MEASUREMENT OF THE $B^0\overline{B}^0$ MIXING

AT THE FERMILAB TEVATRON COLLIDER

Lingfeng SONG

A DISSERTATION

in

PHYSICS

Presented to the Faculties of the University of Pennsylvania in Partial Fulfillment of the Requirements for the Degree of Doctor of Philosophy

1991

Supervisor of Dissertation

Graduate Group Chairperson

ACKNOWLEDGMENTS

I would like to thank my thesis advisor Professor Robert Hollebeek for continuous encouragement and support during my graduate study. His deep insight into of physics and related technical aspects of analysis provided me with invaluable help and intuition. I gratefully acknowledge my thesis committee members, Professor Pekka Sinervo and Professor Hugh Williams. Their encouragement and criticisms made this thesis work polished and effective. Pekka's very detailed review of this thesis and his seriousness toward other projects that I have been worked on with him gave me a very deep impression.

I would like to express my sincere thanks to my other collaborators in this project, Dr. GP Yeh and Dr. John Yoh. GP's encouragement and hard work from the beginning made this difficult analysis possible and the results available in a timingly fashion. His willingness and ability to solve problems overnight has been consistently the driving force for this analysis to reach its next goal. I would also like to thank Dr. Brenna Flaugher and Dr. Lina Galtieri for their help and guidance during this analysis.

The active and humorous Penn group made my graduate study a very enjoyable life experience. I would like to thank all of them, especially Professor Larry Gladney, Professor Nigel Lockyer, Professor Ken Ragan, Dr. Brian Harral, Dr. Eva Low, Dr. to be Tim Rohaly and Richard Hughes, Yi Cen, Julio Gonzalez, Gary Houk and

Wei Zhang.

Finally, I would like to thank my wife and our family members for their love and support.

ABSTRACT

MEASUREMENT OF THE $B^0\overline{B}^0$ MIXING

AT THE FERMILAB TEVATRON COLLIDER

Lingfeng SONG

Dissertation Supervisor: R. Hollebeek

The phenomenon of $B^0\overline{B}^0$ mixing is studied using electron-muon events from $p\bar{p}$ collisions at $\sqrt{s} = 1.8$ TeV. With the extremely high $b\bar{b}$ production rate in such high energy hadron collisions, a large $e\mu$ sample of 900 events is obtained with a background fraction determined to be $(19 \pm 9)\%$. The like-sign to opposite-sign charge ratio R is measured to be 0.556 ± 0.048 (stat) $^{+0.035}_{-0.042}$ (sys). From this measurement, the $B_d^0\overline{B}_d^0$ and $B_s^0\overline{B}_s^0$ averaged mixing parameter χ is found to be 0.179 ± 0.027 (stat) $\pm$ 0.022 (sys) $\pm$ 0.032 (model), where the last uncertainty is due to Monte Carlo modeling.

Contents

1 Introduction **1**

1.1 The Standard Model and Quark Mixing 1

1.2 B Physics at Hadron Colliders 6

1.3 $B^0\overline{B}^0$ Mixing 11

1.3.1 The Origin 11

1.3.2 Related Physics 15

1.3.3 Method of Measurement 17

1.3.4 Brief Experimental History 18

2 CDF Overview **21**

2.1 The Detector 21

2.1.1 Tracking 23

2.1.2 Central Calorimeters 26

2.1.3 Muon Detection 27

2.2 Electronics, Trigger/DAQ System 29

2.3 Offline Software 32

2.3.1 Reconstruction 32

2.3.2 Event Generation and Detector Simulation 34

2.3.3 General Utilities and Network Server 35

3 Event Selection **37**

3.1 Data Sample for Mixing Analysis 37

3.2 Background Events for Mixing Measurement in the $e\mu$ Sample 41

3.3 Electron Identification 45

3.4 Muon Identification 50

3.5 Electron-muon Event Selection 56

4 Background Estimation **71**

4.1 Method of Background Determination 73

4.2 Muon per Track Rate f_μ 76

4.3 Background Fraction 86

4.4 Limit on Over-estimate 89

4.5 Background from J/Ψ Decays 94

4.6 Background Subtraction 102

5 Monte Carlo Modeling of Unmixed B Decays **104**

5.1 Heavy Quark Production 107

5.1.1 Direct $b\bar{b}$ Production 111

5.1.2 Gluon Splitting 115

5.1.3 Flavor excitation 122

5.2 Heavy Quark Fragmentation 123

5.3 Monte Carlo Data Sample 124

5.3.1 Gluon Splitting Fraction 127

5.3.2 Systematic Uncertainties from Monte Carlo 129

6 Determination of the Mixing Parameter 132

6.1 Effect of Monte Carlo ratios f_s, f_c 132

6.2 Effect of Background Fraction f_{BK} 136

6.3 the Mixing Parameter 137

7 Fitting Method — a Consistency Check 141

7.1 muon P_T distribution in the final $e\mu$ sample 142

7.2 Fitting 145

7.3 Results 148

8 Conclusions & Discussions 152

8.1 Other Recent Results 153

8.2 The B_s mixing 153

8.3 Tagging Efficiency, $e\mu$ Rate and CP violation 156

8.4 Future Prospectives for B physics 160

Bibliography **162**

A CDF Coordinate System **166**

B CDF Jet Algorithm **167**

C Calculation of Statistical Uncertainty for the Charge Ratio R **169**

List of Figures

1.1 Z^0 mass spectrum from SLAC and LEP experiments, which limits the Standard Model to only three families. 3

1.2 b quark production cross-section measurements at CDF. 6

1.3 P_T spectrum for inclusive electrons from CDF 1988-1989 run data. . . 9

1.4 Reconstructed D^0's in the inclusive electron sample. 9

1.5 Full reconstruction of $B_u^{\pm} \rightarrow J/\Psi K^{\pm}$ from CDF 1988-1989 run data. . 10

1.6 Full reconstruction of $B_d^0 \rightarrow J/\Psi K^*$ from CDF 1988-1989 run data. . 10

1.7 Time dependence of $B^0\overline{B}^0$ mixing, shown with the expected B_d and B_s mixing parameter $x = 2\Delta m/\Gamma$ values. 13

1.8 Box diagrams for $B^0\overline{B}^0$ mixing. 13

1.9 Top quark mass dependence of the mixing function F(x). 15

2.1 An elevation view of the Collider Detector at Fermilab. 23

2.2 Vertex Time Projection Chamber at CDF. 24

2.3 Central Tracking Chamber at CDF. 25

2.4 Track transversing a muon tower. Sense wires in different cells are offset by 2 mm. The drift velocity can be determine by the differences in drift time. 28

2.5 CDF Data Acquisition System. 30

3.1 Feynman diagrams for Drell-Yan process. 41

3.2 Higgs production via gluon fusion. 44

3.3 Had/EM spectrum for W electrons. 46

3.4 E/P distribution for W electrons. 47

3.5 EM tower energy for J/Ψ muons. 53

3.6 Hadronic tower energy for J/Ψ muons. 53

3.7 Δx matching for J/Ψ muons. 54

3.8 CTC/CMU matching χ^2 spectrum for J/Ψ muons. 55

3.9 Electron Had/EM distribution for $e\mu$ candidates. 59

3.10 Electron E/P distribution for $e\mu$ candidates. 59

3.11 Electron CTC/CES matching in $r\phi$ (left) and z (right) for $e\mu$ candidates. 60

3.12 Electron shower profile fitting χ^2: strip vs wire from CES for $e\mu$ candidates. 60

3.13 Muon EM tower energy distribution for $e\mu$ candidates. 61

3.14 Muon hadronic tower energy distribution for $e\mu$ candidates. 61

3.15 Muon x-matching distribution for $e\mu$ candidates. 62

3.16 Muon CTC/CMU matching χ^2 distribution for $e\mu$ candidates. 62

3.17 Muon track qualities: CTC hit distribution; distance of closest approach (DCA); track vertex to the primary vertex (z component). . . 63

3.18 $e\mu$ data azimuthal opening angle and invariant mass distributions for like-sign and opposite-sign events. 64

3.19 $e\mu$ azimuthal opening angle vs invariant mass for LS (top) and OS (bottom) events. 66

3.20 $e\mu$ invariant mass for single B decays at generator level Monte Carlo. 67

3.21 $e\mu$ invariant mass for single B decays from full Monte Carlo. 67

3.22 $e\mu$ opening angle after the invariant mass cut. 68

3.23 E_T^e vs P_T^μ after the invariant mass cut. 69

4.1 Minimum-bias event good track qualities: CTC hit distribution; distance of closest approach (DCA); track vertex to the primary vertex (z component). 78

4.2 Interaction cross-section in steel for pions and kaons. In each plot, the top curve is for total cross-section, the bottom curve is elastic cross-section. The middle one is the difference between these two curves, representing the absorption cross-section. 79

4.3 Charge asymmetry in punch-through kaons. 79

4.4 P_T dependence of the muons per track rate f_μ for non-interacting punchthrough particles. 82

4.5 P_T dependence of the muons per track rate f_μ for decay muons. . . . 82

4.6 Muon border tower energy spectrum for $e\mu$ events. 84

4.7 Muon border tower energy spectrum for minimum-bias muon events. 84

4.8 A typical $e\mu$ event (like-sign). 85

4.9 χ^2 distribution for minimum-bias muons. 92

4.10 χ^2 distribution for J/Ψ muons. 92

4.11 χ^2 distribution for $e\mu$ muons. 93

4.12 P_T spectrum of b quarks from next to leading order QCD calculations. 98

4.13 Peterson fragmentation function. 98

4.14 Momentum spectrum for J/Ψ's from B meson decay at rest (CLEO). 99

4.15 Momentum spectrum for inclusive leptons from B meson decay in the B meson rest frame (CLEO). 99

4.16 Muon P_T from $b \rightarrow J/\Psi \rightarrow \mu^+\mu^-$ decays. Only one muon has been accepted by the detector geometry and only such muons have been plotted. 101

4.17 Muon P_T from inclusive B semileptonic decays, including sequential decays. CDF muon chamber geometry acceptance implied. 101

5.1 Feynman diagrams for Lowest Order $b\bar{b}$ production. 108

5.2 Feynman diagrams for Next Leading Order $b\bar{b}$ production. 108

5.3 $e\mu$ opening angle for LS events from lowest order $b\bar{b}$ production. . . . 112

5.4 $e\mu$ opening angle for OS events from lowest order $b\bar{b}$ production. . . . 112

5.5 $e\mu$ pair mass for LS events from lowest order $b\bar{b}$ production. 113

5.6 $e\mu$ pair mass for OS events from lowest order $b\bar{b}$ production. 113

5.7 $b\bar{b}$ P_T correlation in Lowest Order $b\bar{b}$ production. 114

5.8 $e\mu$ vector sum P_T distribution from lowest order $b\bar{b}$ production. 115

5.9 $e\mu$ opening angle for LS events from gluon splitting $b\bar{b}$ production. . . 118

5.10 $e\mu$ opening angle for OS events from gluon splitting $b\bar{b}$ production. . . 118

5.11 $e\mu$ pair mass for LS events from gluon splitting $b\bar{b}$ production. 119

5.12 $e\mu$ pair mass for OS events from gluon splitting $b\bar{b}$ production. 119

5.13 $b\bar{b}$ P_T correlation in gluon splitting $b\bar{b}$ production. 120

5.14 $e\mu$ vector sum P_T distribution from gluon splitting $b\bar{b}$ production. . . 120

5.15 b quark P_T distribution from ISAJET. 121

5.16 Fragmentation function for b and c quarks. 124

5.17 $e\mu$ vector sum P_T distribution from final data sample. 128

5.18 $e\mu$ vector sum P_T distribution from Monte Carlo. 128

6.1 Muon border tower energy for LS MC $e\mu$ events from $b\bar{b}$ decays. . . . 135

6.2 Muon border tower energy for OS MC $e\mu$ events from $b\bar{b}$ decays. . . . 135

6.3 Muon border tower energy for MC $e\mu$ events from $c\bar{c}$ decays. 136

6.4 Mixing parameter χ as a function of the background fraction f_{BK}. . . 138

6.5 Charge ratio R versus mixing parameter χ. 139

6.6 Muon P_T spectra for the data, Monte Carlo with the observed mixing and background in like-sign and opposite-sign $e\mu$ events. The uncertainties for the data are statistical only, while those for the background are the determined 47%. Both the data and the Monte Carlo include the background. 140

7.1 Muon P_T spectrum in LS $e\mu$ data. 144

7.2 Muon P_T spectrum in OS $e\mu$ data. 144

7.3 Background free muon (OS-LS) P_T distribution in $e\mu$ data. 146

7.4 Background track (OS-LS) P_T distribution. 146

7.5 Muon P_T spectrum from direct $b\bar{b}\rightarrow e\mu$ decays. 147

7.6 Muon P_T spectrum from sequential $b\bar{b}\rightarrow e\mu$ decays. 147

7.7 Muon P_T spectrum from $c\bar{c}\rightarrow e\mu$ decays. 148

7.8 Log likelihood function from fitting. 149

7.9 χ versus background fraction f_{BK} for R and fitting methods. 150

8.1 CDF $e\mu$ channel: χ_d versus χ_s. 156

8.2 All combined: χ_d versus χ_s contour. 157

List of Tables

1.1 Fundamental interactions and their mediating bosons. 2

3.1 Electron-muon selection criteria. 57

3.2 Final $e\mu$ sample. 70

4.1 Track punch-through probability with different K/π ratios. 80

4.2 Uncertainties for the muon per track rate f_μ. 86

4.3 $e\mu$ background fraction from inclusive electrons. 88

4.4 Relative background level in minimum-bias, J/Ψ and $e\mu$ events. . . . 93

4.5 Relative efficiency for muons from B to J/Ψ and semiletonic decays. . 100

5.1 Summary of full Monte Carlo data sample. 126

5.2 Monte Carlo predictions of no-mixing ratios f_s and f_c. 126

5.3 Systematic uncertainties from Monte Carlo predictions. 129

8.1 Summary of current mixing measurements. 154

8.2 Comparison of different B decay channels for CP violation observation. 159

Chapter 1

Introduction

1.1 The Standard Model and Quark Mixing

Since the discovery of radioactivity in the late 19th century, history has witnessed many dramatic discoveries and developments in the field of particle physics. In the past two decades, a general picture which describes well our current knowledge about matter constituents and the fundamental interactions has emerged. This is called the Standard Model (SM). In this general model, fundamental particles are divided into 3 families. Each family consists of two quarks and two leptons as

$$\begin{pmatrix} u \\ d \end{pmatrix} \quad \begin{pmatrix} c \\ s \end{pmatrix} \quad \begin{pmatrix} t \\ b \end{pmatrix} \quad \text{quarks}$$

$$\begin{pmatrix} \nu_e \\ e \end{pmatrix} \quad \begin{pmatrix} \nu_\mu \\ \mu \end{pmatrix} \quad \begin{pmatrix} \nu_\tau \\ \tau \end{pmatrix} \quad \text{leptons}$$

Each particle also has an antiparticle. All of these particles are fermions with spin 1/2. Except for the neutrinos, all other particles have different mass values. The top quark

Table 1.1: Fundamental interactions and their mediating bosons.

Interaction	Mediating Bosons
Electro-weak	γ, $W^{\pm}$, Z^0
Strong	gluons (g)

is yet to be seen, but its mass is limited to be above 91 GeV at 95% confidence level (C. L.) [1]. Fundamental interactions between these particles (neglecting gravity) are mediated by four types of gauge bosons as shown in table 1.1. In addition to these fundamental particles, there is a scalar boson — the Higgs boson (H_0) which breaks the gauge symmetry in the electro-weak interaction and brings mass to the heavy gauge bosons ($W^{\pm}$, Z^0) and the fermions. This scalar boson has not been observed yet. The current limit on its mass is $m_{H_0} \geq 48$ GeV at 95% C. L. from CERN LEP experiments.

The electro-weak interaction is successfully described by an $SU(2) \times U(1)$ gauge theory. This interaction manifests itself in the decays of the $W^{\pm}$, Z bosons, the heavy quarks and in the normal electromagnetic interactions. The strong interaction is described by Quantum Chromodynamics (QCD), which is an $SU(3)$ gauge field theory. This is the interaction responsible for the production of heavy quarks (c, b, t and their antiquarks) in $p\bar{p}$ collisions and the nuclear forces. The Standard Model is usually referred to as an $SU(3) \times SU(2) \times U(1)$ gauge theory. Recent experiments at

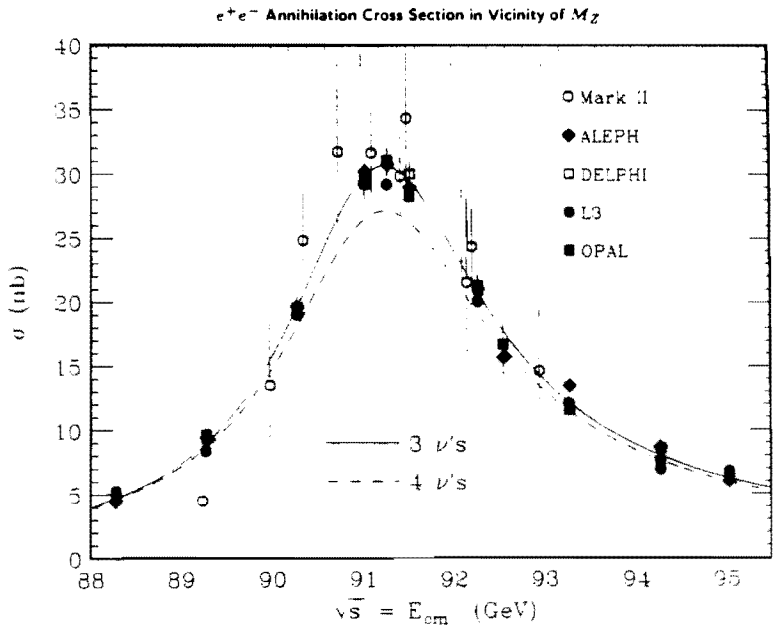

Figure 1.1: Z^0 mass spectrum from SLAC and LEP experiments, which limits the Standard Model to only three families.

SLAC and CERN imply that the SM is limited to only 3 families. This observation results from the measurement of the Z^0 decay with to invisible particles ($Z^0 \rightarrow \nu\bar{\nu}$). The result is shown in figure 1.1 [2].

Due to weak interactions, the masses of fermions are not conserved, so different quark families can mix. For example, the quark-quark weak interaction Lagrangian has the form,

$$L_{int} \sim \bar{u}_L \gamma_\mu \frac{1-\gamma_5}{2} V_{CKM} d_L W^{+\mu} + h.c.$$

where u_L and d_L represent the *up* and *down* type quark operators with charge $Q = +2/3$ and $Q = -1/3$ respectively, γ_μ are the Dirac matrices and $W^{+\mu}$ is the weak

boson W^+ propagator. The unitary matrix V_{CKM} is the Cabbibo-Kobayashi-Maskawa (CKM) matrix, which has the form

$$\begin{pmatrix} V_{ud} & V_{us} & V_{ub} \\ V_{cd} & V_{cs} & V_{cb} \\ V_{td} & V_{ts} & V_{tb} \end{pmatrix}$$

This matrix explicitly shows that different flavor quarks with different masses can mix with coupling strength given by the matrix elements. The matrix is nearly diagonal, but none of the elements are zero. The fact that a phase change for each of the 6 quarks wave functions should not change the physics and an overall phase change doesn't change the CKM matrix restricts the independent matrix elements to $9-(6-1)=4$. A useful representation is given by Wolfenstein [3] as

$$\begin{pmatrix} 1-\frac{1}{2}\lambda^2 & \lambda & A\lambda^3(\rho-i\eta) \\ \lambda & 1-\frac{1}{2}\lambda^2 & A\lambda^2 \\ A\lambda^3(1-\rho-i\eta) & -A\lambda^2 & 1 \end{pmatrix} + O(\lambda^3)$$

with [4]

$$\lambda \simeq 0.22$$

$$A \simeq 1.0 \pm 0.3$$

$$0.3 \leq \sqrt{\rho^2+\eta^2} \leq 1.14$$

where λ is the Cabbibo angle. These numbers are useful for later discussions of B_d and B_s mixing. Except λ, none of the parameters are accurately determined. This

leads to uncertainties in some of the SM predictions. As an important example, the imaginary part of V_{ub} or V_{td}, i.e. η, provides a description of CP violation in the SM scheme. Therefore, experimental determination of the CKM matrix elements is very important in testing the Standard Model and probing new physics beyond.

Since the top quark hasn't yet been seen, the matrix elements related to the top quark cannot be directly measured. However, these elements effect related properties of the bottom quark and other observed quarks. Historically, this is demonstrated in the kaon (s quark) system. Experimental studies of kaon decays had provided many important inputs for new physics well before the discovery of the c (in J/Ψ) and b (in Υ) quarks. This includes the discovery of CP violation, which seems to require at least 3 families in the Standard Model. Since the kaon system only involves the first 2 quark families directly, heavy quark contributions must enter in loop diagrams. The smallness of the coupling constants (CKM matrix elements) greatly suppresses the relevant effects. For the B system, most interesting processes are less suppressed, which can be seen clearly in the Wolfenstein representation of the CKM matrix. Hence studies in the B sector hold more promise. While the mystery of CP violation is strongly hoped to be understood in the B system, precise measurement of the B lifetime, $b \to u$ transition and $B^0\overline{B}^0$ mixing will enable us to completely determine the CKM matrix and test the Standard Model's consistency. Extensive studies of B physics are clearly demanded.

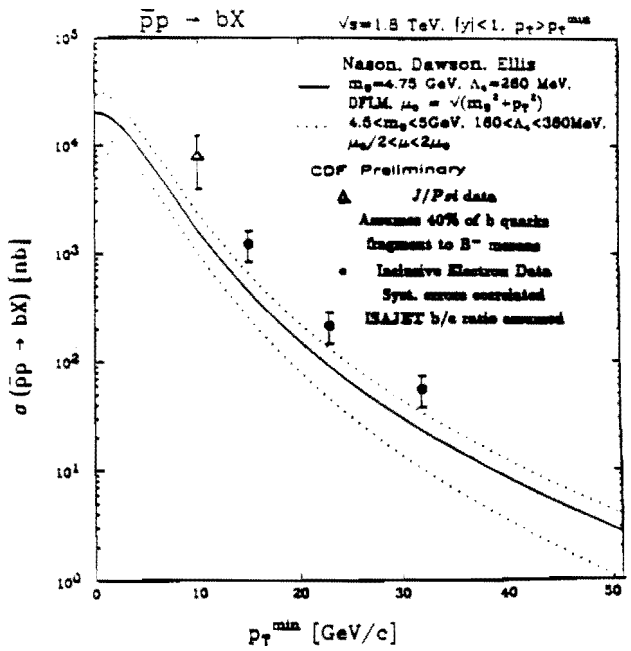

Figure 1.2: b quark production cross-section measurements at CDF.

1.2 B Physics at Hadron Colliders

After the discovery of the b quark in the Υ resonances (1977), many efforts have been devoted to the understanding of this new heavy quark ($m_b \simeq 5.3$ GeV) system. Most notable are those at the e^+e^- colliders operated at the $\Upsilon(4S)$ resonance (ARGUS, CLEO and others). Many properties of the B decays and $B_d^0\overline{B}_d^0$ mixing have been learned. At e^+e^- colliders operated at the $\Upsilon(4S)$, the $b\bar{b}$ production fraction is as large as 1/3 of the collision rate. The produced B mesons can only be in either B^+B^- or $B^0\overline{B}^0$ states as production is via the electro-weak interaction. Such production processes have very small background giving the e^+e^- experiments a relatively clean environment. However, the complexity and very often small branching ratios in B

decays require a large production rate to perform detailed studies.

At high energy hadron colliders the situation is different. The $b\bar{b}$ production cross-section is very large. At the Fermilab Tevatron, with $\sqrt{s} = 1.8$ TeV the cross-section for $p\bar{p} \to bX$, with b quark transverse momentum $P_T^b \geq 15$ GeV, and pseudo-rapidity ($\eta = -\log[\tan(\theta/2)]$)) $|\eta| \leq 1.0$ is about 1.2 μb, which is several orders of magnitude higher than e^+e^- machines operated at the $\Upsilon(4S)$. The b quark cross-section measurements by the Collider Detector at Fermilab (CDF) collaboration is shown in figure 1.2. During the 88-89 run, CDF collected about 4.1 pb^{-1} data. This corresponds to about 10^7 $b\bar{b}$ events produced with large P_T in the central region ($|\eta| \leq 1.0$). Such a large b rate is clearly an advantage of the high energy hadron colliders.

The main question for B physics at hadron colliders is the background. It's usually considered that B events produced at e^+e^- colliders are clean while those produced at hadron colliders are dominated by QCD background. So how to identify B events becomes the main issue for hadron colliders. Without a micro-vertex detector to measure the decay vertices, it is extremely difficult to separate b jets from general QCD jets. However, a high P_T lepton provides a good tag of a heavy quark. While leptons from top decay are scarce given the small top quark production cross-section compare to the b quark, those from $c\bar{c}$ decays is highly suppressed by the high P_T requirement. The hard fragmentation and large mass of the b quark make its decay

daughter leptons more energetic than those from c decays. This will be discussed in later chapters. Other sources of leptons are either easily separable or have relatively small cross-sections. Good lepton identification ability will make it possible to study B physics in the semi-leptonic channel and in channels where the B decay products themselves decay to leptons (such as J/Ψ, Ψ', etc.). The P_T spectrum of the inclusive electrons from the 88-89 CDF run is shown in figure 1.3 along with Monte Carlo predictions. Evidence that the main source of the prompt electrons is B decays is obtained by reconstructing the companion D^0 mesons in B$\rightarrow$ lD^0X. This is given in figure 1.4. Further evidence for the large B production rate is given by the full reconstruction of B mesons in the $B_u^{\pm} \rightarrow J/\Psi K^{\pm}$ and $B_d^0 \rightarrow J/\Psi K^*$ channels, see figure 1.5 and 1.6. The J/Ψ's are reconstructed in the dimuon channel, the $K^{\pm}$ was taken as any tracks above certain P_T, and the K^* is searched in the $K\pi$ channel. The branching ratio for such processes are of the order 10^{-5}.

Since B's have a large semi-leptonic branching fraction (about 20%), with good lepton identifications, high rate B physics is accessible at hadron colliders like CDF. The J/Ψ's also provides a very clean source for B studies. If a micro-vertex detector is implemented, more gain in background rejection is expected by tagging the B decay vertex. It's clear that hadron colliders can also make a big contribution to B physics studies.

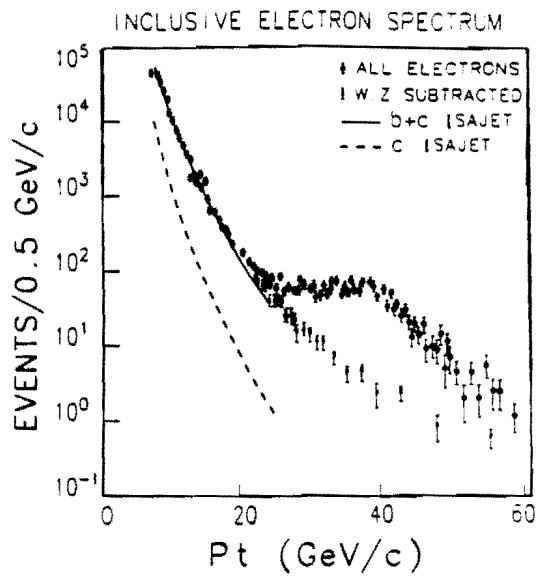

Figure 1.3: P_T spectrum for inclusive electrons from CDF 1988-1989 run data.

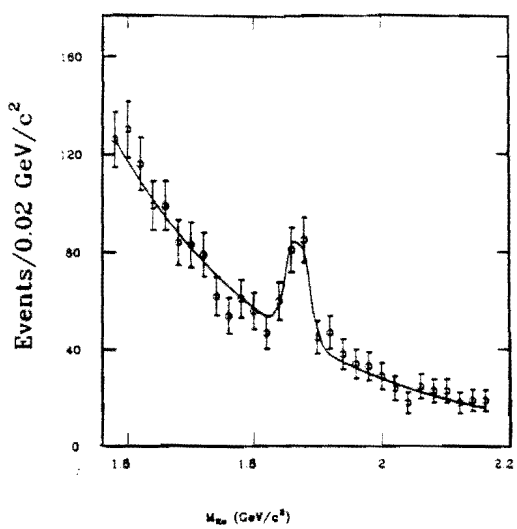

Figure 1.4: Reconstructed D^0's in the inclusive electron sample.

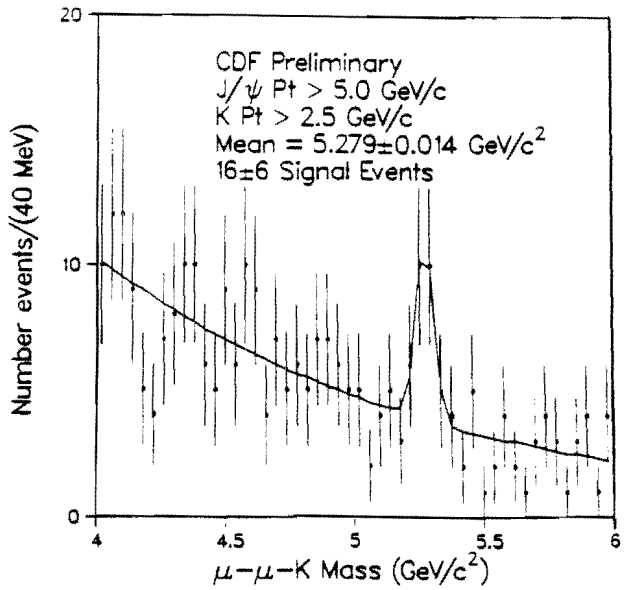

Figure 1.5: full reconstruction of $B_u^{\pm} \to J/\Psi K^{\pm}$ from CDF 1988-1989 run data

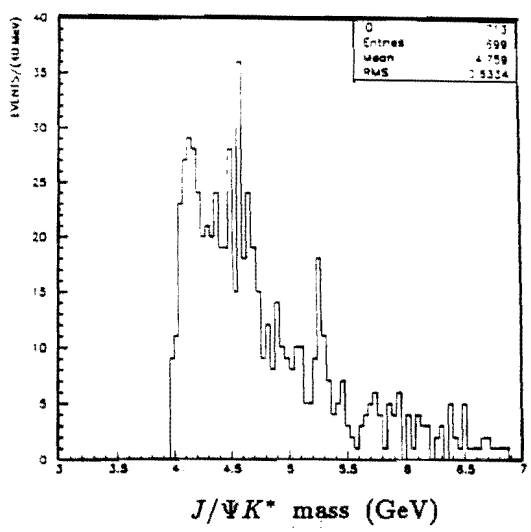

Figure 1.6: full reconstruction of $B_d^0 \to J/\Psi K^*$ from CDF 1988-1989 run data

1.3 $B^0\overline{B}^0$ Mixing

One of the most interesting B physics topics is the study of the $B^0\overline{B}^0$ mixing. As represented by the CKM matrix, different quark flavors can mix due to weak interactions. This phenomenon is first observed in the neutral kaon system. The CKM theory predicts mixing for c and b neutral mesons as well. Since the D^0 decay is Cabbibo favored, its lifetime is too short to allow sizable mixing. The long lifetime of the B makes mixing of $B^0\overline{B}^0$ an observable phenomenon. While a larger than expected mixing has been seen in the $B_d^0\overline{B}_d^0$ system, even larger mixing for $B_s^0\overline{B}_s^0$ is predicted by the CKM theory as we'll discuss below. The top quark is expected to be very heavy and its decay is also Cabbibo favored. Therefore one doesn't expect observable mixing in the top system in the SM scheme. So, in the Standard Model limited to 3 families, the $B^0\overline{B}^0$ and $K^0\overline{K}^0$ systems are the only ones that demonstrate significant mixing.

1.3.1 The Origin

The non-conservation of flavor due to the weak interaction is the reason for flavor mixing. Taking the $B^0\overline{B}^0$ system as an example, one can show how this occurs. From quantum mechanics, if the strong interaction mass eigenstates $|B^0>$ and $|\overline{B}^0>$ are no longer eigenstates of the weak interaction, one expects the new eigenstates to be the superposition of these two states. Since CP is only weakly violated in this case, to

a very good approximation, one can treat CP as a good quantum number in dealing with mixing. Therefore, the weak eigenstates $|B_1>$ and $|B_2>$ satisfies

$$\mathrm{CP}|B_1>=|B_1>=\frac{1}{\sqrt{2}}(|B^0>+|\overline{B}^0>)$$

$$\mathrm{CP}|B_2>=-|B_2>=\frac{1}{\sqrt{2}}(|B^0>-|\overline{B}^0>)$$

An initial state of $|B^0>$ can be written in terms of $|B_1>$ and $|B_2>$ as

$$|B(t=0)>=|B^0>=\frac{1}{\sqrt{2}}(|B_1>+|B_2>)$$

At time t, we have

$$\begin{aligned}
&|B(t)> \\
&=\frac{1}{\sqrt{2}}(|B_1>e^{-im_1t-\frac{\Gamma_1}{2}t}+|B_2>e^{-im_2t-\frac{\Gamma_2}{2}t}) \\
&=e^{-im_1t-\frac{\Gamma_1}{2}t}(|B_0>\frac{1}{2}(1+e^{-i\Delta mt-\frac{\Delta\Gamma}{2}t})+|\overline{B}^0>\frac{1}{2}(1-e^{-i\Delta mt-\frac{\Delta\Gamma}{2}t}))
\end{aligned}$$

where $\Delta m=m_2-m_1$ and $\Delta\Gamma=\Gamma_2-\Gamma_1$. The probability for $|B(t)>$ to be in the $|\overline{B}^0>$ state is

$$P(t)\sim e^{-\Gamma t}(1+e^{-\Delta\Gamma t}-2e^{-\frac{\Delta\Gamma}{2}t}cos\Delta mt)$$

For the $B^0\overline{B}^0$ system, $\Delta m\gg\Delta\Gamma$ and $\Gamma\gg\Delta\Gamma$, so the terms involve $\Delta\Gamma$ can be neglected.

$$P(t)\sim e^{-\Gamma t}(1-cos\Delta mt)$$

as shown in figure 1.7.

The magnitude of $B^0\overline{B}^0$ mixing depends on $2\Delta m/\ \Gamma$. The decay width Γ is determined from the B lifetime measurements. The mass difference is due to second

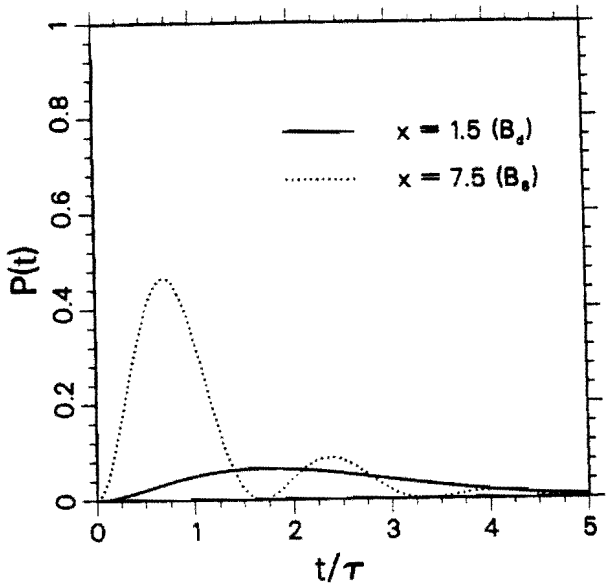

Figure 1.7: time dependence of $B^0\overline{B}^0$ mixing, shown with the expected B_d and B_s mixing parameter $x = 2\Delta m/\Gamma$ values.

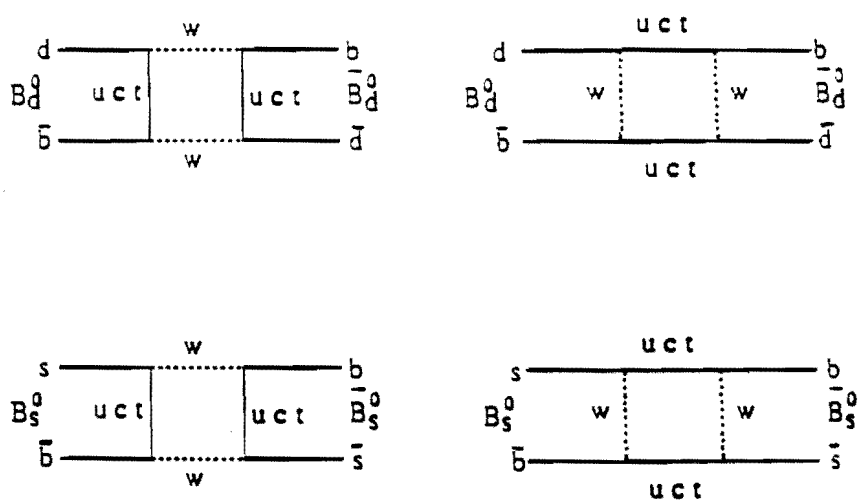

Figure 1.8: box diagrams for $B^0\overline{B}^0$ mixing

order weak interaction as shown in figure. 1.8 It is related to the CKM matrix elements by [9]

$$\Delta m = \frac{8}{3}\eta_{QCD}(\frac{G_F}{4\pi})^2 B_B f_B^2 (V_{tb}V_{tq}^*)^2 m_B M_W^2 F(\frac{m_t^2}{M_W^2})$$

where G_F is the Fermi constant in weak interaction; $B_B f_B$ are related to the B meson wave function; M_W, m_b and m_t are the mass values for W boson and b, t quarks. The function $F(x)$ is given by [9]

$$F(x) = x(\frac{1}{4} + \frac{9}{4(1-x)} + \frac{3}{2(1-x)^2}) - \frac{3}{2}(\frac{x}{1-x})^3 \log x$$

and η_{QCD} contains the radiative QCD corrections. In figure 1.9, $F(x = {m_t}^2/{m_W}^2)$ is shown as a function of the top quark mass m_t together with the 50 GeV constraint line from $B_d^0\overline{B}_d^0$ mixing measurements.

In describing the strength of $B^0\overline{B}^0$ mixing, the following quantities are often used as mixing parameters,

$$x = \frac{2\Delta m}{\Gamma}$$
$$r = \frac{N(B^0 \to \overline{B}^0)}{N(B^0 \to B^0)} = \frac{x^2}{1+x^2}$$
$$\chi_{d(s)} = \frac{N(B_{d(s)}^0 \to \overline{B}_{d(s)}^0)}{N(B_{d(s)}^0 \to B_{d(s)}^0) + N(B_{d(s)}^0 \to \overline{B}_{d(s)}^0)} = \frac{r_{d(s)}}{1+r_{d(s)}}$$

Using the Wolfenstein representation of the CKM matrix, one can see that [4]

$$\frac{x_s}{x_d} = \frac{|V_{ts}|^2 (B_B f_B)_s^2}{|V_{td}|^2 (B_B f_B)_d^2} \geq \frac{|V_{ts}|^2}{|V_{td}|^2} = \frac{1}{\lambda^2((1-\rho^2)+\eta^2)} \geq 5$$

Thus much larger mixing is expected for B_s^0 compare that for B_d^0.

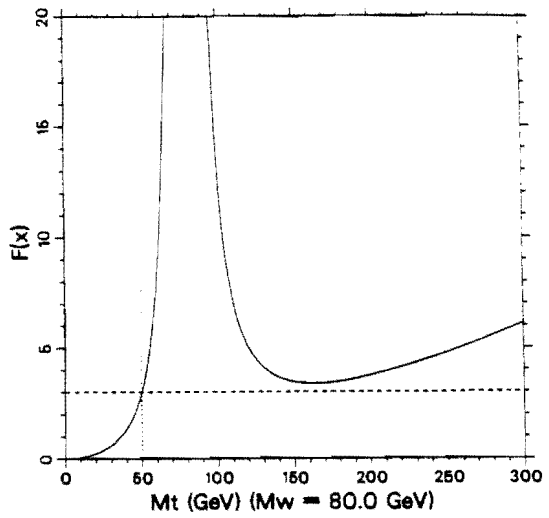

Figure 1.9: Top quark mass dependence of the mixing function F(x).

1.3.2 Related Physics

Mixing itself is an interesting phenomenon. Two degenerate mass eigenstates $|B^0>$ and $|\overline{B}^0>$ of the strong interaction are split by a second order weak interaction. Each state evolves differently in time and results in a particle oscillation effect. This closely resembles the magnetic field splitting of two degenerate spin eigenstates. In this analogy, the spin is replaced by the flavor of the particle, while the magnetic field is replaced by the weak interaction. Mixing studies can therefore provide information about the strength of the second order weak coupling. Accurate measurement of $B_d^0\overline{B}_d^0$ and $B_s^0\overline{B}_s^0$ mixing will lead to the determination of V_{td} and V_{ts}. The degenerate nature of the B^0 and $\overline{B}^0$ mass eigenstates makes the second order weak interaction a large observable effect.

Mixing is related to CP violation in some way. There are two possibilities that can create CP violation. One is via mixing, the other is via final state interaction. In the semileptonic decay (single lepton or dilepton) channels, mixing is the only mechanism for CP violation. A good understanding of mixing can therefore improve the predictions of CP violation effects. [4]

As seen in the formula for Δm, the top quark mass enters quadratically. This is because the heaviest quark dominates the box diagram contribution. One can see this as a phase space effect, or more intuitively, because the weak nature of the box diagram requires a large mass for the propagator. So, measurement of mixing can set limits for the top quark mass. The observed $B_d^0\overline{B}_d^0$ mixing demands a heavy top quark (greater than 50 GeV) [5].

While the B_s meson is yet to be seen directly, experiments above B_s threshold measure an averaged mixing parameter

$$\chi = \frac{prob(b \to \overline{B}^0 \to B^0 \to \ell^+)}{prob(b \to \ell^\pm)},$$

where the leptons can come from both direct and sequential B decays and the denominator includes all possible hadrons formed with the b quark. In terms of the mixing parameters for pure B_d and B_s mesons,

$$\chi = P_d\chi_d + P_s\chi_s,$$

where P_d and P_s is the fraction of the B_d and B_s mesons produced weighted by possible braching ratio differences. (See chapter 8 for a detailed discussion.) The

direct consequence is that the uncertainty in B_s mixing due to the uncertainties in χ and χ_d will be inflated by the factor $1/P_d \simeq 2.5$. However, the number χ itself is useful in several predictions of other B physics processes. For example, the forward-backward $b\bar{b}$ production asymmetry in e^+e^- collisions is given by the form

$$A_{FB} = (1 - 2\chi) f_{FB}$$

where f_{FB} is the asymmetry in the absence of mixing. The averaged mixing parameter enters as a diluting factor. The same situation is true for CP violation effects in certain channels.

1.3.3 Method of Measurement

In order to observe the mixing phenomenon, one has to know not only how to identify the existence of B mesons, but also tag their flavors (b or $\bar{b}$). There is no known way to tag a single B meson flavor as a function of time. So it is crucial that two B's ($B\overline{B}$) are studied at the same time. Conservation of flavor in the strong interaction requires that $b\bar{b}$ be produced in pairs with antiflavors. One needs only to tag the final state flavor and see whether there are bb or $\bar{b}\bar{b}$ pairs to identify mixing. For experiments operated at $\Upsilon(4S)$ threshold, the situation is relatively simple. Because of Einstein-Rosen-Podolsky effect, the $B\overline{B}$ must be produced in a p-wave state with symmetric particle configuration. Thus only $B^0\overline{B}^0$ or B^+B^- can be produced. At higher energies, one can have $B_d^0\overline{B}_d^0$ $B_d^0B_u^-$, $B_u^+B_u^-$, $B_s^0\overline{B}_s^0$ $B_d^0\overline{B}_s^0$, etc. Given the

extreme difficulty of separately identifying B_d and B_s, only the average mixing effect can thus be studied. Since it is a probability measurement, a large statistics sample is required to precisely determine the mixing parameter. The only foreseeable way to achieve a large statistics double tagged $b\bar{b}$ sample is via lepton tagging in B decays. More precisely, dilepton tagging of two different B's. This can be done without a micro-vertex detector if the mixing probability is relative small.

Now we describe the general method used in this analysis. First, a background subtracted dilepton charge ratio R is measured, where R is defined by

$$R \equiv \frac{\#\text{ of LS dileptons}}{\#\text{ of OS dileptons}}.$$

This ratio contains the mixing information, but it is not the direct mixing parameter. There are other processes that can give rise to like-sign dileptons without mixing. So R depends on selection cuts, while χ does not. It is the the mixing probability averaged over all B hadrons. Monte Carlo simulation is used to extract χ from R.

1.3.4 Brief Experimental History

While $K^0\overline{K}^0$ mixing was observed 2 decades ago, mixing in the $B^0\overline{B}^0$ system is a relatively new phenomenon. The SLAC experiment MARK II set a limit for B_d and B_s average mixing as $\chi \leq 0.12$ at 90% C. L. in 1985. In 1987, 10 years after the discovery of the b quark, several experiments reported observations of $B^0\overline{B}^0$ mixing. The CERN S$p\bar{p}$S experiment UA1 observed an excess of like-sign dimuons and the first published

average mixing parameter was $\chi = 0.12 \pm 0.07$ [8]. The ARGUS collaboration reported a larger than expected mixing for $B_d^0\overline{B}_d^0$ system [6]. Subsequently, CLEO and other experiments confirmed these discoveries [7]. The MAC experiment studying e^+e^- collisions at $\sqrt{s} = 28$ GeV (above B_s threshold) reported a value for χ of $0.2^{+0.2}_{-0.2}$ in 1987. The current ARGUS [6] and CLEO [7] combined $B_d^0\overline{B}_d^0$ mixing parameter is $\chi_d = 0.16 \pm 0.04$. The published result from UA1 after re-analyzing the old data is $\chi = 0.158 \pm 0.07$. [9]

At CDF, which will be discussed in detail in the next chapter, $B^0\overline{B}^0$ mixing above B_s threshold can be studied with large statistics, due to the large b production cross-section. We use the electron-muon events from the 88-89 CDF run to double tag the $b\bar{b}$ pairs. To reduce background and maximize detector efficiencies, electrons are required to have transverse energy (E_T) greater than 5 GeV and muons are selected to have transverse momentum (P_T) above 3 GeV. These requirements reduce the contributions from c quark decays and other background while still retaining a $b\bar{b}$ large event sample as we'll show in the following chapters.

The thesis is organized as follows: Chapter 2 provides a general description of CDF apparatus and software support with emphasis on aspects that are most relevant to this analysis; Chapter 3 describes the lepton identification at CDF and event selection for $B^0\overline{B}^0$ mixing measurement; Chapter 4 discusses the background estimation; Chapter 5 describes the Monte Carlo modeling of unmixed B decays; Chapter 6

outlines the mixing parameter determination; Chapter 7 describes a fitting method to check the determined mixing parameter; and the conclusions are presented in Chapter 8.

Chapter 2

CDF Overview

2.1 The Detector

The Collider Detector at Fermilab (CDF) [10] is the first general purpose detector operated at the Tevatron. Its goal is to study various physics processes in $p\bar{p}$ collisions at $\sqrt{s} = 1.8$ TeV, the world's highest energy interactions currently accessible. Surrounding the collision point, various layers of detector components are installed to measure the collision vertex, charged particle tracks, electromagnetic (EM) and hadronic (had) energy deposition and muon signals. Close to the beam pipe, there is a Vertex Time Projection Chamber (VTPC) for the primary vertex measurement. This chamber covers pseudo-rapidity range -3.2 to $+3.2$ and extends from r = 5 cm to r = 24 cm. In between the VTPC and the superconducting magnetic coil at r = 1.5 m there is a 3 m long cylindrical Central Tracking Chamber (CTC) which makes precision measurement of the charged particle track parameters. The η coverage of CTC is from -1.2 to 1.2 at its outer layer. Outside the CTC, there is a 3 layer Cen-

tral Drift Tube (CDT) tracking detector. The magnetic coil is just outside the CDT and is made of aluminum-stablized NbTi/Cu superconducting wire which provides a uniform magnetic field of 1.4116 T in the central volume. Outside the magnetic field, calorimeters in 3 regions cover almost all of the 4π solid angle. Each calorimeter region has two types. The inner one is an EM shower calorimeter while the outer one is a hadronic calorimeter. The central calorimeter is made of lead plates and plastic scintillator for high resolution in a relative low particle occupation environment. It covers the region $|\eta| \leq 1.1$. The end plug and forward/backward calorimeters are made of lead, steel and gas proportional chambers. The η coverage is extended to ± 4.2. To measure the jet activity in $p\bar{p}$ collisions at high energy, all calorimeter cells are made in fine grain tower geometry. Outside the calorimetry, comprising about 5 interaction lengths of material in the central region ($|\eta| \leq 0.63$), there is a 4 layer streamer chamber for central muon (CMU) detection. In the forward/backward region, there are Forward Tracking Chambers (FTC), scintillator Beam-Beam Counters (BBC) to monitor the beam luminosity and provide a beam crossing trigger and Forward Muon chamber (FMU) for additional muon detection. An elevation view of CDF is given in figure 2.1

In the following, we discuss in detail the most relevant detector components used in this analysis. The electron-muon events are selected using the central detectors only. Starting from the beam line, these include the VTPC, CTC, central EM (CEM)

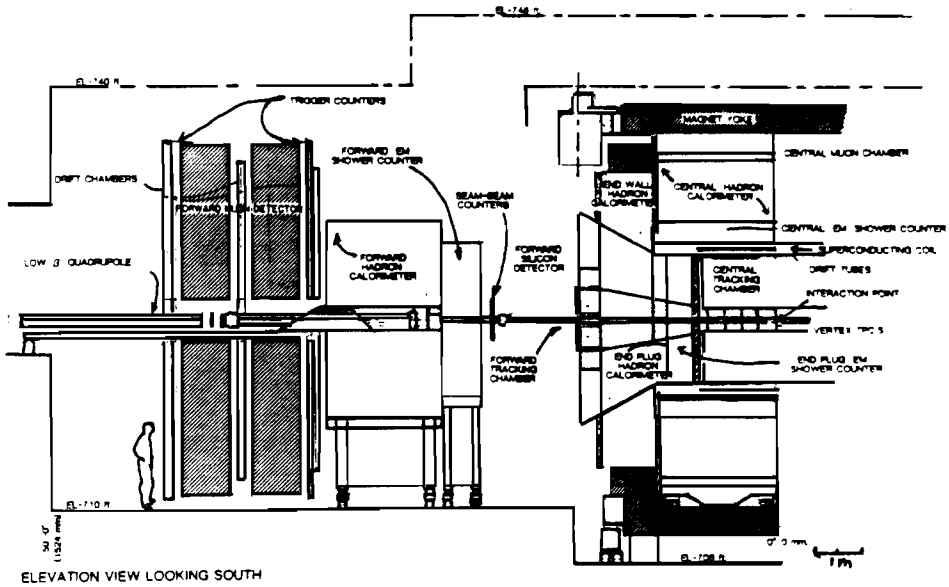

Figure 2.1: An elevation view of the Collider Detector at Fermilab.

and central strip chamber (CES), central hadron (CHA) calorimeter and central muon chamber (CMU). The central drift tube (CDT) is not use in this analysis because the CTC already provides good enough tracking for the events considered.

2.1.1 Tracking

The tracking system used in this analysis includes the VTPC and the CTC. The VTPC is an octagonal time projection chamber [12]. It consists of 8 modules with 16 octants each. There are 24 sense wires and 24 cathode pads for each octant, see figure 2.1.1. The whole chamber is 2.8 meters long with active radial area from $r = 6.8$ cm to $r = 21$ cm. This well covers the $p\bar{p}$ collision point, whose z vertex position

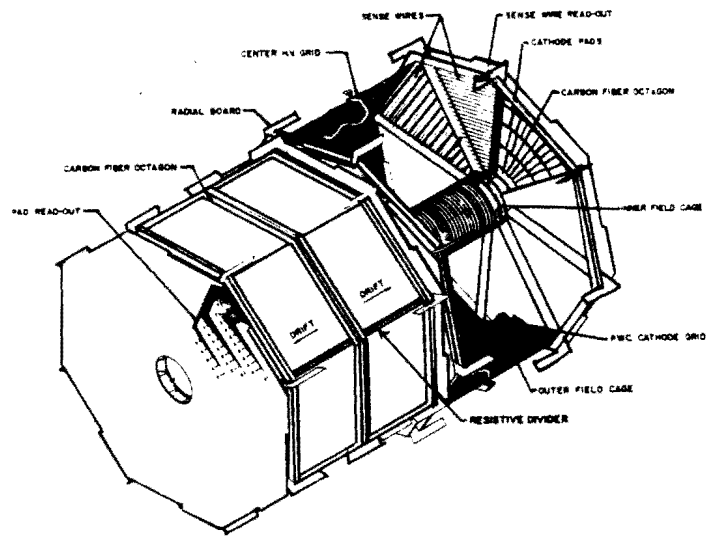

Figure 2.2: Vertex Time Projection Chamber at CDF.

position is described according to a Gaussian with a width of 35 cm. Information from the VTPC is used to measure the event vertex position and to reject photon conversions in electron event selection.

The CTC provides most of the tracking information and momentum resolution. It is a 1.3 m radius and 3.2 m long cylindrical drift chamber [13]. There are 84 layers of sense wires which are arranged in 9 superlayers, of which 5 are axial and 4 are stereo alternating with radial layers. Each axial superlayer contains 12 layers of wires parallel to the beam line which measure the $r\phi$ tracking parameters. The stereo wires have an angle of $\pm 3^\circ$ relative to the beam line. These wires provide 3D information of the tracks. There are 6 wire layers in each of the 4 stereo superlayers. The wires in each superlayers are grouped into cells to limit the maximum drift time

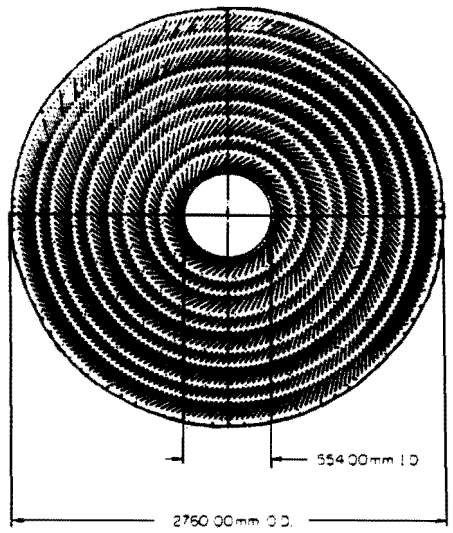

Figure 2.3: Central Tracking Chamber at CDF.

to about 800 ns. An end view of the CTC wire plane is shown in figure 2.1.1. The momentum resolution of the CTC is $0.0011\delta P_T/P^2$ when the track parameters are fit to the hits and the track is constrained to come from the beam vertex. The resolution is $0.0017\delta P_T/P^2$ if no such beam position constraint applied. The individual track impact parameter resolution is about 150 μm and the primary event vertex can be determined to about 60 μm with many tracks.

A high resolution tracking chamber provides important information for charged and non-charged particle identification. In this analysis, the CTC information is heavily used for measurements of charge, momentum, track position and for studies of background, electron and muon selection. A high resolution tracking system is essential for the $B^0\overline{B}^0$ mixing measurements and other B physics studies.

2.1.2 Central Calorimeters

Calorimeters are among the most important and most emphasized detector components in high energy colliders. The CDF central calorimeter consists of the CEM and CHA. The CEM is made of 30 lead sheets interspersed with scintillators [14]. The high Z value of lead allows electrons or photons to shower efficiently and to deposit their energy mostly in the CEM. The scintillator signal is picked up by photo multiplier tubes (PMT). To measure the electron or photon shower position and shape profile, there is a central strip (CES) chamber embedded at the depth where the maximum shower energy is deposited which is about 6 radiation lengths. The radial distance of CES to the beam line is 1.84 m. The CES is made of strips and wires perpendicular to the radial direction and orthognal to each other. Information from the CES along with that from the CTC helps to identify electron or photon objects as we'll discuss in the next chapter. The CEM is calibrated using test beam data and Cs source. The energy resolution for electrons is well described by [11]

$$[\sigma(E)/E]^2 = [13.5\%/\sqrt{Esin\theta}]^2 + [1.7\%]^2$$

where θ is the polar angle measured with respect to the beam direction.

The CHA is made of steel plates sandwiched between scintillators. It contains 32 layers. Both the CEM and CHA calorimeters are divided into cells that form projective towers of $15^\circ \times 0.1$ in $\phi - \eta$ space. The central calorimeter consists of 4 arches, which can be separately removed from the installation position for service.

Each arch includes 12 wedges. There are 10 towers per wedge. In total, there are 478 towers. The pseudo-rapidity coverage is $|\eta| \leq 1.1$, which corresponds to a polar angle (θ) range from 45° to 135°. There are inactive regions between the calorimeter cells and at $\theta = 90°$. These areas (about 15%) are not used for electron detection (with a so-called fiducial volume cut).

With tracking information from the CTC, the small cell size and excellent energy resolution enable a good separation between hadrons and electrons. Without the CES, the hadron rejection factor is about $(2-3) \times 10^{-3}$. The CES can provide more rejection power with shower position matching and shape profile information. The gain factor is close to 10. The CDF central calorimeter system thus provides excellent electron identification for electrons with E_T as low as 2 GeV. More discussion of electron identification is given in the next chapter.

2.1.3 Muon Detection

Central muons are identified as charged particles that penetrate the calorimeters and leave hits in the CMU [15]. The CMU is also constructed in a wedge geometry to match that of the calorimeter. The CMU wedge size in ϕ is 12.6° with a 2.4° crack between each wedge. The CMU is radially 3.47 m away from the beam line. There are 4 layers of modules in each wedge. Each module consists of 3 cells with a 2.36 m long stainless steel sense wire ($50\mu m$) in each cell center. The chambers are operated

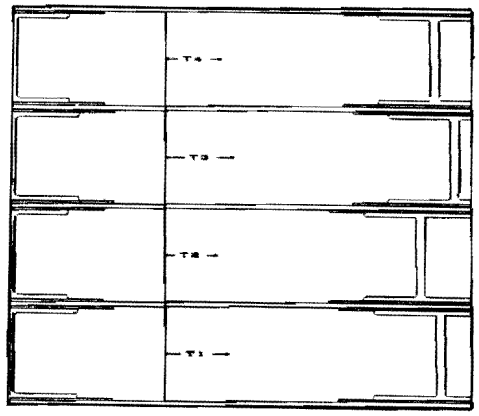

Figure 2.4: Track transversing a muon tower. Sense wires in different cells are offset by 2 mm. The drift velocity can be determine by the differences in drift time.

in streamer mode. The η coverage is from -0.63 to 0.63. Wires in different layers within one module have offsets of a known amount for $r\phi$ track position and magnetic field deflection angle measurement (see figure 2.4). The *rms* resolution in the drift direction is about 250μm. The position of the track hits along the wire direction is obtained using charge division between two wires (which are connected at one end). The charge collected by the ADC's at each end of the wire depends on the location of the charge cluster along the wire. By measuring the ratio of the ADC counts from two connected sense wires, the z position of the track hit on the wire can be determined. The CMU track segment measurements combined with tracking information from the CTC enables one to make stringent matching cuts for muon identification.

2.2 Electronics, Trigger/DAQ System

The CDF detector has about 75,000 channels of output signals. To handle these signals, several electronic systems have been used. For readout of analog signals, a Redundant Analog Bus-Based Information Transfer (RABBIT) system is used. About 60% of the CDF front-end channels are processed through the RABBIT crates. These include the calorimeter and central muon chamber outputs. The signals from each RABBIT crate are read out by FASTBUS based intelligent scanners called MX's. The other 40% of the channels are basically for the tracking systems, which are readout by another kind of intelligent scanner called an SSP (SLAC Scanner Processor). The schematic diagram for the CDF DAQ system is shown in figure 2.5. Most of the electronics are FASTBUS based. The rest are CAMAC based.

The hardware CDF trigger during the 88-89 run consists of 3 levels. The Beam-Beam Counter (BBC) provides a minimum-bias trigger, which is usually referred to as level 0. The level 1 trigger is based on energy deposition in the calorimeters, muon chamber hits or stiff track in CTC. This reduces the event rate of 50-75 kHz to about 1 kHz. At level 2, the trigger is driven by the event topology of calorimeter clusters, central stiff track and muon or electron candidates. In some cases, it uses a fast hardware trigger processor. All hardware trigger systems use fast analog signals from the detector. Above the hardware triggers, there is an online FORTRAN based software trigger system. This is called level 3 trigger, which executes some of the

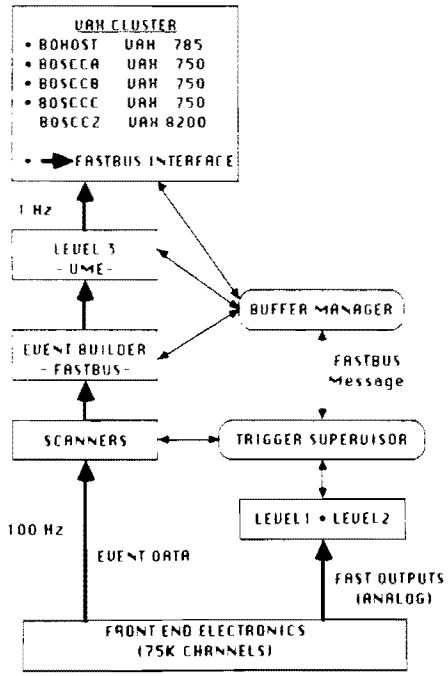

Figure 2.5: CDF Data Acquisition System.

CDF offline reconstruction codes and selects events with much tighter criteria than the hardware triggers. This trigger was not used for the main trigger in $e\mu$ data collection.

As an example of the triggers implemented during the 88-89 run, we take a look at the electron-muon trigger, which is the main trigger for collecting the $e\mu$ events for this analysis. At level 1, a 5 GeV EM cluster is found in CEM for the electron candidates and there must be at least 3 hits found in CMU to form a muon track segment (muon stub). At level 2, an online hardware track processor (CFT — Central Fast Tracker) is used to find a high P_T track to match the EM cluster and muon stub found at level 1. If an event passes all requirements, this event is read out by the DAQ system.

The pipe line structure of the DAQ system [16], as shown in figure 2.5, enables fast event readout. Digitized data are read in by the scanners. Above these scanners, there is an electronic module called Event Builder (EVB), which is responsible for reformatting the output data structure. The trigger supervisor controls the scanners based on information from the lower level (L0-L2) trigger systems. The level 3 system further filters the events before passing them to the host computer for analysis or storage. The Buffer Manager oversees the Event Builder, Level 3 and the host computer during data collection.

When an event passes the trigger, the trigger supervisor will enable the scanners

to readout and the EVB reads in the event data from the scanners, formats it and writes the formated data into one of the level 3 trigger processors. Since level 3 did not put further requirement on the $e\mu$ trigger, the event was output to the host computer and later stored on magnetic tapes.

2.3 Offline Software

An average event from CDF has about 80K bytes of raw information. During the 88-89 run, about 6 million events were recorded. This corresponds to about 0.5×10^{12} bytes or 0.5 Terabytes of data. To reconstruct and analyze this amount of data, a large complex offline software system is required. Besides analyzing the real data, Monte Carlo event generation and full detector simulations are also needed for studies of the detector response to specific physics processes. The CDF offline package contains more than 1 million lines of FORTRAN code, developed by many physicists during the past several years. In the following subsections, we briefly discuss some of the software that are most relevant to this analysis.

2.3.1 Reconstruction

The data recorded from a CDF run are called raw event records. These contain raw detector information, such as ADC counts from calorimeters or TDC counts from drift chambers. To turn these piecewise data into physical quantities, such as jets, electron

candidates and track momentum, a software reconstruction process has to be done. At CDF, this process is called "production". All raw events will be reconstructed and several physics offline data streams will be generated as outputs. The software used in production includes electron candidate finding, muon candidate finding, jet clustering, tracking, measurement of missing transverse energy and many other algorithms. The CDF clustering finding algorithm is given in Appendix B. An electron candidate is defined as an EM cluster with E_T greater than 5 GeV and the EM to hadronic energy ratio less than 0.125. There must be at least one track pointing to the cluster cell to reject photon candidates. A muon candidate is a CMU stub (defined by at least three hits within a time window) matched to a CTC track in both $r\phi$ and z positions. Several filter algorithms are executed after the reconstruction program to select certain physically interesting data types. The muon filter selects muon objects with different P_T thresholds based on the trigger used for a given event. If an event passes a certain filter, it is output to the corresponding stream. In this analysis, three data streams were used. These are the inclusive muon stream, where the $e\mu$ events were selected; the inclusive electron stream and the minimum-bias stream. The latter two were used for the background determination. The total data sample adds up to more than 2000 magnetic tapes, each holding about 150 Megabytes of information.

2.3.2 Event Generation and Detector Simulation

Monte Carlo simulations are needed in almost all analyses. These include studies of detector acceptance, efficiency and event structure. So Monte Carlo event generators and detector simulation packages are among the most important offline programs. At CDF, several such packages exist. The most often used event generator is ISAJET by F. Paige and S. Protopopescu [17] with minor CDF modifications. ISAJET is a general purpose event generator. Most $p\bar{p}$ physics has been incorporated. This analysis uses a modified version of ISAJET to generate $b\bar{b}$ events as we'll discuss in detail in Chapter 5. After the event generation, a full detector simulation is often required. This is done by another software package called CDFSIM [18], which takes each generated particle and propagates it through the components of the CDF detector in its flight path. The response of each detector component is simulated with parameters measured at a testbeam or from other processes. The output data have the same structure as a real CDF raw event record. After simulation, the MC data is reconstructed using the same "production" package as for the real data. Unless otherwise specified, MC data refers to fully simulated data. The same analysis codes used on real data events can be applied to MC data. Generator level data are sometimes used to study the event physics properties with large statistics while saving CPU time. The CDFSIM package takes about 60 VAX-780 equivalent CPU hours to process 1000 events while the "production package" is slightly faster but requires at

least 48 Mbytes memory to run on an IBM3090 mainframe computer.

2.3.3 General Utilities and Network Server

Aside from the well defined software packages discussed above, there are many utilities for offline analysis, such as the CDF Analysis_Control, which provides a generic environment for each individual's analysis codes. It handles general I/O functions for data transfer, organizes different analysis modules, enables the user to specify various control functions, etc. Other utilities include histogram display, event display, CDF job builder and a FORTRAN compiler preprocessor (EXPAND).

The reference location of the offline software is the Fermilab VAX computer cluster. However, for a collaboration with more than 200 physicists from over 20 institutions across the US, Italy and Japan, it is necessary that the software is available on different computer systems. The first question is compatibility. This is achieved at CDF by defining a standard coding scheme based on FORTRAN and using the EXPAND compiler preprocessor. Before installing each routine in the offline area, a test is done to check the compatibility with other computers such as the IBM VM system. To make the software available on systems other than the Fermilab VAX cluster, network servers [19] are employed. Such servers monitor changes on the Fermilab VAX cluster on a day-to-day basis (most servers only work at night to avoid interference with the normal system performance). If changes are detected, a request

for update is sent by the local server to the corresponding server on the Fermilab VAX. Normally, this will keep the off-site user within a day of code availability.

Chapter 3

Event Selection

3.1 Data Sample for Mixing Analysis

As discussed briefly in the introduction, in order to measure the $B^0\overline{B}^0$ mixing, one has to tag the flavor of both b quarks in the final state. The most efficient way for such tagging is through leptons from inclusive decays. In an ideal situation, when only $b\bar{b}$ pairs are produced and their decay products do not themselves decay to leptons, then dileptons can only come from

$b \rightarrow l^-$

$\bar{b} \rightarrow l^+$

So a positive charged lepton identifies b flavor while a negative charged lepton tags anti-b ($\bar{b}$) flavor. Without mixing and other complications, only opposite-sign (OS) dileptons are expected. If there is mixing, one of the initial state b quarks can change its flavor via

$b \rightarrow \overline{B}^0(\bar{b}d) \rightarrow B^0(b\bar{d}) \rightarrow \bar{b}$

thus resulting in bb or $\bar{b}\bar{b}$, which can give like-sign (LS) dilepton events. The case when both of the $b\bar{b}$ mix does not change the event flavor and such events cannot be distinguished from unmixed decays. It is a relatively small effect for B_d mixing because of the smallness of the mixing probability. For pure $B_s^0\overline{B}_s^0$ events, the effect is large since the mixing is close to maximum.

It's clear that the like-sign dileptons are the signal for mixing. For the ideal case, the LS/OS charge ratio R is related to the mixing probability by

$$R = \frac{2\chi(1-\chi)}{[(1-\chi)^2+\chi^2]}$$

where χ was defined in Chapter 1 as the mixing probability averaged over all possible B hadrons produced,

$$\chi = \frac{prob(b \rightarrow \overline{B}^0 \rightarrow B^0 \rightarrow \ell^+)}{prob(b \rightarrow \ell^\pm)}.$$

The first complication arises from other sources of LS dileptons besides mixing. The cascade decay

$b \rightarrow c \rightarrow l^+$

gives positive leptons instead of negative ones. One such decay and one direct decay of the $b\bar{b}$ quarks will produce LS dileptons without mixing as,

$b \rightarrow c \rightarrow l^+$

$\bar{b} \rightarrow l^+$

Almost all B decays produce c quarks. The charmless B decays are an important aspect of B physics as they result from the b to u transition, which can provide more

information about the relevant CKM matrix elements. The current limit for charmless B decays is about 3% [31]. The average semileptonic branching ratio for c flavored hadrons is very close to that for B's. Therefore one expects as many LS dileptons as OS dileptons from $b\bar{b}$ decays. This could cause a serious physical background for the B tagging using leptons. However, leptons from direct and cascade B decays have several differences. The most important one is their P_T spectra. The cascade decay leptons have a P_T spectrum that is much softer than that from the direct decays. This is true for almost any cascade decays. The complicated decay path leaves less parent P_T for the final lepton. Applying a high P_T cut, (which in our case is 5 GeV for the electron and 3 GeV for the muon) strongly suppresses the cascade contribution. More studies are given in the next two chapters. The cascade leptons are usually less isolated. This is due to the small c quark mass compare to the b mass. Therefore, certain isolation requirements can also help in reducing the effect of this type of events.

Another major complication comes from the production and decay of $c\bar{c}$ final states. This only contributes to the OS dilepton sample. Even though the OS dileptons are not the direct mixing signal, measurement of the relative number of this kind of events is never the less important. As one can see from above formulae for R vs χ, it's the charge ratio, not the number of LS events itself that bears the full information of the mixing parameter. So one has to minimize OS dileptons from

non-B decays. The $c\bar{c}$ production cross-section in $p\bar{p}$ collisions is not measured at CDF energies. From perturbative QCD calculations, the production rate is as high as that for $b\bar{b}$. Give the similar semileptonic decay branching ratio, one expects the same amount of dileptons from $c\bar{c}$ as from $b\bar{b}$. Once again, the lepton P_T cuts help to reduce this contribution. Measurements have shown that the c quark has a very soft fragmentation spectrum. The hard fragmentation of the b quark gives its decay products relatively harder P_T than that of the c quark. (A detailed discussion of heavy quark fragmentation is given in chapter 5 in association with the Monte Carlo studies). From Monte Carlo studies, it is shown that c decays only account for about 10% of the inclusive electron sample at CDF, assuming almost the same quark level production cross-section.[28] The UA1 collaboration used muons to study the $b\bar{b}$ cross-section. [20] The isolation is another variable that can be used to reduce the $c\bar{c}$ contribution as one expects leptons from b decays should be more isolated than that from c decays due to the large mass difference.

In mixing analysis, we select all dilepton events resulting from b or c decays as the data sample. With different decay processes and their contributions modeled using Monte Carlo programs, the mixing parameter is extracted.

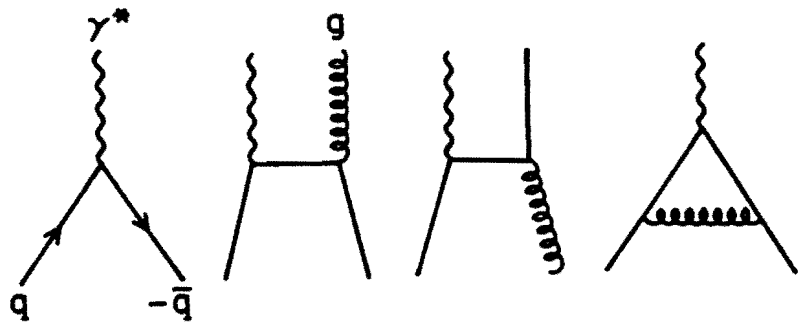

Figure 3.1: Feynman diagrams for Drell-Yan process.

3.2 Background Events for Mixing Measurement in the $e\mu$ Sample

We consider dilepton events not from b or c decays as background to the mixing data sample. For ee or $\mu\mu$ dileptons, the Drell-Yan (DY) process is an important example. In $p\bar{p}$ collisions, a quark and an antiquark can annihilate into a virtual photon as in the following diagram 3.1. The virtual photon leads to two opposite-sign leptons. The production cross-section for Drell-Yan process is about 10^{-4} of that of the $b\bar{b}$. However, the double branching ratio for both B decay to leptons and the P_T cut significantly reduce the dilepton cross-section from $b\bar{b}$. This makes the DY events a sizeable background. The main difference between DY leptons and leptons from B's is the isolation, which is usually defined as energy or charged track transverse momentum deposition in a cone around the lepton. It's clear from the production

mechanism that DY leptons should not be correlated with particles from underlying event. The heavy flavor decay leptons are less isolated because there are always other particles associated with the lepton in addition to the underlying event. By making a requirement that the lepton be non-isolated, the DY background can be reduced significantly.

Decays of heavy quarkoniums also produce OS ee or $\mu\mu$. These include J/Ψ, Ψ', $\Upsilon(1S)$, $\Upsilon(2S)$ and $\Upsilon(3S)$. The best way to eliminate these contributions is to impose invariant mass cuts around the resonances. The dimuon sample has another unique background. That's the cosmic ray contribution. Again, this only contributes to the OS sample and can be reduced by opening angle cone cut.

In this analysis, we use the $e\mu$ events, which are obtained by requiring one electron and one muon in the same event. Such events do not have direct Drell-Yan or meson decay background. The production rate of $e\mu$ from $b\bar{b}$ decay is almost twice that of ee or $\mu\mu$ alone. Such advantages make the $e\mu$ events the best sample for a $B^0\overline{B}^0$ mixing measurement.

One physical background for $e\mu$ can come from $\tau^+\tau^-$ Drell-Yan. The production rate is suppressed slightly at the mass range we are interested in (5 GeV $\leq m_{e\mu} \leq$ 25 GeV) relative to ee or $\mu\mu$ because of the large τ mass. The major contribution could be from $Z \rightarrow \tau^+\tau^-$ decays. At CDF, the number of Z production and decay into the e^+e^- channel in the central detector is less than 500 taking into account of the

detector acceptance and efficiency. Given the τ decay to e or μ branching ratio of 7% and the P_T cut, the contribution to $e\mu$ events from Z to $\tau^+\tau^-$ is clearly very small, about 5 events or less than 1% of the $e\mu$ data sample (see Chapter 5). Another possible source of physical background arises from the production and decay of J/Ψ's in a B event. If one B hadron decays semileptonicaly, while the other B decays to a J/Ψ which subsequently decays to dilepton pair, one would have three leptons in the final state. If one of the leptons from J/Ψ decay is not observed due to the detector acceptance or P_T cuts, this will give a dilepton event which has no charge sign correlation. In the next chapter, we'll study this process in some detail. The conclusion is that the contribution from such a process is negligible. Light Higgs (H_0) and exotic particles (e. g. leptoquark) can also decay to $e\mu$. If the Higgs is greater than $2m_\tau$ while still less than $2m_b$, $H_0 \rightarrow \tau^+\tau^-$ would be the main decay channel. Subsequent decays of τ's can produce $e\mu$ events. Such events will be highly isolated. The Higgs production cross-section is about 200 pb for 10 GeV Higgs mass at $\sqrt{s} = 1.8$ TeV, which is dominated by the gluon fusion process shown in figure 3.2. [23] Even for a light Higgs boson, the contribution is negligible. The SM Higgs is limited to be heavier than 48 GeV by the LEP experiments. For Higgs masses above twice the b mass and below twice the W mass (given $m_t \geq m_W$), the main decay channel for Higgs will be $b\bar{b}$. This is the signal for mixing measurement.

The main background for $e\mu$ events is from hadrons that fake leptons. With

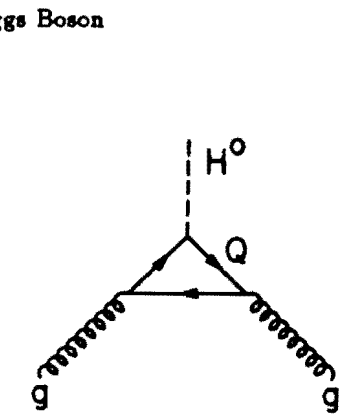

Figure 3.2: Higgs production via gluon fusion.

to the fact that the efficiency of the CDF system is poor for non-isolated electrons while electrons from b decays are usually not so well isolated. The lowest muon trigger threshold was 3 GeV, so the rate of dimuons is higher even with a relative small muon chamber coverage. However, the dimuon channel suffers from large background. This is mainly because the muon identification at CDF during the 88-89 run is not as good as for the electrons. The calorimeter provides only about 5 interaction lengths in the central region. Hadron punch-through is significant for muon events. The $e\mu$ events provides a large statistics sample while has relatively small background fraction. In the following sections, we first discuss in some detail electron and muon identifications at CDF for the 88-89 run, then we discuss the $e\mu$ event selection.

provides a large statistics sample while has relatively small background fraction. In the following sections, we first discuss in some detail electron and muon identifications at CDF for the 88-89 run, then we discuss the $e\mu$ event selection.

3.3 Electron Identification

An electron candidate is defined as a calorimeter energy cluster with a large EM energy fraction and associated with a high P_T track. The ratio of hadronic calorimeter energy (Had) over electromagnetic energy (EM) is used to define an EM cluster for electron or photon candidates. The trigger level requirement is Had/EM ≤ 0.125. This corresponds to a particle depositing 89% of its energy in the EM calorimeter before it reaching the hadron calorimeter. A tighter cut on this quantity to be less than 0.04 was imposed in the offline reconstruction and data selection. This is one of the most important cuts in distinguishing electrons or photons from hadrons. The Had/EM spectrum for a sample of W electrons is shown in figure 3.3.

The track requirement rejects photon candidates and neutral hadrons. The most important selection cut that requires tracking information is the E/P cut. This is the ratio of calorimeter energy of a given cluster over the track momentum associated with that cluster. For electrons, this ratio is known from Monte Carlo studies and measurement of W electrons to be slightly higher than 1. The reason why it does not equal unity is that high energy electrons radiate. The tracking chamber only

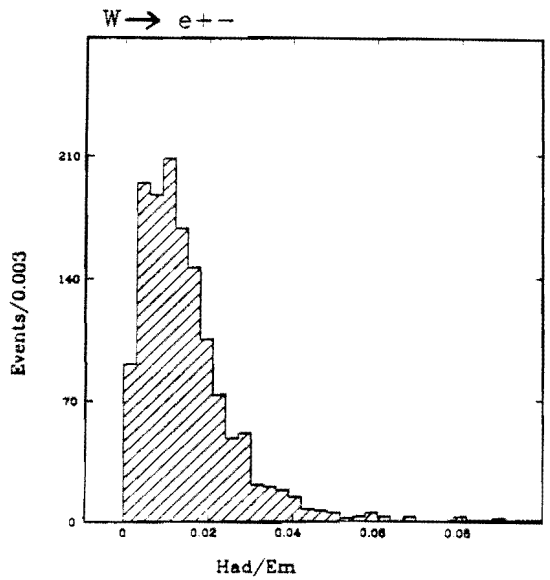

Figure 3.3: Had/EM spectrum for W electrons.

measures the momentum of the electron while the calorimeter typically measures the total energy of the electron and the photon. The distribution for the W electron sample is shown in figure 3.4. A cut of $0.07 \leq E/P \leq 1.4$ is imposed to ensure the E/P within the range of good electrons. This cut reduces fake electrons from charged hadrons and charged pions overlapping neutral pions.

Both the Had/EM and E/P cuts imply some isolation requirements. First, an electron has to be isolated to a certain degree to be identified as an EM cluster. Electrons embedded in jets would usually fail the Had/EM cut. Second, the $E/P \simeq 1$ requires that there can not be many tracks associated with that cluster. Therefore, the Had/EM and E/P cuts are correlated to some extent. Although the implicit isolation lowers the efficiency in electron identification, it helps to reduce the $c\bar{c}$ to

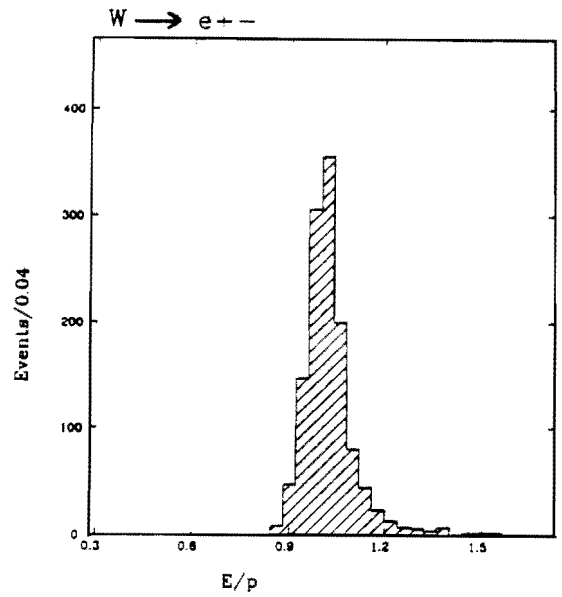

Figure 3.4: E/P distribution for W electrons.

$b\bar{b}$ fraction. Another track requirement used is that there must be one and only one track pointing to the EM cluster cell. This requirement reduces electrons from photon conversions and also requires the EM cluster to be more isolated. For mixing measurement, it also reduces the possibilty of charge confusion.

Several χ^2 type cuts have been applied to remove candidates that are not consistent with electrons. One quantity, generally referred to as L_{share}, is a measurement of the lateral shower profile for electron candidates in the central calorimeter [21],

$$L_{share} = 0.14 \sum_k \frac{M_k - P_k}{\sqrt{0.14^2 E + (\Delta P_k)^2}}$$

where the sum is over towers in the cluster surrounding the seed tower, M_k is the measured energy in these towers, P_k is the expected energy from testbeam data given

the shower position in the calorimeter, E is the EM energy in the cluster, and ΔP_k is the error in P_k. The first term in the denominator represents the resolution of the CEM. This quantity describes the matching between the e candidate shower profile as measured by the calorimeter segments and that for real electrons from testbeam study. The reconstruction requires an electron candidate to have L_{share} less than 0.3. A further cut of 0.2 on this quantity is applied in the final $e\mu$ sample.

The Central Strip chamber (CES) embedded in the central EM calorimeter measures shower shapes in two directions (strip and wire) transverse to the shower direction. Testbeam studies show that electrons have rather distinctive shower profiles compared with other particles (π^0 and charged hadrons). In the offline production, a fit of the data to the testbeam results was made, which gives two χ^2 for the two shower shapes measured for each candidate. One is from strip measurement, the other is from the wires. The strips and wires are orthogonal to each other, and therefore provide two independent measurements. A cut is made on the averaged $\chi^2 = \sqrt{{\chi^2_{strip}}^2 + {\chi^2_{wire}}^2}$.

Shower position matching cuts are also imposed using the track direction measured in the CTC and the shower $r\phi$ and z positions measured by the CES. The high resolution of the CTC and CES enables very good matching cuts. Furthermore, to ensure the best response of the calorimeter, a cut is made to avoid calorimeter cell boundaries, cracks between modules and certain towers that do not behave regularly.

The above cuts reject non-electron background, such as hadrons and photons. There is another source which gives real electrons but has nothing to do with heavy quark decays. These are the conversion electrons. Photons or π^0's passing through the materials before the calorimeter decay into e^+e^- pairs. It has been studied that such electrons contribute to a significant fraction of real electron events ($\sim$ 20%) [28]. The conversion electrons can be rejected using track information from the CTC and VTPC. There are several methods to identify conversion events. The following method is used in this analysis and some other analyses [21].

The VTPC measures charged particle tracks down to very small radius, inside which there is little material left. If a photon or a π^0 decays outside the VTPC, there will be no hit inside. Electrons from this kind of decay are called outer conversions. Measurements using W and Z electrons show that the efficiency for charged particle tracking in the VTPC is very high ($\simeq$ 98%). Requiring a high VTPC occupancy removes outer conversion effectively. For those conversion electrons that originated before the VTPC, there is another quantity to use. This is the e-track invariant mass cut. Conversion electrons are produced in pairs with zero invariant mass. The CTC measures track momentum for P_T as low as 140 MeV. By looping over all tracks with the electron candidate, the lowest e-track invariant mass can be found. If it is smaller than 0.5 GeV, that electron is considered as a conversion candidate and removed. This cut also removes outer conversion events that are not removed by

the hit fraction cut. If an event fails either cuts, it is rejected. The efficiency of this algorithm for identifying conversion electrons has been measured be about 85% or higher while the over-efficiency (removing good electrons) has been shown to be small (5%) [21].

Some of the requirements described above can only be applied to the central detector, such as the CES requirements, L_{share}. For other part of the detector, electron identification is not as good as in the central region. The electron samples and the final $e\mu$ sample all require central electrons only. An analysis of inclusive electrons for a b quark cross-section measurement yielded a prompt electron fraction of about 65%, which provides a good sample for study B physics in the semileptonic channel [28]. For the $e\mu$ event selection, we now discuss muon identification at CDF.

3.4 Muon Identification

Muons can be identified through their ability to penetrate a large amount of material characterized by the hadron interaction length. Hadrons can interact with the nuclei via strong interaction and lose their energy in the process. Leptons interact with the material via bremsstrahlung or ionizing lose. High energy electrons lose their energy mainly through bremsstrahlung. The generated photons form e^+e^- pairs and continue the same process, forming an electromagnetic shower. This process reduces the electron energy faster than the hadron's energy. It is the reason for the Had/EM

cut in electron identification. The muon is much heavier than the electron. At CDF energy, it loses its energy mainly through ionization. This enables it to penetrate a longer thickness of material than a hadron or electron. For this reason, high energy muons can be identified as minimum ionizing particles.

For this analysis, only muons detected by the central muon chamber (CMU) are used. The CMU covers $|\eta| \leq 0.63$. The minimum calorimeter interaction length is 4.9. Three or more hits associated with a charged particle that goes into the muon chamber (which is a 4 layer streamer tracking chamber as described in the last chapter) will be considered as a muon stub. At trigger level, such a muon stub matched by a track with P_T greater than 3 GeV is required to keep the event. In the offline reconstruction and the following data selection, more stringent track requirements, matching cuts and minimum ionizing cuts are applied.

We first discuss the track quality cuts which have been used for muon selection and background studies. The CTC measures charged particle tracks with high precision ($\delta P_T/P^2 \sim 0.0017$) and high efficiency. First, to ensure good track measurement, at least 50 hits out of the 84 tracking wire layers are required for a good track. The transverse impact parameter, or the distance of closest approach of the track to the beam line (DCA) is required to be less than 0.5 cm. The track vertex component along the beam direction (Z_{trk}) is required to be within 5.0 cm of the event vertex (Z_{vtx}). These cuts exclude tracks that are not coming from the collision point. A P_T

cut of 3 GeV on the track is applied as in the muon trigger.

For muon candidates, a minimum ionizing cut requires that there be less than 2 GeV energy deposited in the EM calorimeter and no more than 4 GeV in the hadronic calorimeter. Muons on the average leave 0.3 GeV in the EM calorimeter and 1.2 GeV in the hadron calorimeter. The energy deposition curve for muons should have a Landau shape. The calorimeter energy distributions in the tower that the muon passes (muon tower) for the $J/\Psi \rightarrow \mu^+\mu^-$ sample (at least 90% real muons) are shown in figure 3.5 and 3.6. Muons going through the calorimeter must leave some energy, so there is also a requirement that a muon deposit at least 0.1 GeV in the EM and hadronic calorimeters. The peak at zero is an artificial effect due to an error in the production code where calorimeter energy less than a certain value has been set to zero.

Two matching cuts are imposed for the muon candidates. One was imposed at the reconstruction stage. This is the CTC/CMU position matching in the direction which is perpendicular to the beam axis (x direction at CDF), or the CMU sense wire direction. The matching is degraded by the Coulomb scattering of the particle through the calorimeter. Muons from kaon or pion decay-in-flight usually exhibits some mis-match due to the change of momentum and flight direction. Charged hadrons that are not completely absorbed by the calorimeter (called hadron leakage) can result in a muon stub having a large mis-match with the original track. Therefore, the matching

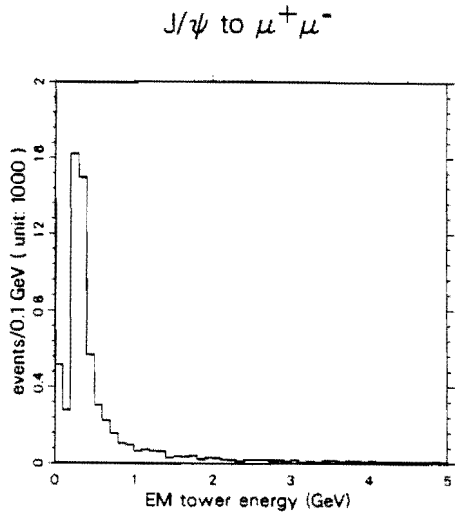

Figure 3.5: EM tower energy for J/Ψ muons.

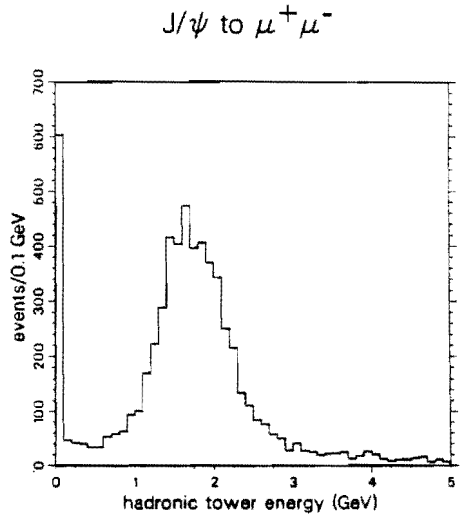

Figure 3.6: Hadronic tower energy for J/Ψ muons.

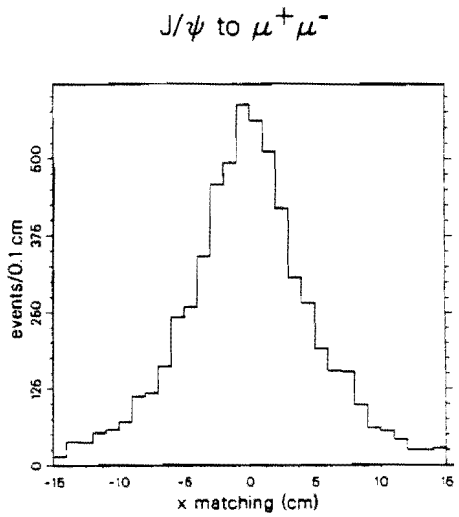

Figure 3.7: Δx matching for J/Ψ muons.

cut can help reducing these background muon candidate events. The x-matching for the J/Ψ muons are shown in figure 3.7. A cut is made on the CTC/CMU matching χ^2 using both position and angle matching. The reconstruction package searches for a track that is best matched to the CMU muon stub. Minimum ionizing particles will have a χ^2 distribution for two degrees of freedom so that a negligibly small number will have $\chi^2 \geq 12.0$. However, large χ^2 muon candidates are found with a an almost flat distribution. These events are either from hadron leakage, decay-in-flight or muons that have been badly scattered. One expects the non-interacting punch-through particles to behave the same way as real muons. So, a cut on χ^2 does not reject such background. The χ^2 distribution for J/Ψ muons are shown in figure 3.8.

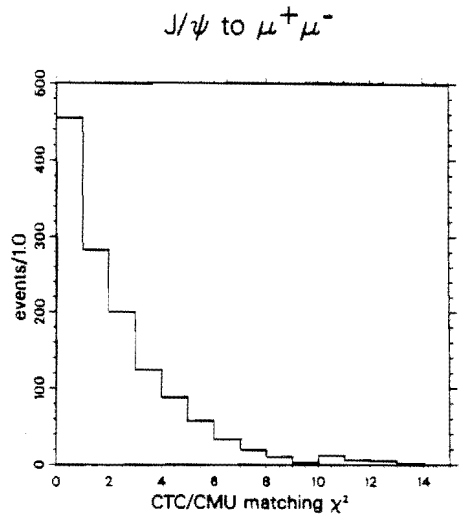

Figure 3.8: CTC/CMU matching χ^2 spectrum for J/Ψ muons.

4.) cosmic ray muons. A cosmic ray background usually gives two opposite-sign back-to-back muons, which can be reduced by imposing a opening angle cone cut.

While the hadron leakage and decay muons can be reduced by the matching cuts, there is no effective way to reduce the non-interacting punch-through contributions. This kind of background looks exactly like real muons except their contribution goes down as the effective hadron interaction length goes up, as in the case where a track has a larger η. The only way to reduce non-interacting punch-through is by adding more shielding materials before the muon chamber. Not being able to remove this contribution, one can only estimate its fraction by various methods.

While the hadron leakage and decay muons can be reduced by the matching cuts, there is no effective way to reduce the non-interacting punch-through contributions. This kind of background looks exactly like real muons except their contribution goes down as the effective hadron interaction length goes up, as in the case where a track has a larger η. The only way to reduce non-interacting punch-through is by adding more shielding materials before the muon chamber. Not being able to remove this contribution, one can only estimate its fraction by various methods.

3.5 Electron-muon Event Selection

With the electron and muon identification criteria discussed above, an $e\mu$ data sample is selected. The central electron and muon selection criteria used for the $e\mu$ data sample are listed in the table 3.1. In addition to these cuts, the event |z vertex| is required to be less than 60 cm. This ensures that the event is well covered by the detector and is consistent with the measured Gaussian distribution for the event vertex with mean of -1.0 cm and width of 35 cm [22]. Electron candidates are required to be in the EM calorimeter fiducial region. Conversion electrons are removed using the algorithm discussed above. The VTPC hit fraction is required to be larger than 0.5 and the minimum e-track pair mass be greater than 0.5 GeV. For best charge measurement, we require one and only one 3D track be associated with the electron candidate. A cut on missing transverse energy ($\not{E}_T$) to be less than 15 GeV is applied

Table 3.1: Electron-muon selection criteria.

e	μ
$E_T \geq 5$ GeV	$P_T \geq 3$ GeV
Had/Em≤ 0.04	EM tower ≤ 2.0 GeV
E/P≤ 1.4	Had tower ≤ 4.0 GeV
Lshare ≤ 0.2	EM + Had ≥ 0.1 GeV
$\Delta(r\phi) \leq 1.5$ cm	x match ≤ 10.0 cm
$\Delta(z) \leq 2.5$ cm	CTC/CMU fitting $\chi^2 \leq 10.0$
averaged CES $\chi^2 \leq 10.0$	# of CTC hits ≥ 50
	track DCA ≤ 0.5 cm
	$\lvert Z_{trk} - Z_{vtx}\rvert \leq 5.0$ cm

for all events to remove possible background from W plus jets production where tracks in jets can fake a muon. The missing E_T is measured by the imbalance of the total calorimeter energy including the muon momentum contribtution. Leptonic W decays always have a neutrino that carries away a large fraction of the transverse energy. Therefore, missing E_T is a good signal for W production. In addition to these selection cuts, all suspected bad runs are not used in this analysis. A bad run is a data taking run when a bad performance of detector is identified so all or part of the data taken from the run is distrustful.

There are 1340 $e\mu$ events that pass all the criteria. A large fraction (1150 or 86%) of this sample comes from the central electron 5 GeV and central muon 3 GeV trigger. This trigger was implemented in January 1989 and has about 2.7 pb^{-1}. Other events come from various other triggers, such as the inclusive lepton, jet and photon triggers. Among the 1340 events, 429 are like-sign while 911 are opposite-sign.

To study the selection cuts, we plot the corresponding quantities without making the cut except that in some cases the cut has been made at reconstruction or event stripping level. All other cuts are applied. For the electrons, the Had/EM and E/P distributions are given in figure 3.9 and 3.10. The CTC/CES matching quantities are shown in figure 3.11. The strip versus wire shower profile matching χ^2 is given in figure 3.12.

For muons, the EM and hadron tower energy are shown in figure 3.13 and 3.14. The x-matching is shown in figure 3.15 and the CTC/CMU matching χ^2 is given in figure 3.16. The track quality cuts are shown in figure 3.17.

It's clear from these plots that the cuts are reasonable in keeping the $e\mu$ signal while reducing backgrounds. After this selection, the $e\mu$ event structure can be studied.

The $e\mu$ azimuthal opening angle ($\Delta\phi$) and invariant mass distributions for the 1340 events are shown in figure 3.18. The high peak in the low invariant mass region for the OS events is patially due to single b sequential decays to e and μ, *i.e.*

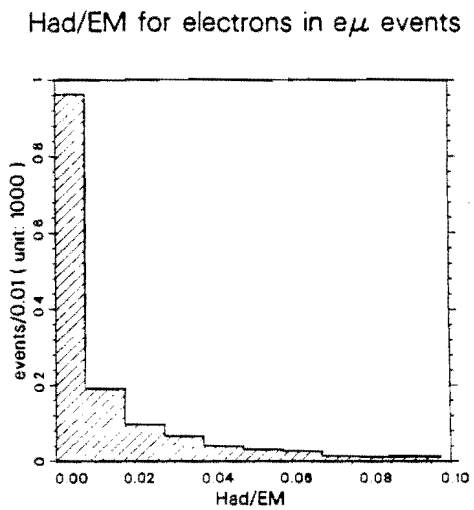

Figure 3.9: Electron Had/EM distribution for $e\mu$ candidates.

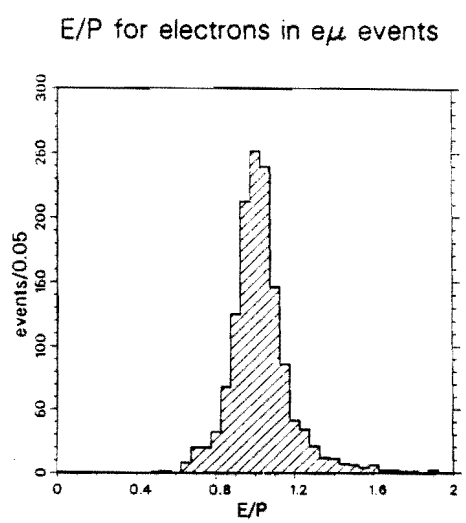

Figure 3.10: Electron E/P distribution for $e\mu$ candidates.

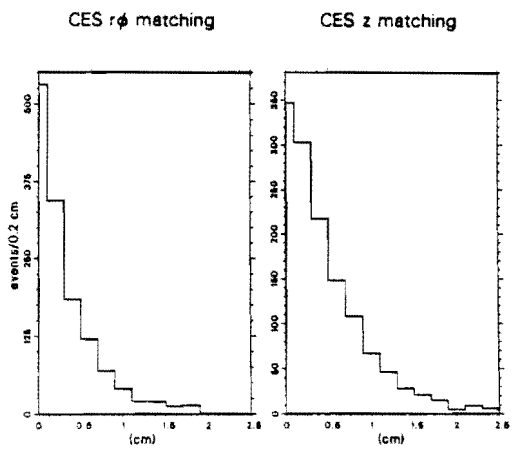

Figure 3.11: Electron CTC/CES matching in $r\phi$ (left) and z (right) for $e\mu$ candidates.

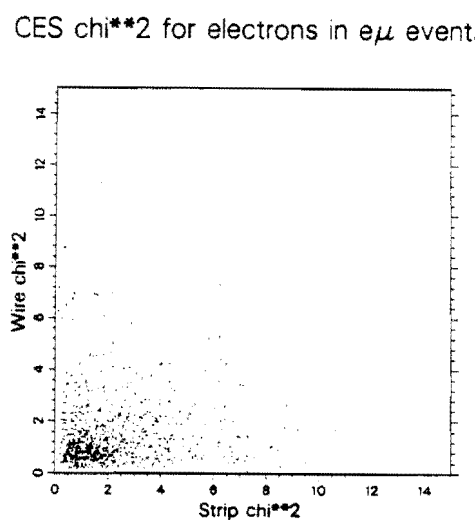

Figure 3.12: Electron shower profile fitting χ^2: strip vs wire from CES for $e\mu$ candidates.

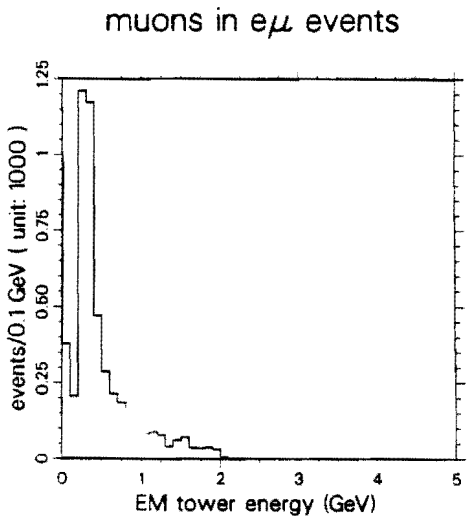

Figure 3.13: Muon EM tower energy distribution for $e\mu$ candidates.

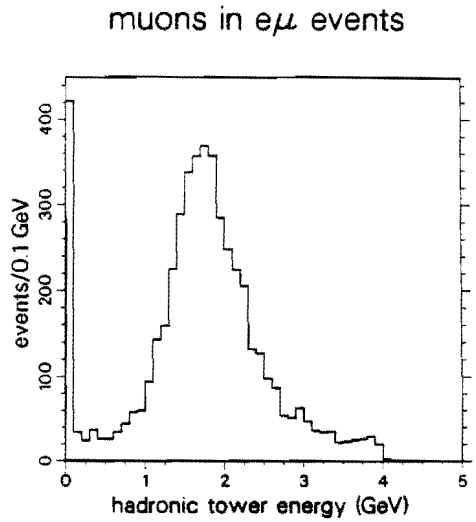

Figure 3.14: Muon hadronic tower energy distribution for $e\mu$ candidates.

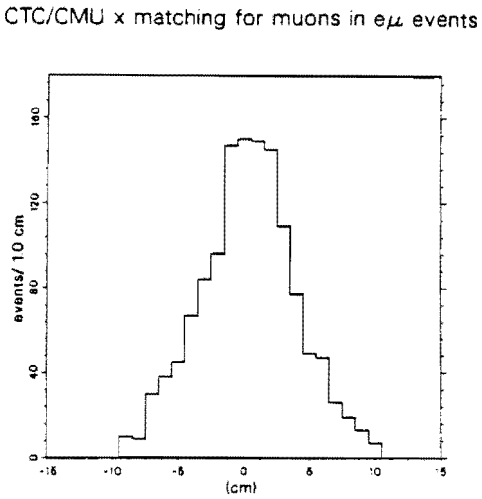

Figure 3.15: Muon x-matching distribution for $e\mu$ candidates.

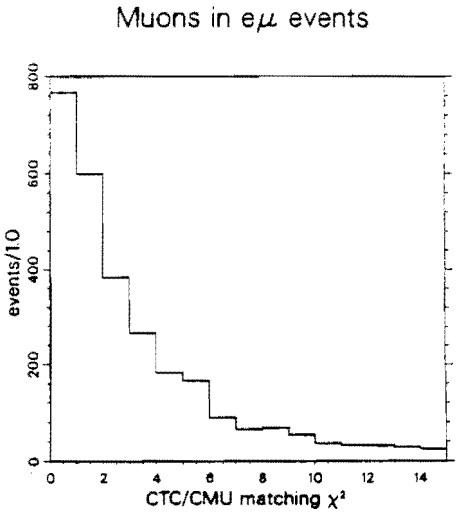

Figure 3.16: Muon CTC/CMU matching χ^2 distribution for $e\mu$ candidates.

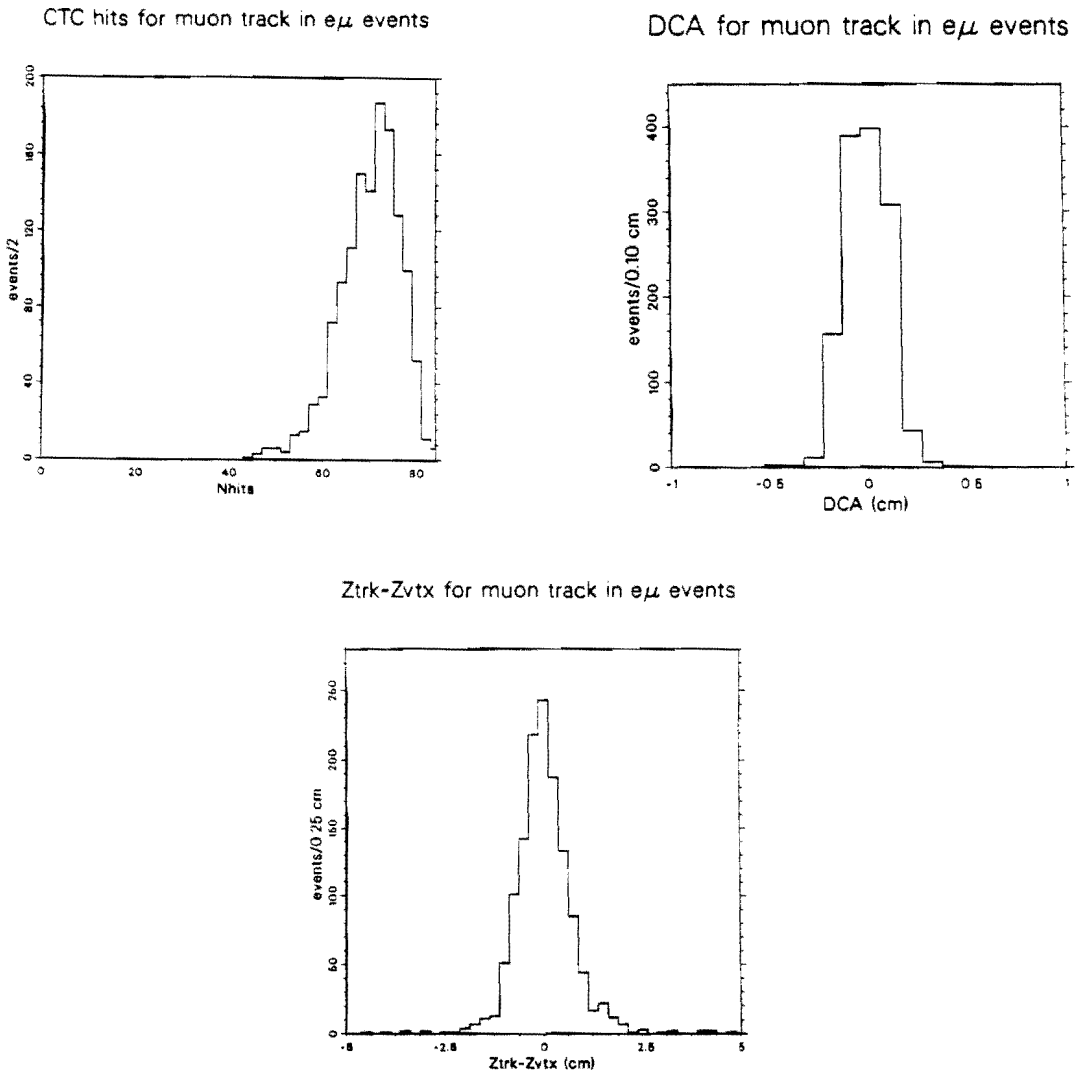

Figure 3.17: Muon track qualities: CTC hit distribution; distance of closest approach (DCA); track vertex to the primary vertex (z component).

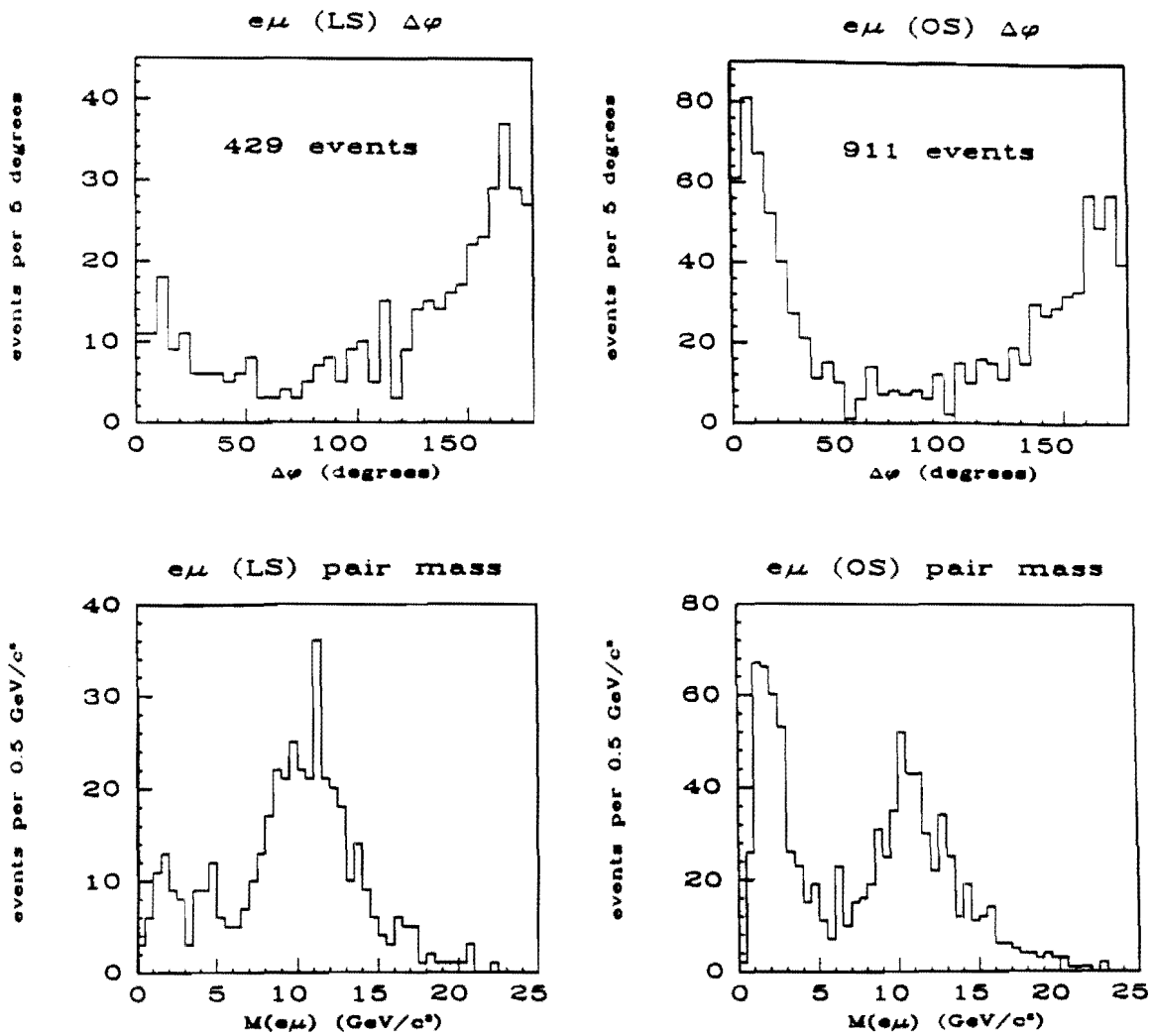

Figure 3.18: $e\mu$ data azimuthal opening angle and invariant mass distributions for like-sign and opposite-sign events.

$b \rightarrow e^- c\bar{\nu}_e \rightarrow e^- \mu^+ s\bar{\nu}_e \nu_\mu$. Such events typically have small invariant mass and opening angle. These two quantities are highly correlated as shown in figure 3.19. The $e\mu$ invariant mass distribution for single b decays from Monte Carlo is shown in figure 3.20 at generator level. The same distribution is shown in figure 3.21 after full detector simulation. The generator level plot with high statistics shows that the single B contribution disappears around 4.0 GeV. The detector simulation reduces events due to acceptance and resolution, but the smearing does not seem to be important. By applying an invariant mass cut at 5.0 GeV, the single B events are removed.

This cut removes events with small $e\mu$ opening angle, as seen in figure 3.19. Therefore, $b\bar{b}$ events from high order processes such as gluon splitting ($p\bar{p} \rightarrow g \rightarrow b\bar{b}$) are also reduced. This reduces the signal but also limits the high order contribution and so the uncertainties in generating such events. More discussion will be given in chapter 5. The same cut is also applied for LS events to maintain the same selection criteria for each $e\mu$ event. Another consequence of this cut is that the $e\mu$ opening angle is large ($\geq 45^o$), thus eliminating $b\bar{b}$ events in which the e and μ overlap.

After this cut, the final $e\mu$ sample for $B^0\overline{B}^0$ mixing measurement is obtained. The opening angle distributions for this sample are given in figures 3.22. The E_T^e vs P_T^μ distribution is given in figure 3.23. The LS/OS event numbers and ratio R for different P_T thresholds, after the invariant mass cut, are listed in table 3.2. In particular, there are 346 LS and 554 OS events with $E_T^e \geq 5$ GeV and $P_T^\mu \geq 3$ GeV

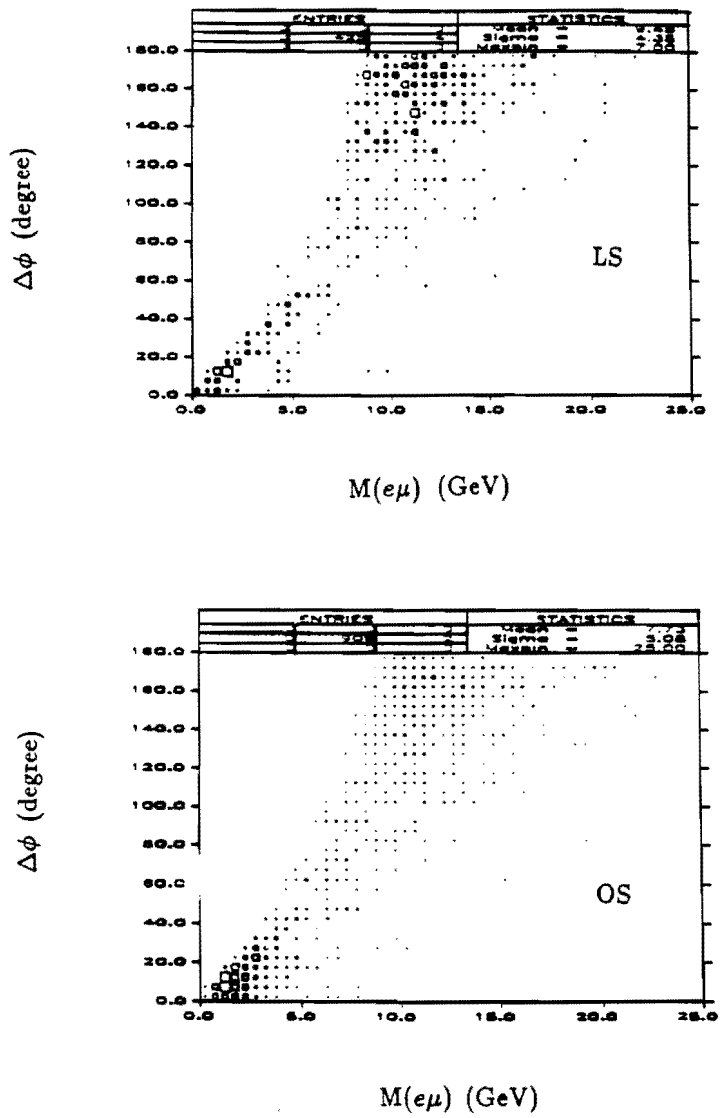

Figure 3.19: $e\mu$ azimuthal opening angle vs invariant mass for LS (top) and OS (bottom) events.

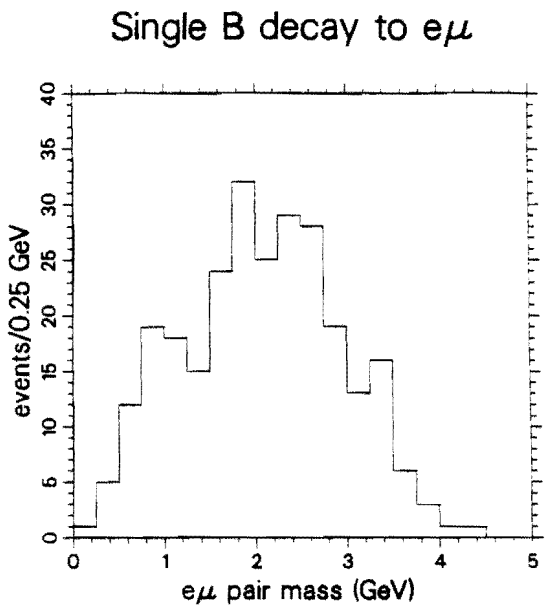

Figure 3.20: $e\mu$ invariant mass for single B decays at generator level Monte Carlo.

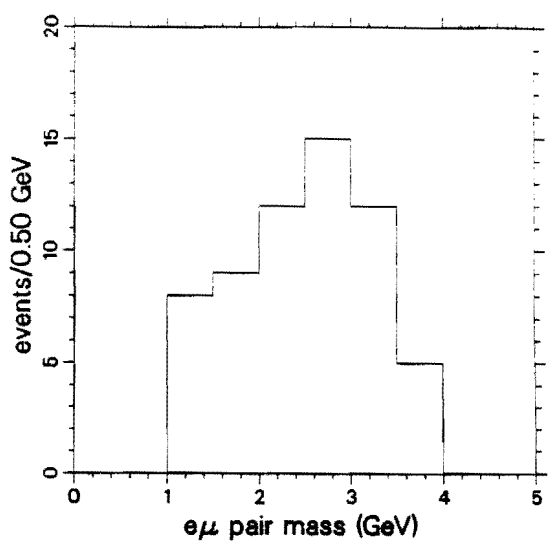

Figure 3.21: $e\mu$ invariant mass for single B decays from full Monte Carlo.

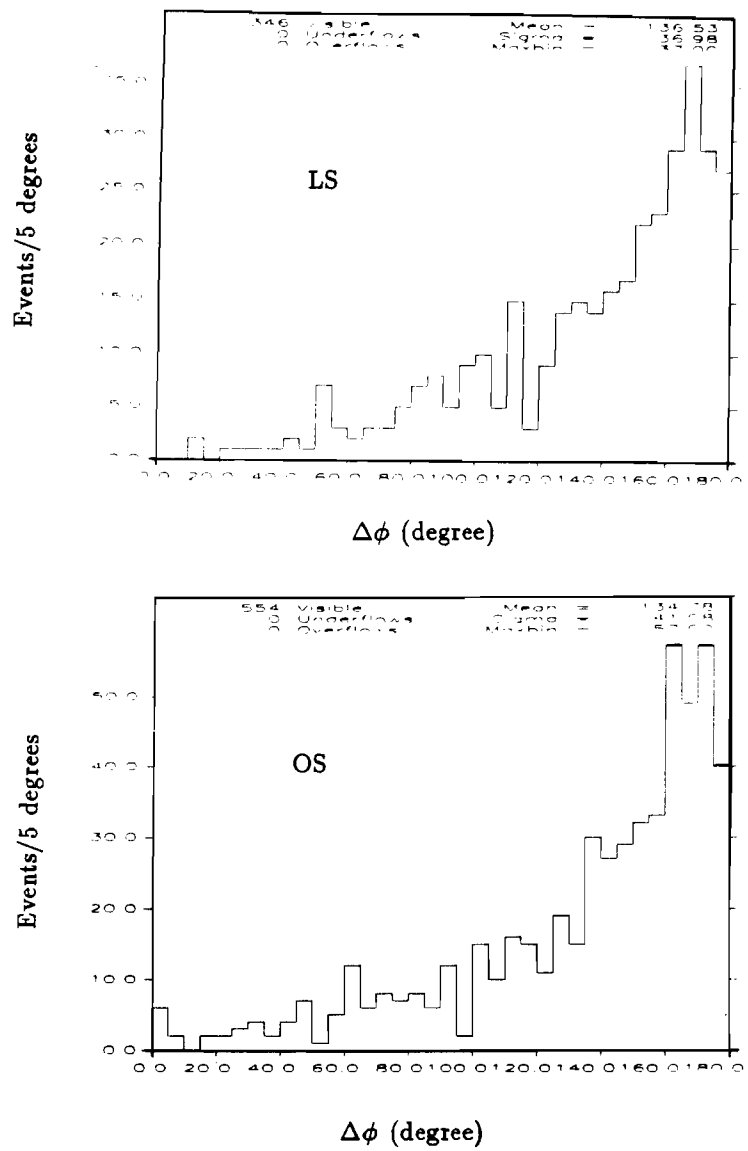

Figure 3.22: $e\mu$ opening angle after the invariant mass cut.

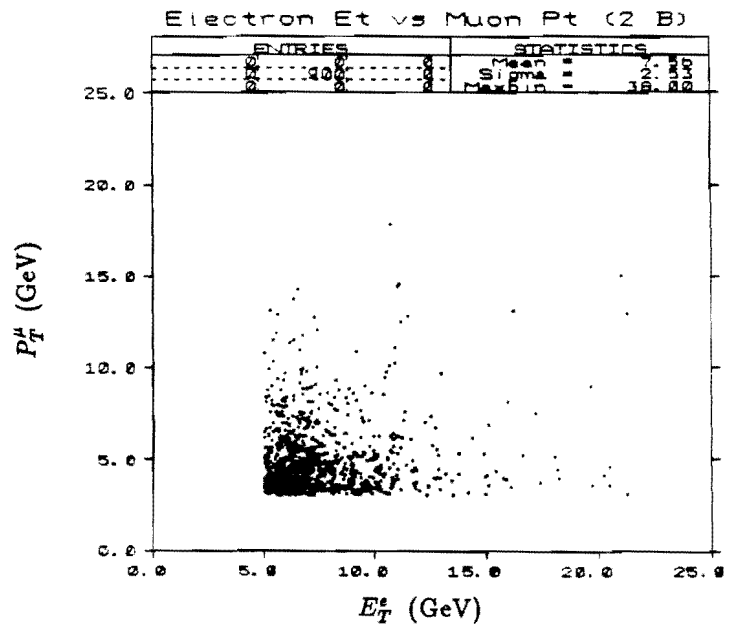

Figure 3.23: E_T^e vs P_T^μ after the invariant mass cut.

in the data. The LS events from second generation b decays have a softer lepton P_T spectrum. For higher P_T thresholds, the contribution to LS events from non-mixing source (sequential decays) are reduced relative to the OS events, resulting in smaller values of R. The trend in the table agrees with such an expectation. Background subtraction has not been done for the numbers in table 3.2.

In order to determine the charge ratio R for the mixing measurement, one has to know the background fraction in this final data sample and the charge ratio in the background. This is the subject of the next chapter.

Table 3.2: Final $e\mu$ sample.

E_T^e(GeV)	P_T^μ (GeV/c)	R (data)
5	3	346/554 = 0.623
5	5	109/197 = 0.553
7	3	156/246 = 0.634
7	5	51/ 94 = 0.542
5	7	43/ 72 = 0.597
7	7	19/ 33 = 0.576

Chapter 4

Background Estimation

In this analysis, all $e\mu$ events from $b\bar{b}$ or $c\bar{c}$ decays are considered to be signal. As mentioned in the introduction, other physics processes, such as $\tau^+\tau^-$ Drell-Yan, which can contribute to real $e\mu$ events have very small production rates compare to the signal rate. Therefore, the main background to be considered is from fake electron, fake muon or both fakes. Fake leptons defined here include all lepton event candidates not resulting from b or c decays. Thus, muons from kaon or pion decays, electrons from photon conversions are included in the fake lepton catagory. For clarity in the discussion, we first divide the fake $e\mu$ background into three categories:

1.) real e, fake μ

2.) fake e, fake μ

3.) fake e, real μ

The sources of fake muons were discussed in the muon identification section of last chapter. Since we are only interested in charged partilces, the fake background is

proportional to the number of tracks seen by the triggers collecting the data sample. That is, each track has, on average, a probability to fake a lepton. This leads to a meaningful rate of muon candidates per track. Since we have tight requirements on the muon track, all tracks that can fake a muon must also satisfy these requirements. The following background estimation method originated from this consideration. Note, the fake background is not necessarily proportional to the number of events seen by the triggers because the track multiplicity for different event types can be very different.

Fake electrons can come from hadrons, conversions or photons overlapping with a charged particle ($\pi^{\pm}$, etc.). For the last case, photons give rise to a small Had/EM, while the charged particle provides a track to match the photon EM cluster. Early showering of charge pions or charge exchange effect can all contribute to fake electron events. Any charged particle detected by the muon chamber will be considered a muon candidate. So charged hadrons penetrating through the calorimeter will lead to a fake muon event. Light hadrons (K, π, ρ, etc.) can decay to muons on its fight path. These are also considered to be fake muon events in this analysis.

For this analysis, only the overall background fraction is important. It is not necessary to determine each background category separately. In the next section, we'll discuss a method that estimates the total background fraction.

4.1 Method of Background Determination

Given the fact that the fake background can be directly related to the number of tracks in a event sample, the lepton candidates per track rate can be used in certain situations for background estimation. For example, to determine the background in an inclusive muon sample, if we know the number of fake muons per track, i.e. the probability for a track to fake a muon on average, and given the total number of tracks involved, we can estimate how many fake muons are expected in the sample. However, in this case, one has to know the total number of tracks in all $p\bar{p}$ collisions that give rise to the inclusive muon sample. It is not possible in the case of single inclusive leptons to determine this number. The normalization sample is the minimum-bias sample and CDF did not collect the required huge minimum-bias sample to perform this measurement.

For dileptons, this method can apply. The normalization sample is the corresponding inclusive single leptons. The $e\mu$ sample is a good example for applying such a method. We first select a sample of inclusive electrons with the electron selection criteria defined in the $e\mu$ data selection. Then we look for muons and good track candidates. The number of good tracks times the muon per track rate defined below gives all three categories of fake background. The expected background event number over the total $e\mu$ events observed in the same inclusive electron sample is the background fraction for the $e\mu$ subsample.

To show this method clearly, we first define the muon candidates per track rate f_μ. This is the ratio of inclusive muons over all good tracks in minimum-bias events. The muons are required to pass all muon selection cuts defined before. The good tracks are defined by the track selection criteria for the muons, *i. e.* $P_T \geq 3$ GeV and the track quality cuts. To mimic the real muons, tracks are also required to point in the muon chamber fiducial region, which eliminates space that is not covered by the CMU chambers.

The muons from the minimum-bias sample include all possible sources: real muons from heavy quark semileptonic decays, fake muons from punchthrough, kaon or pion decays and cosmic ray muons. Therefore,

$$f_\mu = \frac{N_\mu}{T_{MBS}} = \frac{N_\mu^F + N_\mu^R}{T_{MBS}} = f_\mu^F + f_\mu^R$$

where N_μ is the number of muons in the minimum-bias sample, consisting of N_μ^R muons from heavy flavor decays and N_μ^F muons candidates from other sources (fake muons). Thus, f_μ^F is fake muon per track and f_μ^R is real muon per track in an unbiased sample. Muons from the minimum-bias trigger belong to a low P_T inclusive muon sample if such a trigger had been implemented. We expect that background in an inclusive muon sample goes down as the P_T cut goes up. This is because decay background is significantly reduced as P_T goes up while punchthrough contribution is relatively independent on P_T above a certain threshold (see figures 4.4 and 4.5). The large background fraction in the high P_T inclusive muons indicates that most of the

low P_T minimum-bias muons are background. Therefore, f_μ^F dominates. Note, this muons per track number also includes real muons. This is for the fake e and real μ fraction of the background. We do not expect that fake electron events with $E_T \geq 5$ GeV have a different heavy quark fraction than minimum-bias events with a 3 GeV P_T track. The probability per track for observing a real muon from b or c decays in the fake e sample is thus close to that of the minimum-bias sample with a 3 GeV track.

To apply this rate in the inclusive electron sample to calculate the $e\mu$ background, one has to consider the possible differences between the tracks in the minimum-bias and the inclusive electron sample. Differences can arise due to a different K/π ratio, different track P_T spectra and possibly different jet activity in the two samples. These differences will be taken into account as systematic uncertainties, which we'll discuss later.

The number of tracks T_e in the inclusive electron sample is the total number of tracks that can lead to fake $e\mu$ events. Note that T_e also has two parts, one from real electron sub-sample (T_e^R) and the other from the fake electron sub-sample (T_e^F), i. e.

$$T_e = T_e^R + T_e^F.$$

Multiply T_e by f_μ, we get

$$T_e \bullet f_\mu = (T_e^R + T_e^F)(f_\mu^F + f_\mu^R) = T_e^R f_\mu^F + T_e^F f_\mu^F + T_e^F f_\mu^R + T_e^R f_\mu^R$$

On the right side of the equation, the first term is the number of real e fake μ events expected, the second term gives fake e fake μ and the third term is the fake e real μ events expected. The last term is an over-estimate, which arises from multiplying the real muon per track rate f_μ^R to the number of good tracks in the real electron sub-sample. This part does not belong to the background.

As one can see, the number of good tracks in the inclusive electron sample multiplied by the inclusive muon per track rate gives the total number of background events from all 3 categories with some over-estimate. The ratio of this number of background events to the total number of $e\mu$ events observed in the same inclusive electron sample gives the fraction of background for the $e\mu$ data. If f_μ is dominated by fakes, the over-estimate shall be small. (see section 4.4)

4.2 Muon per Track Rate f_μ

In order to determine f_μ, we take the full CDF minimum-bias event sample. Good tracks and muon candidates are selected according to criteria defined above. In about 278,000 events, we find 2959 good tracks and 8 muons with P_T above 3 GeV. Therefore, the inclusive μ per track rate f_μ is $8/2959 = 0.27\%$. The small number of muons and tracks observed is consistent with our tight selection. This also provides an example of how important it is to have a selective trigger to collect interesting events. Muon candidates that pass offline selection are only $8/278,000 = 2 \times 10^{-5}$ of

the collision rate. Other signals have even smaller yield.

Some of the track quality plots are shown in figure 4.1. Compared with the same plots for muon candidates from the $e\mu$ sample, one can see that they are very similar.

Different K/π ratios between minimum-bias and inclusive electron events can lead to a difference in f_μ between the two samples. This is because the punch-through and decay probability are different for kaons and pions.

Kaons have a relatively small interaction cross-section with nuclei, as shown in figure 4.2. This leads to a larger probability for kaons to punch-through. Also seen from figure 4.2 is the difference between K^+ and K^-. The positive kaons have an even smaller interaction cross-section than their negative partners. This effect shows up in the asymmetric charge ratio among punch-through kaons. A Monte Carlo study [26] of this charge asymmetry is shown in figure 4.3. This asymmetry is useful for a rough estimate of the background fraction.

The decay background also depends on the K/π ratio. Kaons have a larger decay probability. However, because of the large mass difference between the kaon and the muon, the decay daughter track usually has a distinctive P_T and forms a "kink" with the parent $K^\pm$. These features help to remove the decay muons since such tracks have a low reconstruction efficiency in the CTC and sizeable mis-match to the CMU stub. The pion decay probability is smaller, but the decays themselves are much harder to

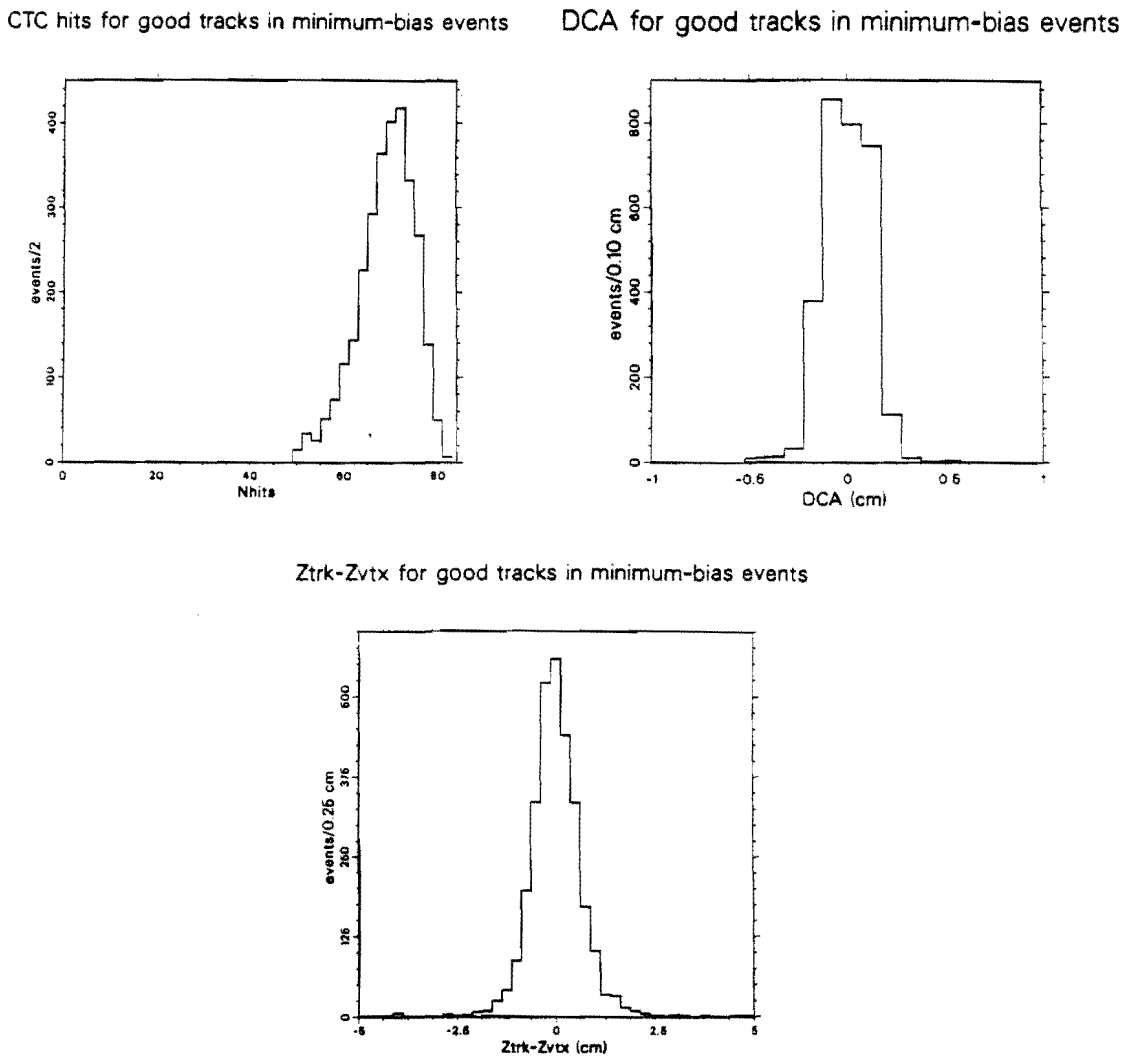

Figure 4.1: Minimum-bias event good track qualities: CTC hit distribution; distance of closest approach (DCA); track vertex to the primary vertex (z component).

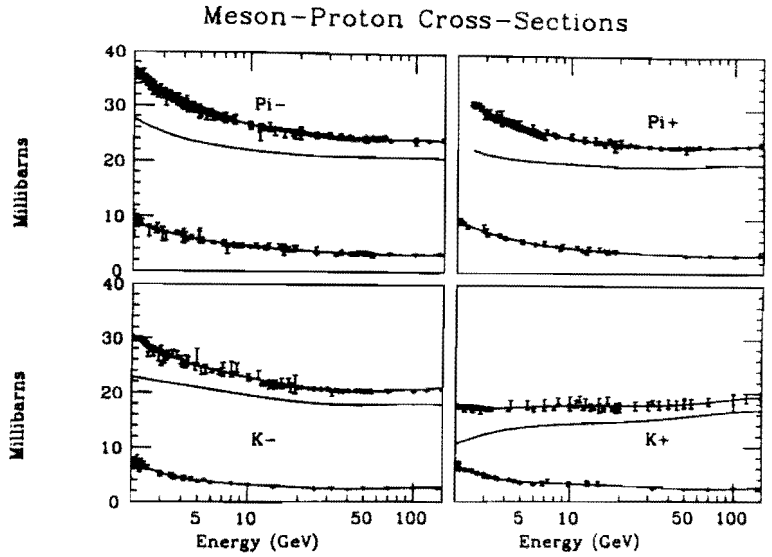

Figure 4.2: Interaction cross-section in steel for pions and kaons. In each plot, the top curve is for total cross-section, the bottom curve is elastic cross-section. The middle one is the difference between these two curves, representing the absorption cross-section.

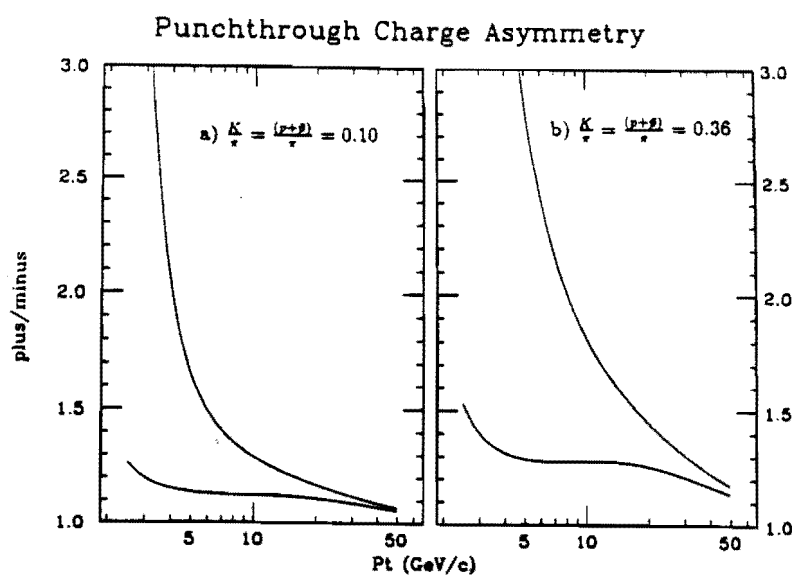

Figure 4.3: Charge asymmetry in punch-through kaons.

Table 4.1: Track punch-through probability with different K/π ratios.

K/π ratio	f_μ^P
0.12	$\eta_\mu \bullet 0.32\%$
0.24	$\eta_\mu \bullet 0.38\%$
0.36	$\eta_\mu \bullet 0.42\%$

distinguish from real muons in the CTC. Studies show that pion decay contributes as many background as from kaon decay [26].

To estimate the systematic error due to the K/π ratio difference, Monte Carlo simulation using real data tracks has been performed. To determine the effect of punch-through background, we take the good tracks in the inclusive electron sample, for a given K/π ratio, and calculate the interaction length for each track using the CDF central calorimeter interaction length parametrization [25]. The punchthrough probability is calculated for different K/π ratio before the muon detection efficiency is taken into account:

$$f_\mu^P = \eta_\mu \frac{\#\text{ of punch-through tracks}}{\#\text{ of trial tracks}}$$

where η_μ is the central muon detection efficiency.

Values of f_μ^P for different K/π ratio are given in table 4.1. The K/π ratio is varied between the known upper and lower limits for $P_T \geq 3$ GeV/c tracks in $p\bar{p}$

collision at $\sqrt{s} = 1.8$ TeV [27]. One can see that f_μ varies by 15% around its central value. A similar simulation study was made [26] for decay muons. In contrast to punch-through muons, decay muons are sensitive to the selection cuts used. For tight cuts as used in the $e\mu$ data selection, a variation of less than 15% is observed for decay muons. So, the total systematic error due to uncertainties in the K/π ratio is assigned as 15%. The variation of f_μ estimated this way provides an upper limit on the uncertainty of inclusive muon per track rate (f_μ) due to K/π ratio.

The same simulation is used for verifying the track P_T dependence of f_μ. At K/π ratio of 0.24, f_μ is not very sensitive to the track P_T distribution. This is because the meson scattering cross-section is a weak function of P_T as seen in figure 4.2. The P_T dependence of f_μ at $K/\pi = 0.24$ is given in figure 4.4 for non-interacting punchrough hadrons and in figure 4.5 for muons from kaon and pion decays. We assign a 20% error for using the f_μ, which is essentially determined at low P_T (3-5 GeV) from minimum-bias events.

The hadron activity in an electron event mainly effects leakage background. First, this kind of background can be significantly reduced by tight matching cuts. Second, tracks in both minimum-bias and $e\mu$ events are relatively isolated. One does not expect large differences in f_μ due to this source. The isolation of $e\mu$ events can be studied in the muon border tower energy distribution, which is defined as the energy in the calorimeter towers surrounding the tower that the muon passes. In figure 4.6

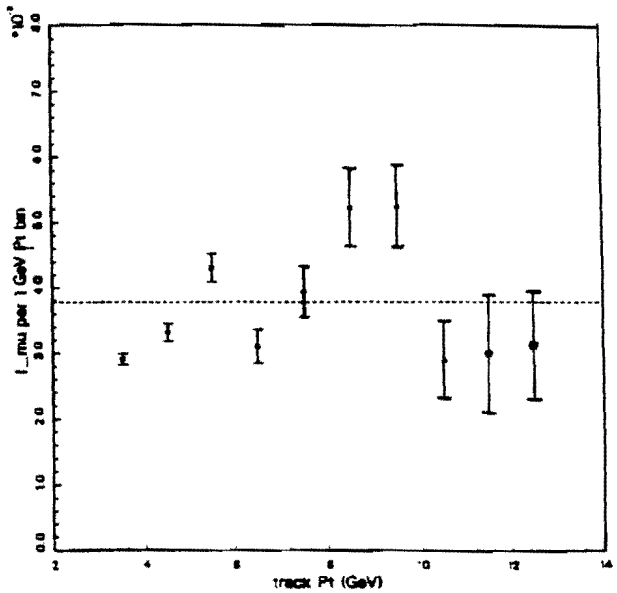

Figure 4.4: P_T dependence of the muons per track rate f_μ for non-interacting punchthrough particles.

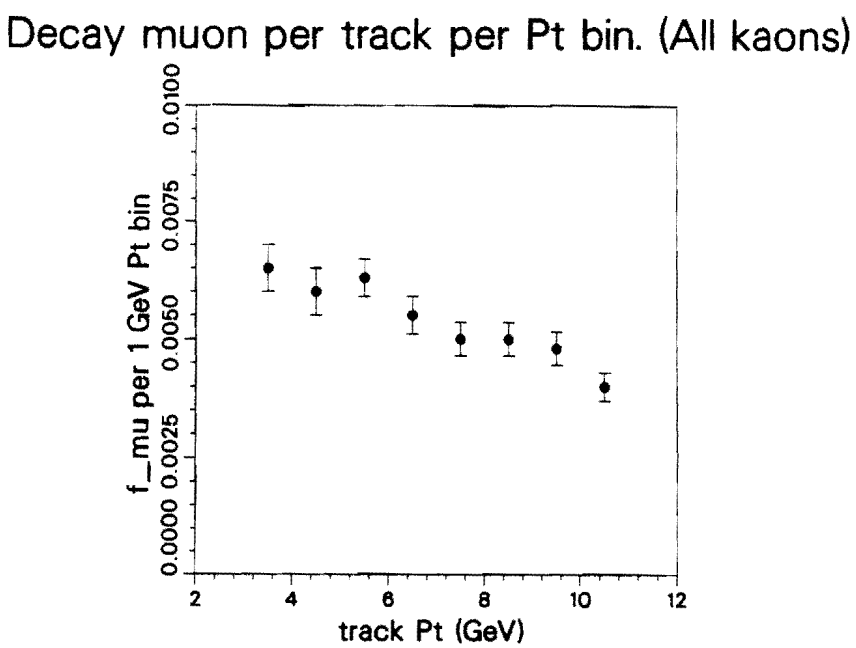

Figure 4.5: P_T dependence of the muons per track rate f_μ for decay muons.

and 4.7 we show this isolation quantity for both $e\mu$ events and minimum-bias events with a muon ($P_T \geq 2.0$ GeV). One can see that the difference is small even though the minimum-bias events are limited by statistics. A typical $e\mu$ event is shown in figure 4.8. The difference in f_μ due to possible differences in hadron activity around the muon candidate is negligible compared to to the large uncertainties from the limited statistics and other systematic sources discussed above.

Another important result from the isolation study is that the charge confusion in $e\mu$ events is a very small effect. In a mixing measurement, the charge sign is a crucial variable. Wrong charge sign can be assigned to tracks that are not well measured. This potential error is limited to negligible level ($\leq 1\%$) by requiring a high quality 3D track in the CTC for both the electron and the muon. While for electrons we require one and only one track be pointing to the EM cluster cell, so no mis-assignment can occur, the muons do not have this requirement. Possible muon stub to track mis-assignment can occur. This is another potential charge confusion. At offline reconstruction, muon candidate is attached to a CTC track by requiring the best match. If the muon stub is caused by a high P_T object while there are many relatively low P_T tracks nearby, a wrong matching can occur. This can lead to wrong charge assignment. Since the muons in $e\mu$ events are well isolated, such mis-assignment error is very small. The wrong charge $e\mu$ pair should contribute equally to both LS and OS events, same as the fake background.

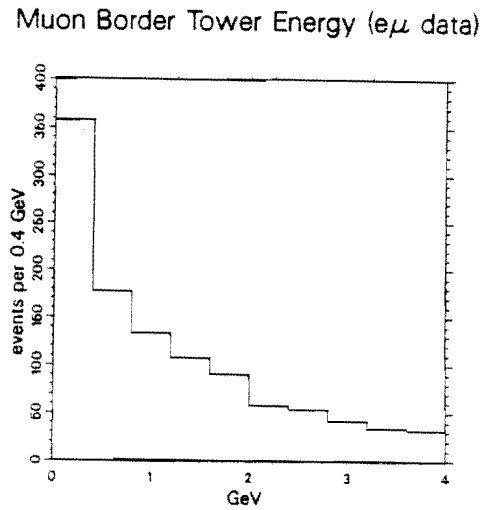

Figure 4.6: Muon border tower energy spectrum for $e\mu$ events.

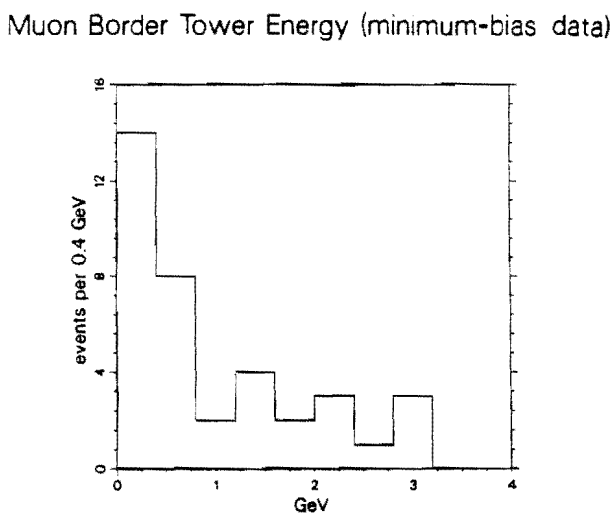

Figure 4.7: Muon border tower energy spectrum for minimum-bias muon events.

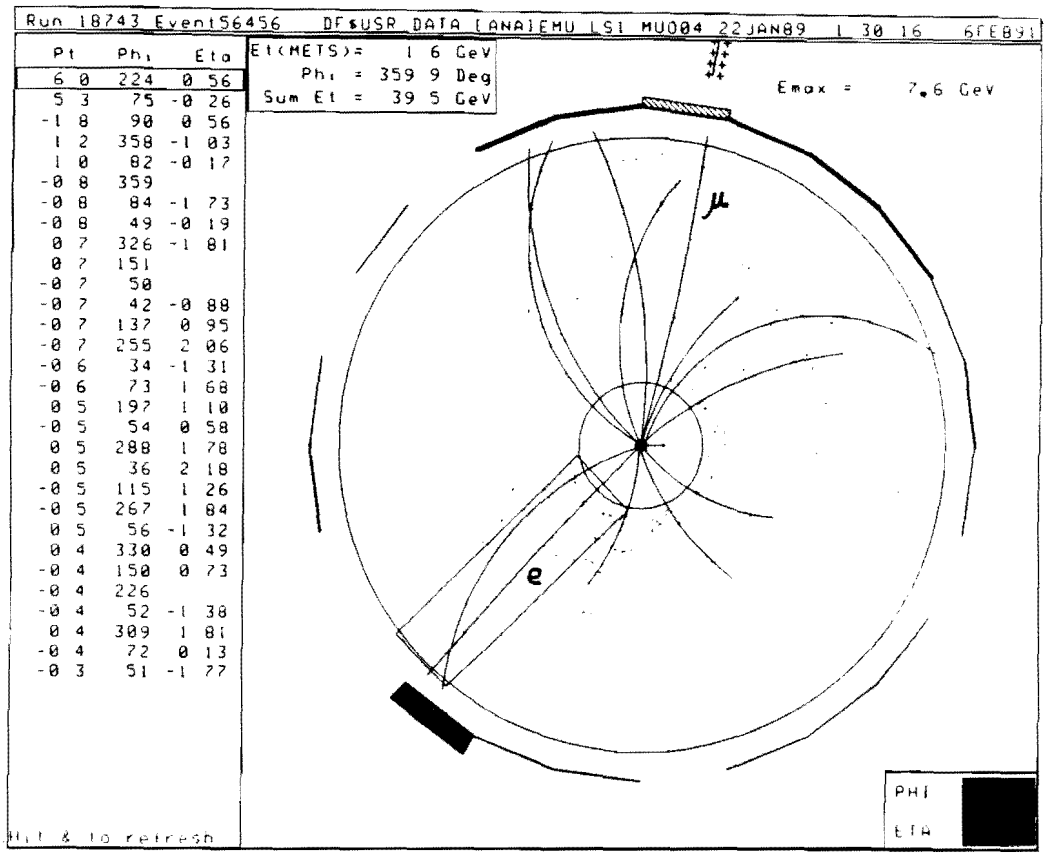

Figure 4.8: A typical $e\mu$ event (like-sign).

Table 4.2: Uncertainties for the muon per track rate f_μ.

source	uncertainty
statistics	35%
K/π ratio	15%
P_T dependence	20%
overall	50%

In summary, the muons per track rate f_μ is determined as

$$f_\mu = (0.27 \pm 0.12)\%$$

The main uncertainties are shown in table 4.2. Clearly this number is limited by statistics. By increasing the statistics of the minimum-bias high P_T tracks, both the statistical error and the error due to the P_T distribution can be reduced. The error due to K/π ratio difference can be eliminated if one measures the ratio in both the minimum-bias and the inclusive electron sample.

4.3 Background Fraction

To determine the background fraction, we first calculate the number of muons expected in the an inclusive electron sample using f_μ given in the last section. The ratio of this number to the number of $e\mu$ events actually observed in the same sample

gives an estimate of the background fraction.

For this purpose, one would like to have an inclusive electron sample with the same trigger criteria for the electron as in the $e\mu$ data. The $e\mu$ trigger threshold for the electron was 5 GeV. The inclusive electron sample with the closest threshold is the 7 GeV trigger sample (E7). This introduces another source of uncertainty since the background fraction may depend on the electron E_T. We check this using the 12 GeV threshold trigger (E12) inclusive electron sample. Since the E7 trigger was prescaled and only cover part of the run, the integrated luminosity is only about 110 nb^{-1}. The E12 trigger covered most of the run with a total luminosity of $4.1 pb^{-1}$. The event overlap between these two triggers is very small, less than 5%. Both samples used have about 10,000 good electron candidates. Thus they provide a good source for studying the electron E_T dependence of the background fraction. Ideally, one would like to have a large 5 GeV inclusive electron sample to study the background.

We apply the sample selection criteria to the inclusive electrons. Meanwhile, in the identified electrons, we look for muons and good tracks as defined before. For each of the two inclusive electron samples, we obtain the number of good tracks and multiply that by f_μ to get the expected background event number. The ratio of expected number of $e\mu$ background events to that of the actually observed $e\mu$ events is given in table 4.3. To check the dependence on the $e\mu$ invariant mass cut, both cases have been included. The cut here corresponds to the e-track invariant

Table 4.3: $e\mu$ background fraction from inclusive electrons.

	E_T^e	# tracks	# fake $e\mu$ expected	# $e\mu$ observed	background
without $e\mu$	7	1935	5.2 ± 2.3	27	$(19 \pm 9)\%$
mass cut	12	4082	11.0 ± 4.9	53	$(21 \pm 9)\%$
with $e\mu$	7	1324	3.6 ± 1.6	19	$(19 \pm 9)\%$
mass cut	12	2897	7.8 ± 3.5	44	$(18 \pm 8)\%$

mass. The number of $e\mu$ events per inclusive electron changes by almost a factor of 2 from E7 to E12 sample. This can be understood as the high threshold on the electron result in a high recoil P_T for the muons on the other side to pass the 3 GeV P_T requirement. Similar arguments apply for the tracks that can fake muons. The background fraction is unchanged within the uncertainty propagated from f_μ. We therefore use the background fraction from the E7 trigger for our final $e\mu$ sample. Including all error sources, we obtain the background fraction in our final $e\mu$ sample as

$$f_{BK} = (19 \pm 9)\%$$

Another indication of the background level is the muon charge asymmetry. The charge asymmetry in punch-through background can be as large as 3 for the K/π ratio discussed above. The final $e\mu$ sample contains 900 events with 181 $e^+\mu^+$, 165

$e^-\mu^-$, 290 $e^+\mu^-$ and 264 $e^-\mu^+$. The excess of positive muons is 42. Assuming a charge asymmetry of 1.5 for the non-interacting punch-through muons and the rest of background doesn't have charge asymmetry, and assuming that half of the background is non-interacting punch-through, the background muon charge asymmetry is calculated as:

$$y = \frac{\frac{1}{2} + \frac{1}{2}\kappa/(1+\kappa)}{\frac{1}{2} + \frac{1}{2}1/(1+\kappa)}$$

for $\kappa = 1.5$, one has $y = 1.28$. The expected background is given by

$$N_{BK} = \frac{42}{y-1} = 150$$

So the background fraction is $150/900 = 16.7\%$, consistent with above estimation. This kind of estimation depends strongly on the Monte Carlo modeling of the muon background so that it has a large systematic uncertainty. We therefore merely use it as a consistency check. More checks are given later.

4.4 Limit on Over-estimate

As discussed in section 4.1, this method of background estimation has the potential of over-estimating the background. The over-estimate arises from the fact that the tracks in the real electron subsample times the real muon per track rate corresponds to the number of real e and real μ events and was included in the background calculation. While the real muon per track rate is expected to be much higher in the

real e subsample compare to that in the the minimum-bias sample, the latter is not zero given the large B production cross-section and large semileptonic branching ratios. To show that the over-estimate is small, one needs to show that the real muon fraction in an unbiased 3 GeV muon sample is small. To get an estimate of the background in an low P_T (3 GeV) inclusive muon sample, we study the CTC/CMU matching χ^2 distribution. This distribution provides information about muons that have large multiple scattering or background with large mis-matching. Hadron leakage and decay-in-flight background usually exhibit such behavior. If one can gain some idea about part of background, e. g. using another sample, such as the J/Ψ, one can estimate the total background level. This is because all muon backgrounds are proportional to the number of good tracks in the data sample. If we assume that leakage and decay muons have the χ^2 distribution $F_{bk}(\chi^2)$, the ratio of events with $\chi^2 > \chi_c^2$ ($N_>$) to that of $\chi^2 < \chi_c^2$ ($N_<$) shall be a constant for pure background. In other words, if $N_>$ does not contain real muons, all background is proportional to $N_>$. That is $N_{BK} = cN_>$ with c as a constant independent of the data sample. (The constant c is determined by the background χ^2 shape and the cut χ_c^2.) Therefore, the background fraction f_{BK} will be given by

$$f_{BK} = c\frac{N_>}{N_T}$$

where only the constant c is unknown in the right side of the equation. By comparing two data samples, one can estimate the background fraction in one sample from that of the other. The cut χ_c^2 is designed to separate pure background from real muons. Due to multiple scattering, some real muons also have large χ^2. This contribution is studied using J/Ψ muons and is found to be relatively small.

Three samples of muon candidates from minimum-bias, J/Ψ and $e\mu$ events are used. The CTC/CMU matching χ^2 distributions are given in figure 4.9 to figure 4.11 The J/Ψ sample is selected requiring events with a dimuon trigger and $P_T \geq 3$ GeV for both muons. All muons are required to pass the muon selection cuts defined in section 4 except the χ^2 cut. It's clear that all of the 3 samples have a flat contribution in χ^2 up to values as large as 200. This is mainly because the backgrounds from hadron leakage or decay-in-flight usually have very soft P_T compared to the original track and get scattered much more than a prompt muon. The mis-matching in both position and momentum can cause a large χ^2. In table 4.4, we provide the total number of events and the events with $\chi^2 \geq 15$. Events with large χ^2 are primarily background. Some real muons have large multiple scattering can show up in this region as well, but it is small enough that the above discussion is valid. We take the ratio of the two numbers of events ($N_<$ and $N_>$) to determine the *relative* background level, as in column 4 of table 4.4.

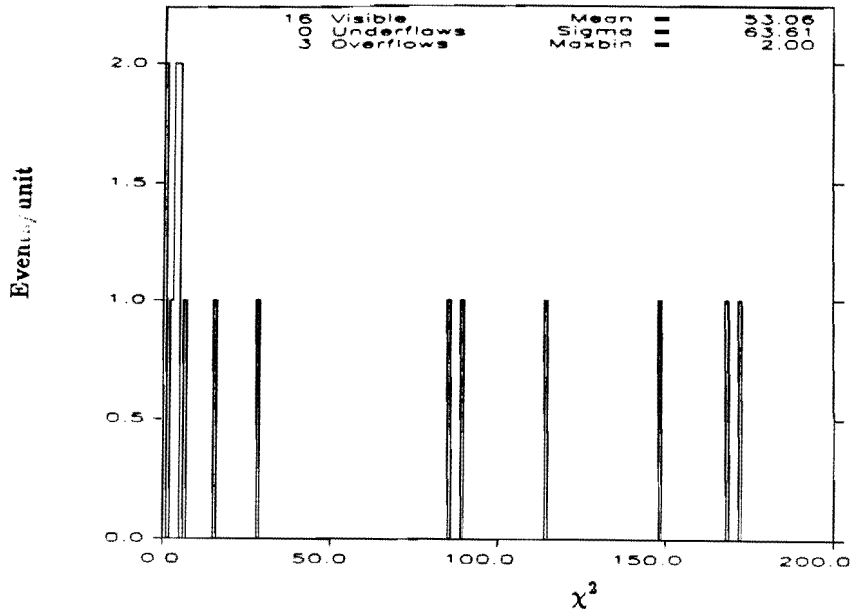

Figure 4.9: χ^2 distribution for minimum-bias muons.

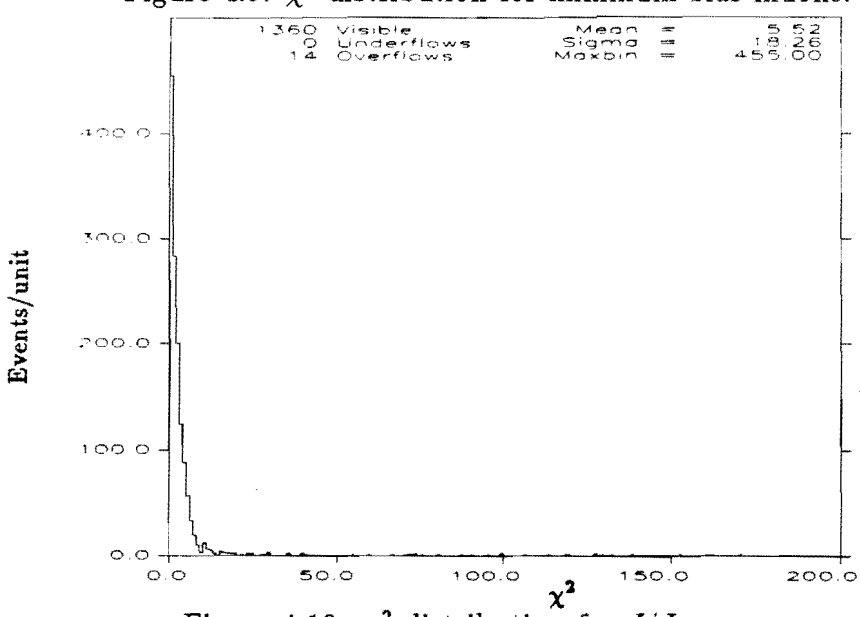

Figure 4.10: χ^2 distribution for J/Ψ muons.

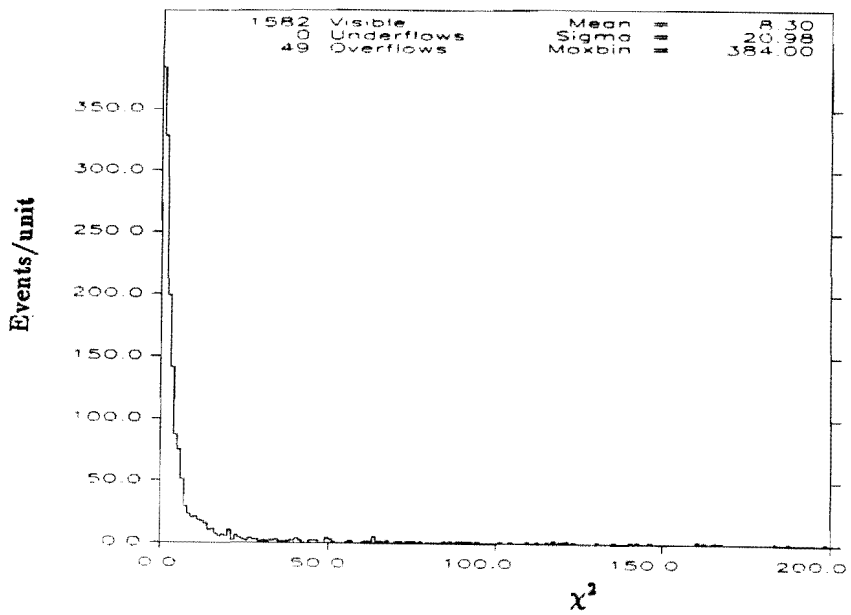

Figure 4.11: χ^2 distribution for $e\mu$ muons.

Table 4.4: Relative background level in minimum-bias, J/Ψ and $e\mu$ events.

sample	total events	$15 \leq \chi^2 \leq 200$	relative background level
J/Ψ	1347	63	4.7%
$e\mu$	1504	164	10.9%
MBS	17	9	52.9%

The J/Ψ sample has the lowest background while the inclusive muons from minimum bias has the highest. Take the fake muon rate in the J/Ψ sample to be $(8-10)\%$, as from the sideband study. From the relative background level one expects $(16-20)\%$ background in the $e\mu$ sample and $(80-100)\%$ background in the minimum-bias muons. Using the prompt e fraction determined in the inclusive electron analysis [28] of 65%, a 20% real muon rate only indicates that about 12% of the estimated background could be over-estimate. That is, over-estimate could effect only $\leq 2.5\%$ of the final data sample. From this one can also estimate that the fake e real μ fraction accounts only a small fraction of the background. The main background is due to events with a fake muon in it. This observation is consistent with the dielectron mixing analysis [29], where the fake background is determined to be small.

4.5 Background from J/Ψ Decays

Aside from the fake $e\mu$ background that is not associated with $b\bar{b}$ decays, there are real $e\mu$ events from some of the heavy flavor decay chains. Such events are not included in the above estimation and they are not signals for B mixing study. Given the large J/Ψ sample seen at CDF, it is natural to worry about the potential background from B to J/Ψ and J/Ψ to dilepton decays with one lepton lost due to the detector acceptance or selection cuts. The other B in the event decays semileptonicaly and results in a lepton common to the mixing signals (when both B's decay semileptonicly.) Here we

describe in detail a simple Monte Carlo that is also used in several other B physics analyses at CDF. [32] [33] The results from this study may also be useful for other B physics studies.

We first define the processes and the quantity to be studied.

a) Background process:

$b \rightarrow e\,X$

and

$b \rightarrow J/\Psi\,X$ with $J/\Psi \rightarrow \mu^+\mu^-$

b) Signal process: (both semileptonic decays)

$b \rightarrow e\,X$

and

$b \rightarrow \mu\,X$ or $b \rightarrow c\,X$ with $c \rightarrow \mu\,X$

Process a) with only one muon of the dimuon seen in the final state gives an $e\mu$ event, which is a typical background with equal contribution to both like-sign and opposite-sign signal. Process b) gives the signal that is used to extract the mixing parameter. The ratio of the number of events from these two processes in a given data set is the quantity to be studied. This is just the fraction of background due to process a). The following kinematic cuts are applied in the following simple Monte Carlo study.

electron $\quad E_T \geq 5$ GeV $\quad |\eta| < 1.00$

muon $\quad P_T \geq 3$ GeV $\quad |\eta| < 0.65$

The similar process where J/Ψ decays to dielectrons is less important because of these cuts.

We define the background fraction from the process a) as

$$f_{J/\Psi} = \frac{N_a}{N_b}$$

where N_a is the number of events come from process a) and N_b is from process b) given the same number of events $b\bar{b}$ parent events, N_t. Hence,

$$N_a = N_t \, \mathrm{Br}(b \to e\, X) \, \mathrm{Br}(b \to J/\Psi\, X) \, \mathrm{Br}(J/\Psi \to \mu^+\mu^-) \bullet Q_a$$

$$N_b = N_t \, \mathrm{Br}(b \to e\, X)(\mathrm{Br}(b \to \mu\, X) + \mathrm{Br}(b \to c \to \mu\, X)) \bullet Q_b$$

where Q_a and Q_b are the reduction factors due to detector acceptance and P_T cut. The background fraction $f_{J/\Psi}$ becomes

$$f_{J/\Psi} = \frac{\mathrm{Br}(b \to J/\Psi\, X) \, \mathrm{Br}(J/\Psi \to \mu^+\mu^-)}{(\mathrm{Br}(b \to \mu\, X) + \mathrm{Br}(b \to c \to \mu\, X))} \bullet \frac{Q_a}{Q_b}$$

using [39]

$$\mathrm{Br}(b \rightarrow J/\Psi\, X) \simeq 1\%$$

$$\mathrm{Br}(J/\Psi \rightarrow \mu^+\mu^-) \simeq 7\%$$

$$\mathrm{Br}(b \rightarrow \mu\, X) \simeq 10\%$$

$$\mathrm{Br}(b \rightarrow c \rightarrow \mu\, X) \simeq 10\%$$

the branching ratio part is readily calculated. The fraction reduces to

$$f_{J/\Psi} = 0.35\% \bullet \frac{Q_a}{Q_b}$$

The ratio of the acceptance factors is determined from the following Monte Carlo.

First, we generate b quarks according to the Nason-Dawson-Ellis (NDE) [34] P_T distribution, as shown in figure 4.12. Then the b quark is fragmented into a B meson using the Peterson formalism as in ISAJET [35], figure 4.13. (See section 5.2 for discussion of heavy quark fragmentation.) In the B meson rest frame, we use CLEO's measurements for the inclusive J/Ψ and lepton momentum spectra to generate J/Ψ and muon final state momentum. The CLEO measurements [30, 31] used are given in figure 4.14 and 4.15. A Lorentz boost is then applied to the generated daughter particles into the CDF lab frame. In the case of J/Ψ, the next step is to decay it to dimuons. Since we are interested in the inclusive spectrum, the helicity polarization is taken as flat. Note, the CLEO inclusive lepton spectrum includes direct B decays ($b \rightarrow \mu\, X$) as well as sequential decays ($b \rightarrow c \rightarrow \mu\, X$). The relative contribution is almost equal without any cuts, as suggested by the equal branching ratios.

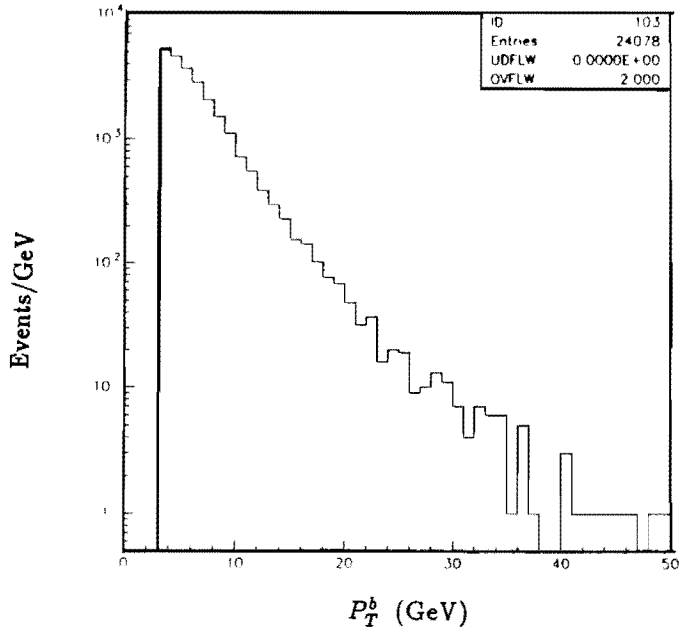

Figure 4.12: P_T spectrum of b quarks from next to leading order QCD calculations.

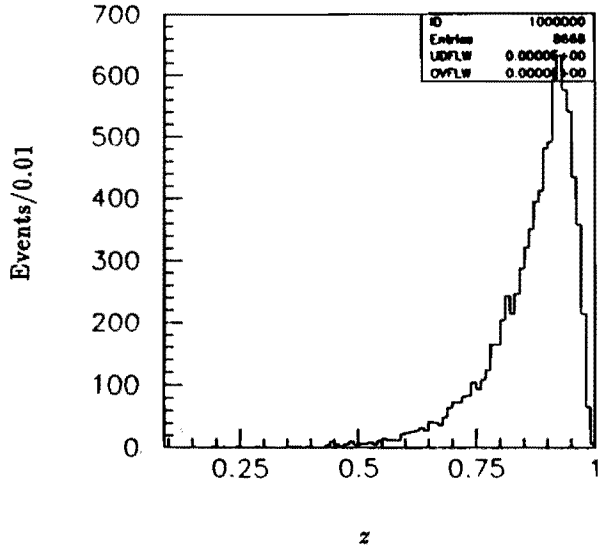

Figure 4.13: Peterson fragmentation function.

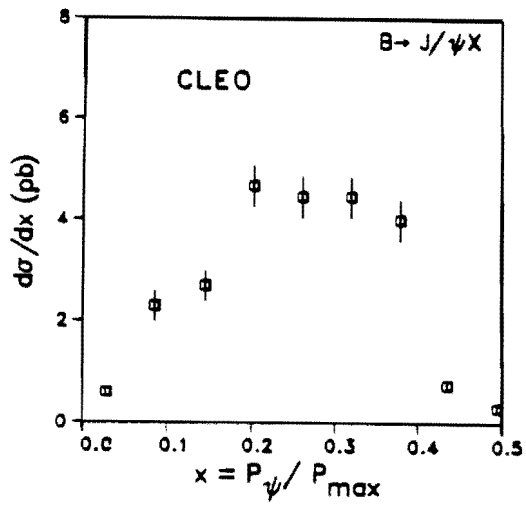

Figure 4.14: Momentum spectrum for J/Ψ's from B meson decay at rest (CLEO).

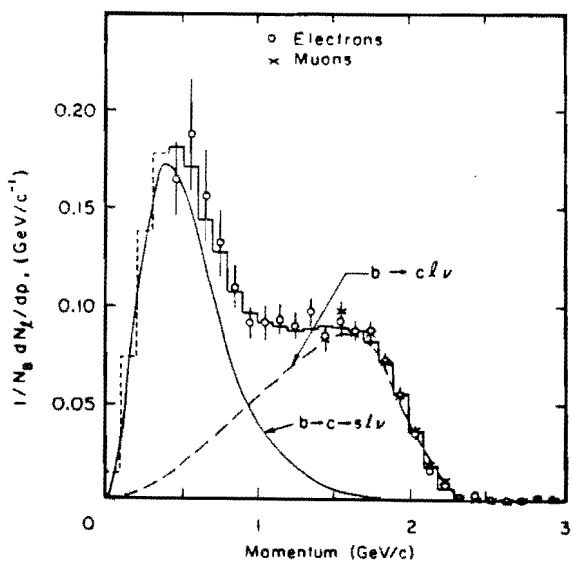

Figure 4.15: Momentum spectrum for inclusive leptons from B meson decay in the B meson rest frame (CLEO).

Table 4.5: Relative efficiency for muons from B to J/Ψ and semiletonic decays.

$b \rightarrow J/\Psi \rightarrow \mu^+\mu^-$ with only one muon detected	8751
with both muon detected	296
inclusive muons the muon detected	8668

The generated muons are then propagated through a model of the CDF detector to determine whether they enter the muon chambers using the CDF geometry for the 1988-89 run. In figure 4.16 and 4.17 we show the P_T spectra of the muons in the muon detector fiducial volume.

With 50,000 b quarks generated for both process a) and b), where no branching ratios are involved, the result from the Monte Carlo is listed in table 4.5.

Therefore, the acceptance ratio Q_a/Q_b is given by

$$\frac{Q_a}{Q_b} = \frac{8751}{8668} = 1.01$$

The background fraction is obtained as

$$f_{J/\Psi} = 0.35\% \bullet 1.01 = 0.35\%$$

In conclusion, this background source is negligible compare to the already large uncertainty (10%) in the background determination.

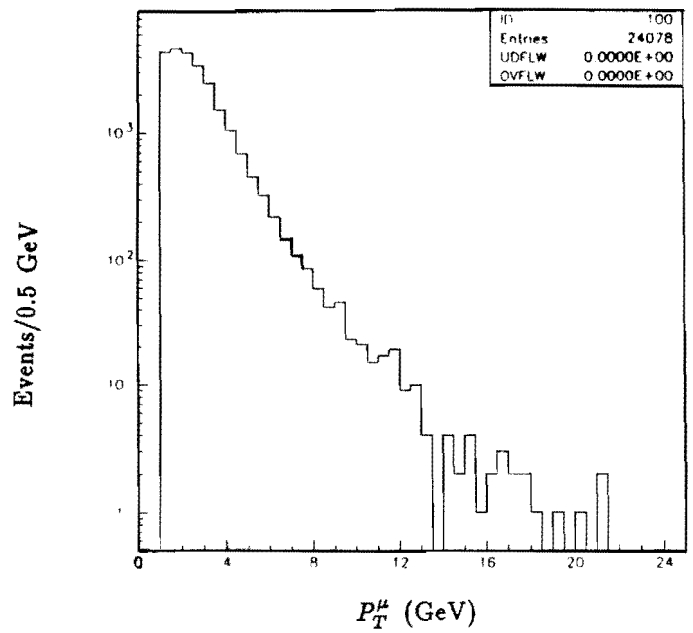

Figure 4.16: Muon P_T from $b \rightarrow J/\Psi \rightarrow \mu^+\mu^-$ decays. Only one muon has been accepted by the detector geometry and only such muons have been plotted.

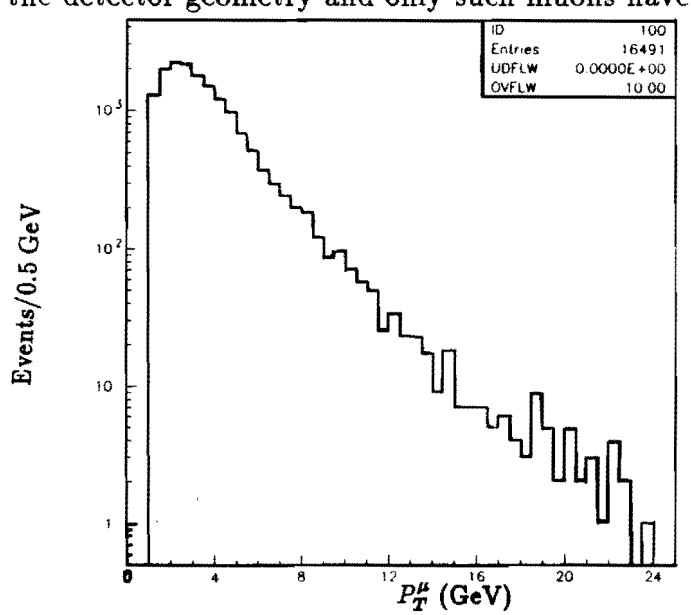

Figure 4.17: Muon P_T from inclusive B semileptonic decays, including sequential decays. CDF muon chamber geometry acceptance implied.

4.6 Background Subtraction

The number of events in the final $e\mu$ sample is 900. With the background fraction f_{BK} of $(19 \pm 9)\%$, we obtain the total number of background events as 171 ± 81. To do the background subtraction, one needs to know the contributions of background to both LS and OS events. Due to possible local charge correlation, the LS:OS ratio in the background is not necessary 1:1. For example, if a fake muon is on the same side of an electron, it will usually have a charge opposite to that of the electron due to charge correlation. However, if one demands that the electron and the fake muon be opposite in azimuth, the charge correlation will be small. This is because tracks with a large relative opening angle typically come from different partons. In such cases, one expects the LS:OS ratio close to unit. This is true for fake $e\mu$ background.

To determine the LS:OS ratio in the background, we again use the inclusive electron sample. Since fake muons arise from tracks satisfying the track selection cuts, random electron-track pair should represent the real e fake μ and fake e fake μ background sample. We thus expect the charge correlation in this sample to be similar to that of the $e\mu$ background. In the E7 sample, we find 637 LS and 655 OS e-track events after the invariant mass cut. So the LS/OS ratio is 0.95 ± 0.06, where the error is statistic only. This is consistent with 1:1. More importantly, it shows that the observed raw R $= 364/554 = 0.62$ is inconsistent with pure background.

With this observation, we attribute half (86 ± 41) of the background to both LS

and OS $e\mu$ events. After subtracting the background, the charge ratio R is

$$R = 261/469 = 0.556 \pm 0.048 \text{ (stat)} \, ^{+0.035}_{-0.042} \text{ (sys)}$$

This ratio contains the experimental information on $B^0\overline{B}^0$ mixing. To determine the mixing parameter from R, we need to study the Monte Carlo predictions for unmixed B decays. This is the subject of the next chapter.

Chapter 5

Monte Carlo Modeling of Unmixed B Decays

In the last two chapters, we obtained a charge ratio R which indicates the charge asymmetry in the real $e\mu$ events from $b\bar{b}$ and $c\bar{c}$ decays. The mixing signal is embedded in this ratio. However, asymmetry is expected even without mixing. Dilepton events from unmixed B decays have to be understood before one can determine the mixing probability. Using Monte Carlo studies, one can study the main sources of such events and determine their charge asymmetries.

Dileptons mainly come from the following processes:

1.) two first generation semileptonic decays of a $b\bar{b}$ event

$$b \rightarrow l^- X$$

$$\bar{b} \rightarrow l^+ X$$

Only opposite-sign (OS) dileptons are produced in this process.

2.) one first generation, one second generation semileptonic decays of a $b\bar{b}$ event

$$b \rightarrow cX \rightarrow l^+ X$$

$\bar{b} \rightarrow l^+ X$

This process gives like-sign (LS) dileptons without mixing. This is the major process that can confuse the mixing signal.

3.) two semileptonic decays of a $c\bar{c}$ event

$c \rightarrow l^+ X$

$\bar{c} \rightarrow l^- X$

Only OS dileptons are expected from these decays.

There are other processes which also produce opposite-sign dileptons, but the contribution to the total rate is very small. For example, dileptons can come from

i.)

$b \rightarrow cX \rightarrow l^+ X$

$\bar{b} \rightarrow \bar{c}X \rightarrow l^- X$

ii.)

$b \rightarrow \tau^- X \rightarrow l^- X$

$\bar{b} \rightarrow \tau^+ X \rightarrow l^+ X$

The first process is studied separately to have a very small fraction. The second process is included in the event generation. The double sequential decay nature generally makes its acceptance very low due to the lepton P_T cut.

In the absence of mixing, the charge ratio R_0 is given by

$$R_0 = \frac{N_s}{N_f + N_c} = \frac{f_s}{1 + f_c}$$

where N_f, which is dominated by process 1, includes all OS dileptons from $b\bar{b}$ decays, N_s is number of events from process 2 and N_c is number of events from process 3, $f_s \equiv \frac{N_s}{N_f}$, $f_c \equiv \frac{N_c}{N_f}$.

If $B^0\overline{B}^0$ mixing occurs, dileptons from $b\bar{b}$ decays will change their charge sign. Since B hadrons are not separately identified, one defines the probability of a B hadron transforming into its antiparticle as the mixing parameter. This is therefore the probability of $B^0\overline{B}^0$ mixing averaged over all B hadron species produced in $p\bar{p}$ collisions. The relationship between R and χ is

$$R = \frac{2\chi(1-\chi)N_f + [(1-\chi)^2 + \chi^2]N_s}{[(1-\chi)^2 + \chi^2]N_f + 2\chi(1-\chi)N_s + N_c} = \frac{2\chi(1-\chi) + [(1-\chi)^2 + \chi^2]f_s}{[(1-\chi)^2 + \chi^2] + 2\chi(1-\chi)f_s + f_c}$$

The ratio R is larger than R_0 if mixing exists.

To determine the mixing parameter χ from the observed R, a Monte Carlo study is used to determine the two ratios f_s and f_c. In this chapter, we first discuss the various $b\bar{b}$ and $c\bar{c}$ production and semileptonic decay processes. Then, we give the results from our Monte Carlo data including the full detector simulation.

The ISAJET Monte Carlo generator package is used for this analysis. Other Monte Carlo generators exist, but most of them do not have a complete fragmentation and decay structure and do not provide underlying event generation. ISAJET has been incorporated into the CDF detector simulation package. Most aspects of this generator have been studied in other analyses and have been tuned to agree with the

available experimental data. The heavy quark sector has been studied in several other analyses, most notably, the top quark searches and the b cross-section measurements at both CERN $p\bar{p}$ collider experiments and CDF.

B physics is among the most complicated sectors for Monte Carlo generators. Its production, fragmentation and decay all involve complicated QCD calculations, theoretical assumptions and unknown parameters. In the following, we first study the production mechanism.

5.1 Heavy Quark Production

Heavy quarks (c, b or t) can be produced via a gluon or quark fusion mechanism in lowest order QCD, as shown in the Feynman diagrams in figure 5.1. At collider energies, the gluon fusion processes dominates. Normally, one will think the lowest order process should be the major contribution to the total production cross-section. In the case of b or c quark production, this is actually not the case. The next to leading order diagrams yields almost twice as large a contribution. Since the strong production process conserves flavor quantum numbers, the $b\bar{b}$ are always produced in pairs. So the lowest order production mechanism is an α_s^2 process, where α_s is the strong coupling constant. The next to leading order, which we call higher order in subsequent discussions, is α_s^3. The higher order diagrams are shown in figure 5.2. Because of the different event structure for the final state heavy quark, they are

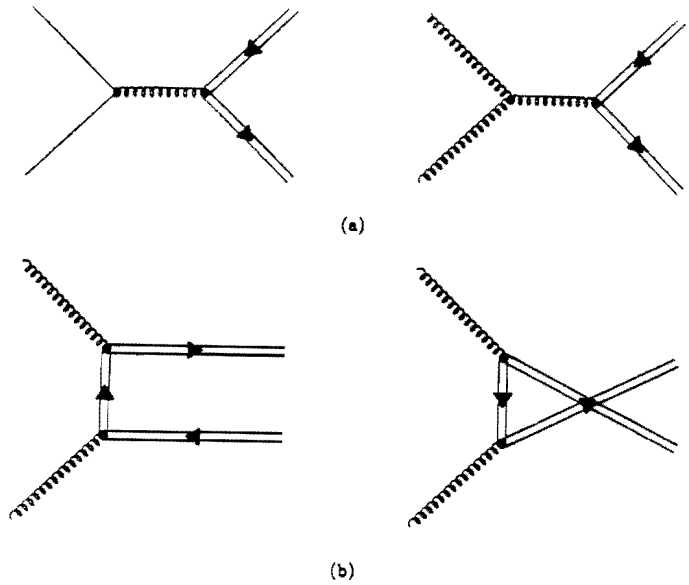

Figure 5.1: Feynman diagrams for Lowest Order $b\bar{b}$ production.

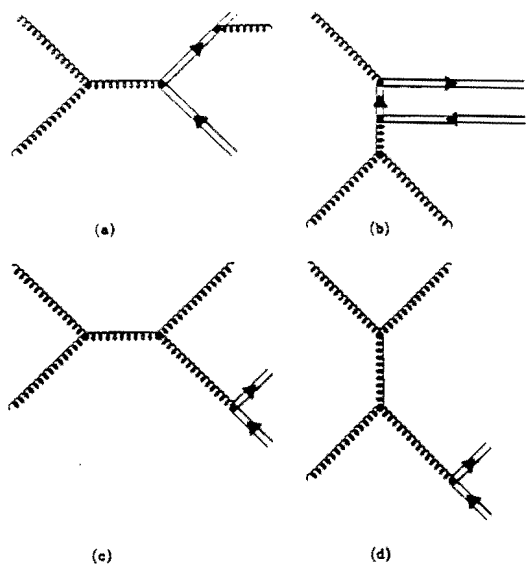

Figure 5.2: Feynman diagrams for Next Leading Order $b\bar{b}$ production.

usually referred to as two processes: 1.) gluon splitting or $g \rightarrow b\bar{b}$, where the $b\bar{b}$ come from a decay of a final state gluon; 2.) flavor excitation or $gb \rightarrow gb$, where the initial state gluon splits into $b\bar{b}$ and one of the b quarks gets scattered by another parton from the incident proton. The gluon splitting events usually have two B hadrons both with high P_T, so their decay leptons can both be observed. For the flavor excitation process, usually only one of the B hadrons in the final state has high P_T to pass the trigger requirements. In high P_T dilepton events, this process is therefore suppressed relative to the gluon splitting process.

The reason why higher order processes are as important as the lowest order one is due to the large gluon-gluon scattering cross-section. The process $gg \rightarrow gg$ has a cross-section about 100 times that of $gg \rightarrow b\bar{b}$, even through the $g \rightarrow b\bar{b}$ branching fraction is only 1%, the $b\bar{b}$ production from this process is competitively as large as the lowest order contribution. In view of the importance of the higher order processes in the following Monte Carlo study, we generate both lowest order and higher order $b\bar{b}$ events.

For the mixing measurement, the requirement of two B hadron in the final state is crucial. The requirement of two high P_T leptons and the invariant mass cut are found to suppress the higher order processes. This clearly reduces the acceptance, but also makes the analysis relatively insensitive to the higher order processes. The input we need from Monte Carlo are two event number ratios. The ratios are less

sensitive to many systematic uncertainties, including the efficiencies, acceptance, etc.. Such observation makes the analysis less sensitive to Monte Carlo uncertainties.

There are some technical difficulties one has to overcome in generating a large sample of full $b\bar{b}$ and $c\bar{c}$ events. The generation process, especially for higher order production, is very CPU intensive. The difficulty in higher order generation is due to the very slow speed and low efficiency. ISAJET uses a gluon shower mechanism, i.e. gluon radiates gluon, to generate the higher order processes. Due to the small branching fraction for a gluon to split into $b\bar{b}$ (or $c\bar{c}$) pair, this process is very slow. If one looks for a dilepton pair from $b\bar{b}$ decays, each lepton has about 20% branching ratio, the dilepton branching fraction is reduced to about 4%. Taking into account the P_T requirement and fast falling P_T spectrum, the efficiency to observe dileptons is further reduced to about 10^{-4} per $b\bar{b}$ pair. Such a slow process takes an extremely large amount of computer CPU time (about 3 months) to generate a sufficient sample (5 pb^{-1}) even with the fast IBM3090 mainframe. Modifications to ISAJET have been made to speedup the $b\bar{b}$ and $c\bar{c}$ production and decay to dilepton processes. After the modifications, the generator is sped up by almost a factor of 20. In the following subsections, we study dilepton events from each of the production processes using about 4.5 pb^{-1} Monte Carlo data sample.

5.1.1 Direct $b\bar{b}$ Production

Direct $b\bar{b}$ refers to the events produced via lowest order Feynman diagrams. This is a typical source of high P_T, back to back $b\bar{b}$ events. Most of these events fragment to dijets. Some of them will give rise to two high P_T, almost back to back leptons. These dileptons usually have large pair mass. The cuts for $e\mu$ selection clearly favor this source of $b\bar{b}$ to dilepton signal. The $e\mu$ opening angle and invariant mass distributions for $b\bar{b}$ events generated in this process are given in figures 5.3 to 5.6. The isolated peak at low mass in the OS events is clearly due to the single B sequential decays. These events are removed completely by the invariant mass cut. The rest of the events all have distinctively large opening angle.

At the quark level, the $b\bar{b}$ P_T scatter distribution is shown in figure 5.7, which clearly shows a strong correlation between the two b quarks. Such correlations are important for understanding the charge asymmetries in the Monte Carlo. If the two B's are strongly correlated, one high P_T B will imply another B with high P_T, therefore the second B acceptance will be large. This correlation is different for lowest order and higher order production processes. More study on the second B tagging efficiency using leptons at CDF is discussed in chapter 8.

Another interesting quantity to study is the $b\bar{b}$ vector sum P_T distribution. For an exact $2 \rightarrow 2$ process, one expects a delta function at zero. However, ISAJET provides both initial state and final state gluon radiation. Such QCD processes boost

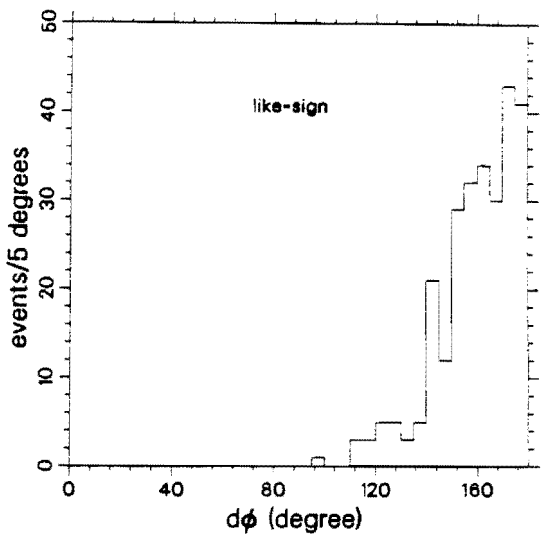

Figure 5.3: $e\mu$ opening angle for LS events from lowest order $b\bar{b}$ production.

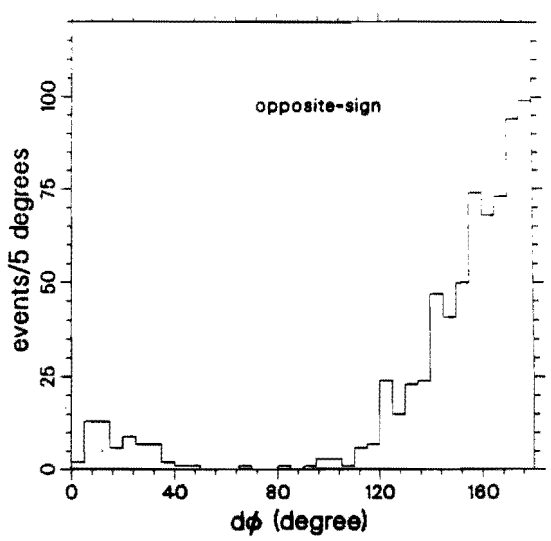

Figure 5.4: $e\mu$ opening angle for OS events from lowest order $b\bar{b}$ production.

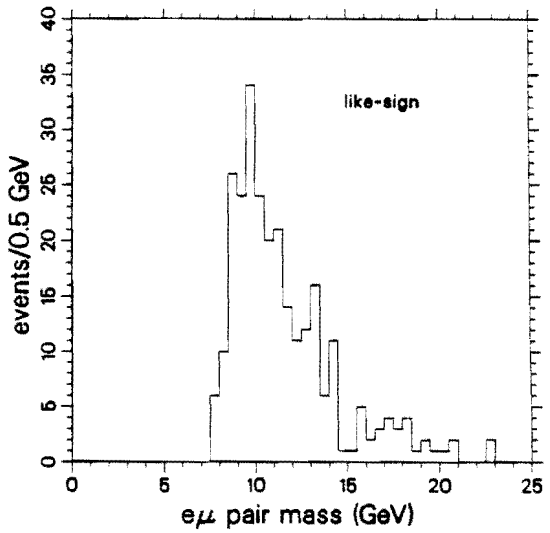

Figure 5.5: $e\mu$ pair mass for LS events from lowest order $b\bar{b}$ production.

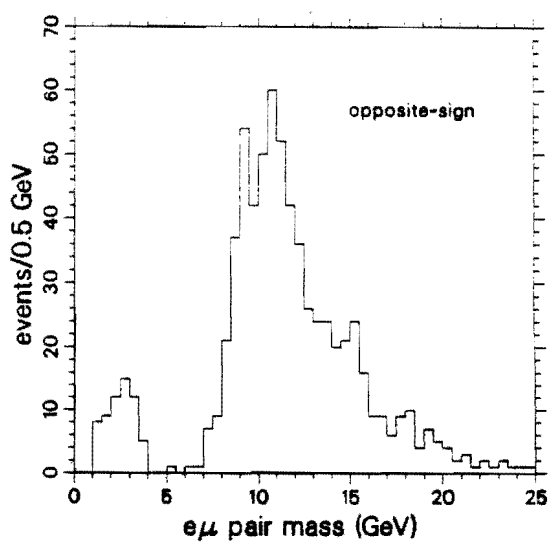

Figure 5.6: $e\mu$ pair mass for OS events from lowest order $b\bar{b}$ production.

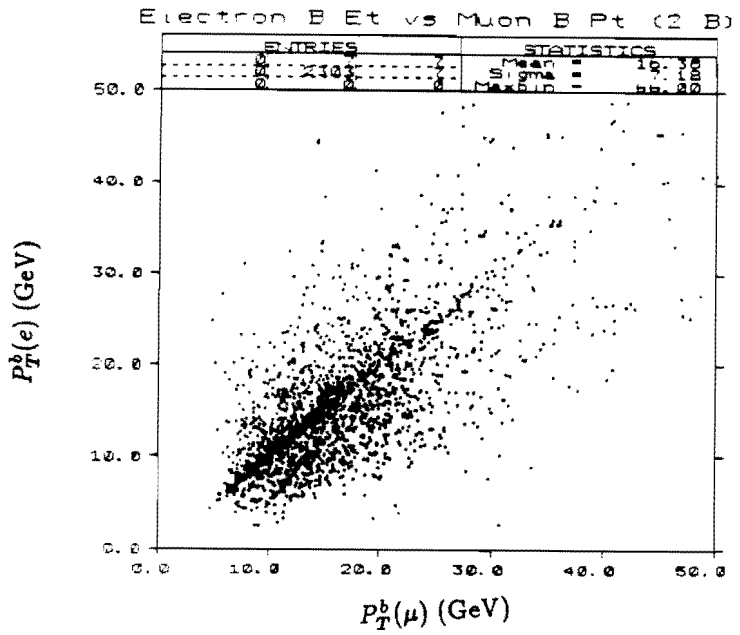

Figure 5.7: $b\bar{b}$ P_T correlation in Lowest Order $b\bar{b}$ production.

the $b\bar{b}$ pair with some P_T. These gluon radiations can be viewed as the soft tail of the higher order processes. In real situations, there is no absolute difference between lowest order and high order diagrams. When the radiated gluon momentum goes from zero to as high as the final state heavy quark, then the process goes from strict lowest order to higher order. The term lowest order and higher order is only valid in a P_T relative sense. There are also interference effects between different Feynman diagrams at intermediate energy. However, if one requires high P_T for both b quarks, the interference effect is small and one therefore can study the different processes separately.

The $e\mu$ vector sum P_T is the experimentally measurable representation of the $b\bar{b}$ vector sum P_T in this analysis. This quantity can be used to separate lowest order and

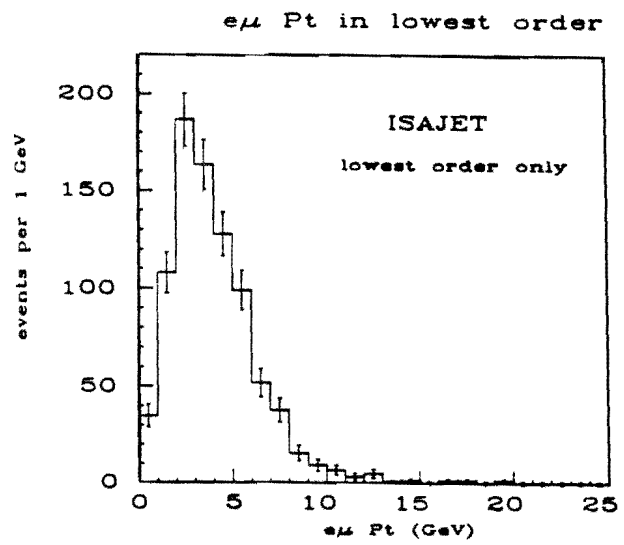

Figure 5.8: $e\mu$ vector sum P_T distribution from lowest order $b\bar{b}$ production.

higher order processes. More discussion is given in section 5.2.1. The Monte Carlo spectrum of $e\mu$ vector sum P_T for direct $b\bar{b}$ production is given in figure 5.8. The soft gluon radiation leads to a peak at low P_T. Comparisons between this spectrum and that for higher order processes will be made in following discussions. The result can be interpreted as a determination of the higher order fraction in the final $e\mu$ sample.

5.1.2 Gluon Splitting

As we'll see later, this is the most important higher order process for this analysis. The flavor excitation contribution is much more strongly suppressed by the P_T cuts. This is also the most slowly generated process in ISAJET. Since ISAJET does not generate $2 \rightarrow 3$ scattering directly, it uses a gluon shower mechanism to generate such processes. With the gluon shower mechanism, for each parton both in initial or final

state, gluon radiation is added to take into account the QCD effects. The drawback of using such an algorithm to produce gluon splitting is the cost in terms of CPU time. One has to generate many non-interesting events to get one B event. To reduce this inefficiency, modifications were made to ISAJET. This is the often referred to as the ISALEP algorithm.

In ISALEP, a standard TWOJET hard collision is performed. Then this event is evolved a number of times. Each evolution has multi-gluon radiations with each gluon having a certain probability of splitting into quark pairs. A search for a heavy quark in the event is done after each evolution. If heavy quarks are found, the program proceeds to fragment and decay the heavy quark. Otherwise, the program re-evolves the same hard collision. In the decay process, the same technique is used. Each heavy quark is given a number of chances to decay. A lepton search is performed after each decay tree is completed. Only events with a lepton passing certain P_T threshold are kept. To prevent statistical bias, every hard collision is evolved the same number of times as is the decay of every heavy quark. The numbers of evolutions and decays are set such that the same initial state does not produce more then one event. With each hard collisions evolved 10 times and each heavy quark event decayed 10 times, the program can be speeded up by a factor of 10.

For dilepton generation, there is another inefficiency. Given a single B semileptonic decay branching ratio of 10%, the dileptons only have an acceptance of 1%.

To ensure that almost each $b\bar{b}$ event will lead to a dilepton final state, further modifications have been made. These modifications restricts the possible decays to be those that will eventually lead to a final state lepton. This gives another factor of 10 speedup. However, in order to do this, events have to be separately generated according to whether a b or c quark decay produce the lepton. This reduces the overall speed by a factor of 2. Therefore, this additional speedup is a factor of 5 for dilepton events.

The gluon splitting process is generated using the ISALEP version of ISAJET. To avoid lowest order process, the outgoing hard collision partons are set to g, u, d, s. So heavy quarks can only come from gluon splitting. The event structure for this process is very different from the direct production. The $b\bar{b}$ pair, coming from a high P_T gluon, is more co-linear than back to back. The opening angle and invariant mass distribution for the decay $e\mu$ events are shown in figure 5.9 to 5.12 Here, the $e\mu$ pair mass cut removes almost half of the events. The quark level correlation is shown in figure 5.13. It's clear that the correlation is much smaller than in the case of direct production. The vector $b\bar{b}$ P_T here represents the parent gluon P_T, which is required kinematically to be larger than about $2m_b$. The corresponding $e\mu$ vector sum P_T is shown in figure 5.14. Comparing with figure 5.8, one can see that this spectrum peaks at a relatively high value. These spectra are used in determining the gluon splitting fraction in the $e\mu$ data. As shown in figure 5.15 [36], the b quark P_T spectra for

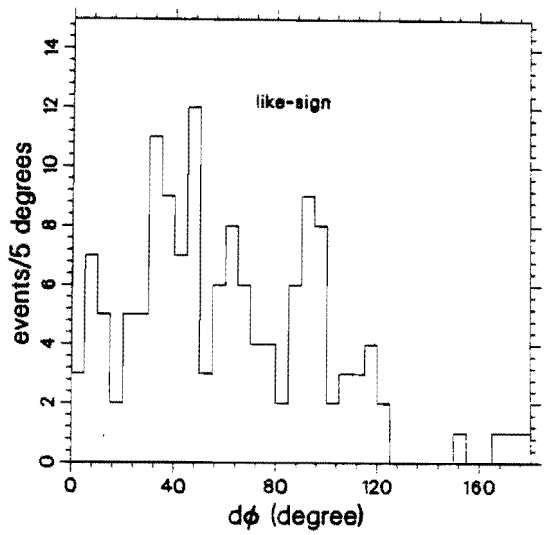

Figure 5.9: $e\mu$ opening angle for LS events from gluon splitting $b\bar{b}$ production.

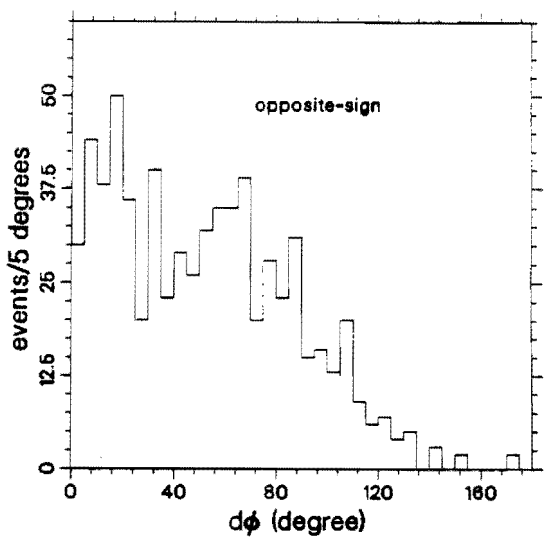

Figure 5.10: $e\mu$ opening angle for OS events from gluon splitting $b\bar{b}$ production.

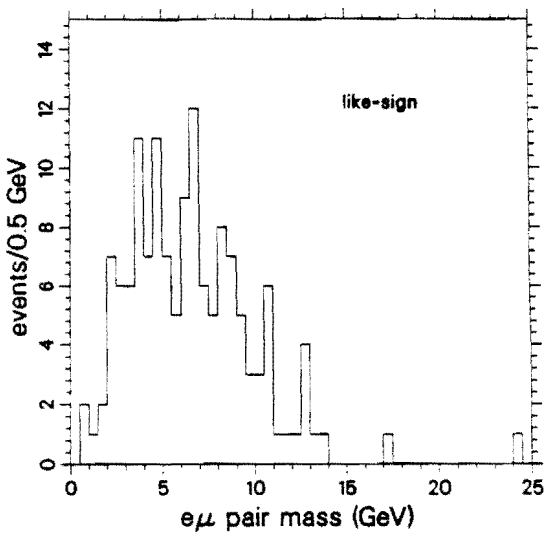

Figure 5.11: $e\mu$ pair mass for LS events from gluon splitting $b\bar{b}$ production.

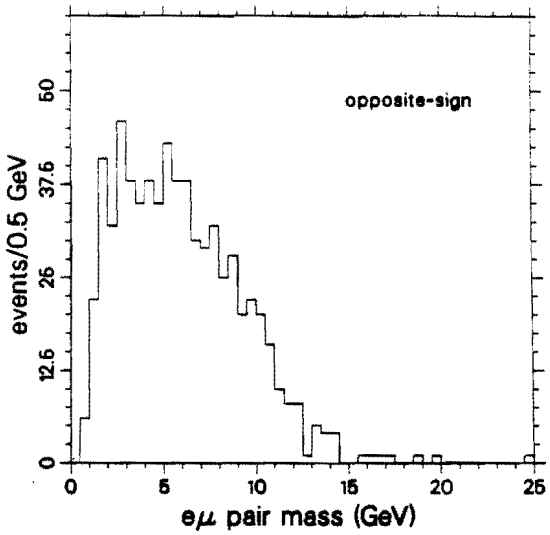

Figure 5.12: $e\mu$ pair mass for OS events from gluon splitting $b\bar{b}$ production.

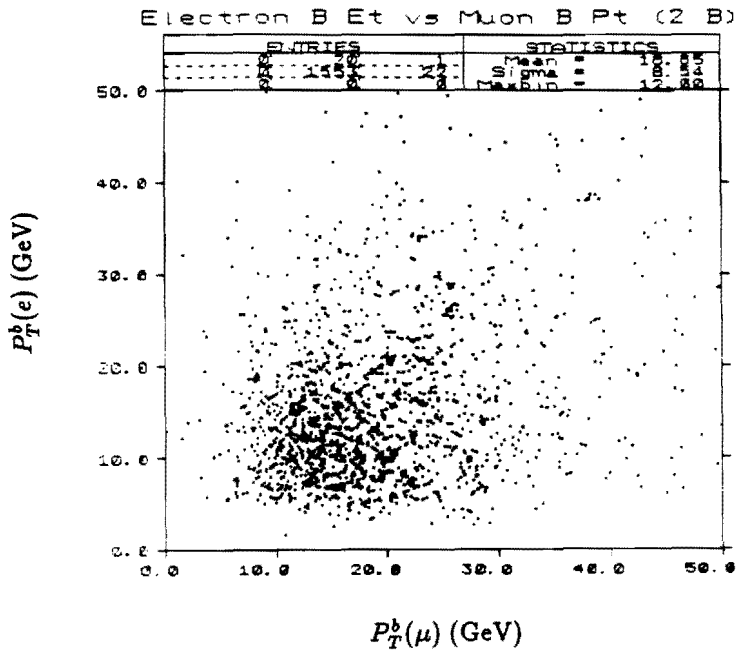

Figure 5.13: $b\bar{b}$ P_T correlation in gluon splitting $b\bar{b}$ production.

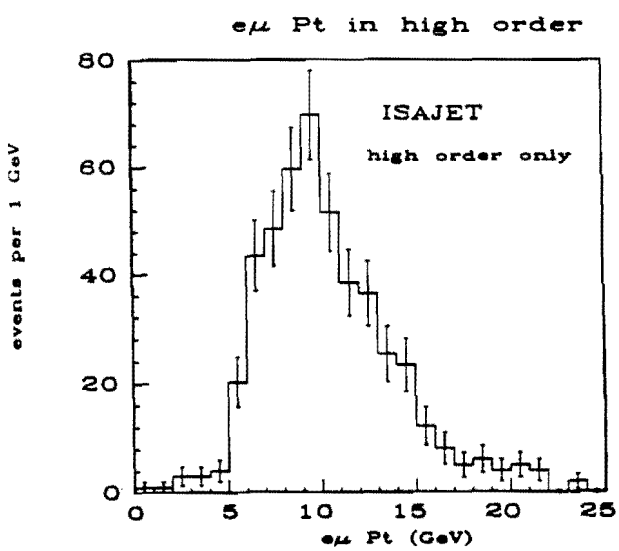

Figure 5.14: $e\mu$ vector sum P_T distribution from gluon splitting $b\bar{b}$ production.

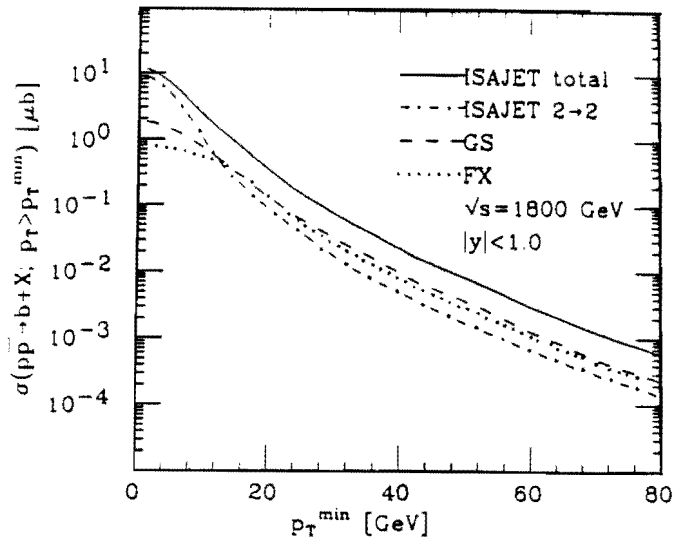

Figure 5.15: b quark P_T distribution from ISAJET.

the higher order $b\bar{b}$ is very close to the lowest order process. This establishes the so called K factor, which is the ratio of the total production cross-section including high order contribution to that from the lowest order calculation. It almost indicates that the P_T cut will not significantly suppress the higher order processes relative to the lowest order process. Such a conclusion is not completely true because of the lack of correlation between $b\bar{b}$ pairs produced in higher order. For the direct $b\bar{b}$ if one of them has high P_T, the second one will also have high P_T. In the case of gluon splitting, such correlation is absent. In requiring two high P_T leptons, the gluon splitting process is relatively suppressed.

5.1.3 Flavor excitation

In ISAJET, the lowest order process, gluon splitting and flavor excitation have almost the same total production cross-section [36]. However, after the dilepton P_T cuts and the invariant mass cut, the gluon splitting fraction is reduced to about 30% of the total rate. The flavor excitation contribution is suppressed even further.

Flavor excitation, by definition, involves an initial state gluon splitting. A gluon from incident $p\bar{p}$ beam splits into $b\bar{b}$ pair, which is colinear with the beam direction. A hard collision occurs between one of the b quarks and an incident parton. This will "excite" one b quark with high P_T, leaving the other one with very little P_T or lost in the beam. Such a picture also predicts that the η distribution for this kind of events should be concentrated in the forward/backward region. With the requirement that the electron pseudo-rapidity be less than 1.0 and the muon pseudo-rapidity be less than 0.65, generator level Monte Carlo predicts that about 5% of the $e\mu$ events come from flavor excitation.

Since uncertainties from other sources are much larger than the small contribution from the flavor excitation process, we therefore focus our MC $b\bar{b}$ study on the other processes discussed above. In the following discussions, higher order process implies gluon splitting.

5.2 Heavy Quark Fragmentation

Partons fragmenting into their corresponding hadrons lose part of their momentum in the process. The energy tranfer of heavy quark (c, b or t) fragmentation can be discribed by the formula [35]

$$D_Q^H(z) = \frac{N}{z[1 - \frac{1}{z} - \frac{\epsilon}{1-z}]^2}$$

where $z = (E^H + P_{||}^H)/(E^Q + P^Q)$, $P_{||}^H$ is the momentum component of the hadron H parallel to the quark Q momentum direction, $D_Q^H(z)$ is the probability that the heavy quark Q will fragment with value z, ϵ is a constant proportional to $1/M_Q^2$. The normalization constant N is determined by

$$\sum_H \int D_Q^H(z) = 1$$

where the summation is over all hardons containing heavy quark Q. This formula agrees well with experimental measurements for b and c quarks. The measured ϵ value for a b quark is [37, 38]

$$\epsilon_b = 0.006 \pm 0.001 \pm 0.002$$

where the first uncertainty is statistic and the second is systematic.

The smaller ϵ is, the larger $< z >$ is, *i.e.* the hadron retains more parent quark momentum. The $1/M_Q^2$ dependence of ϵ suggests a harder fragmentation for b quark than for c quark. The ISAJET Monte Carlo uses the value $\epsilon_c = 0.30$, which agrees

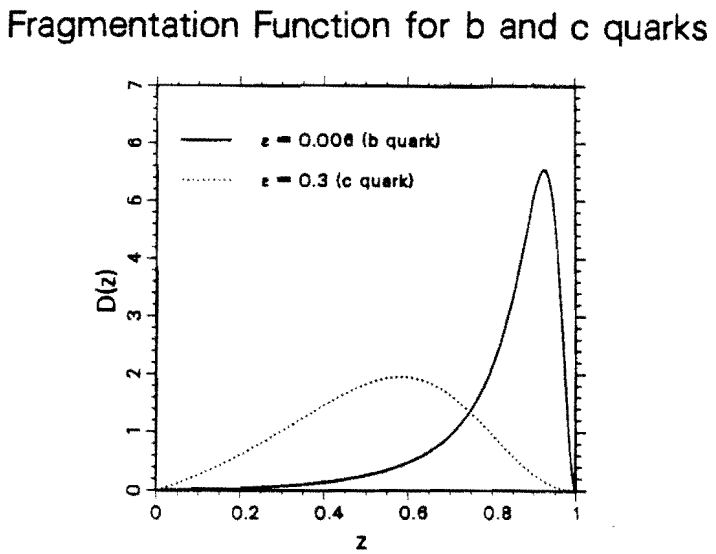

Figure 5.16: Fragmentation function for b and c quarks.

with the e^+e^- experimental results[20]. As an example, the fragmentation function $D_Q^H(z)$ for b and c quarks are shown in figure 5.16. One can see that the bottom quark fragmentation is much harder than that of the charm quark. The hard fragmentation for b quark clearly favor the detection of its decay daughter leptons at high P_T. This is the main reason why the high P_T lepton sample is dominated by b decays.

5.3 Monte Carlo Data Sample

We use ISAJET 6.22 to generate the following processes separately,

$$p\bar{p} \rightarrow b\bar{b} \rightarrow ll$$

$$p\bar{p} \rightarrow c\bar{c} \rightarrow ll$$

$$p\bar{p} \rightarrow g \rightarrow b\bar{b} \rightarrow ll$$

$$p\bar{p} \rightarrow g \rightarrow c\bar{c} \rightarrow ll$$

In this mixing study, one is interested in events with both b quarks decaying to leptons. So only decays that can lead to dilepton final state are completely generated. Some single b to $e\mu$ events are also generated, but not completely. Therefore, we don't expect fraction of single b's (low mass $e\mu$ events) in the Monte Carlo to agree with the data. This does not affect the comparison of events with two b semileptonic decays (after the invariant mass cut).

The generated events are put through the full CDF detector simulation package CDFSIM. Reconstruction was performed using the same CDF production package as for the data.

We generate $b\bar{b}$ and $c\bar{c}$ from lowest order and higher order processes separately. This enables one to study the systematic uncertainties for different event structures. Direct processes give dileptons with large opening angle while gluon splitting contributes more to small opening angle. Also, the correlation between the two leptons in the final state is different. It's generally believed that the lowest order process is easier to model. So, study of the difference between lowest order MC and the data can shed some light on the higher order predictions.

In table 5.1 we summarize the full Monte Carlo data sample. The ratios $f_s = N_s/N_f$ and $f_c = N_c/N_f$, where N_f is the number of $e\mu$ events from two first generation $(b \rightarrow \ell)$ $b\bar{b}$ decays, N_s is the number of $e\mu$ events from one first generation and one

Table 5.1: Summary of full Monte Carlo data sample.

process	lowest order	gluon splitting
1	655 in 3.02 pb^{-1} (OS)	388 in 4.50 pb^{-1} (OS)
2	267 in 4.77 pb^{-1} (LS)	87 in 4.51 pb^{-1} (LS)
3	60 in 5.15 pb^{-1} (OS)	30 in 3.67 pb^{-1} (OS)

Table 5.2: Monte Carlo predictions of no-mixing ratios f_s and f_c.

ratio	lowest order	gluon splitting	overall
f_s	25.8%	22.4%	24.8%
f_c	5.4%	9.5%	6.6%

second generation $(b \to c \to \ell)$ $b\bar{b}$ decays and N_c is the number of $e\mu$ events from $c\bar{c}$ decays $(c \to \ell)$, from the full MC sample are given in table 5.2

The ratios are different between the lowest order and higher order process due to the different event structure *i.e.* P_T spectra and angular correlations. However, as seen from the table, the difference for f_s is actually very small. This is because f_s is the ratio of number of second generation decay B's to that of first generation decay. The difference in these two process is dominated by the decay mechanism. Most effects from the production mechanism cancel. In any case, one would like to

gain more knowledge of the higher order process if possible. In the next subsection, we use the MC data sample to compare with the data. The gluon splitting fraction in the final $e\mu$ sample is checked.

5.3.1 Gluon Splitting Fraction

If the ratio f_s^i is different for lowest order (i=q) and higher order (i=g) processes, and the higher order fraction is f_g, the overall ratio f_s can be written as

$$f_s = \frac{N_s^q + N_s^q}{N_f^q + N_f^q} = \frac{f_s^q + (\frac{f_g}{1-f_g})(\frac{1+f_s^q}{1+f_s^g})f_s^g}{1 + (\frac{f_g}{1-f_g})(\frac{1+f_s^q}{1+f_s^g})}$$

where the super-script q denotes direct production and g is for gluon splitting.

ISAJET predicts a gluon splitting fraction of 28% as as shown in table 5.1. One can measure this quantity in the data using MC input. As discussed above, the direct $b\bar{b}$ is almost back to back while the gluon splitting $b\bar{b}$ are co-linear. The $e\mu$ vector sum P_T is therefore small for the lowest order process and large for gluon splitting. The $e\mu$ vector sum P_T distribution from the final data sample is given in figure 5.17. One can use the MC predictions (figure 5.8 and 5.14) to fit the data spectrum to obtain a measurement of the gluon fraction in the data. The result of 27% agrees with the ISAJET Monte Carlo of about 30%. A comparison of ISAJET prediction and the data is shown in figure 5.17 and 5.18. This gives an example that shows ISAJET associated with CDFSIM is modeling the $b\bar{b}$ to dilepton events relatively well.

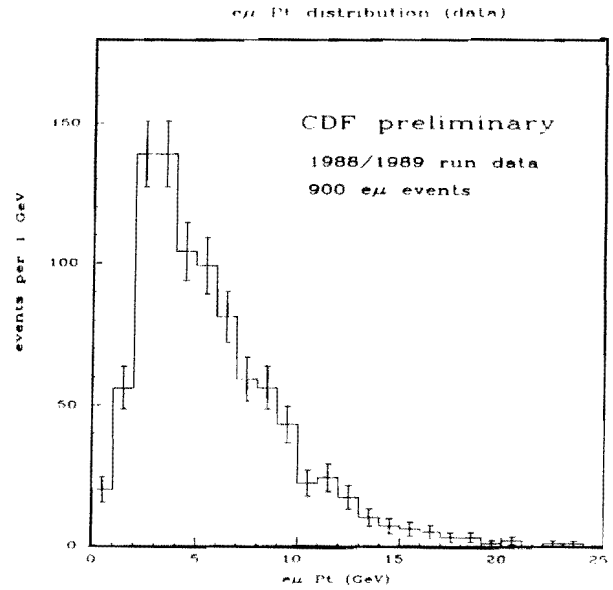

Figure 5.17: $e\mu$ vector sum P_T distribution from final data sample.

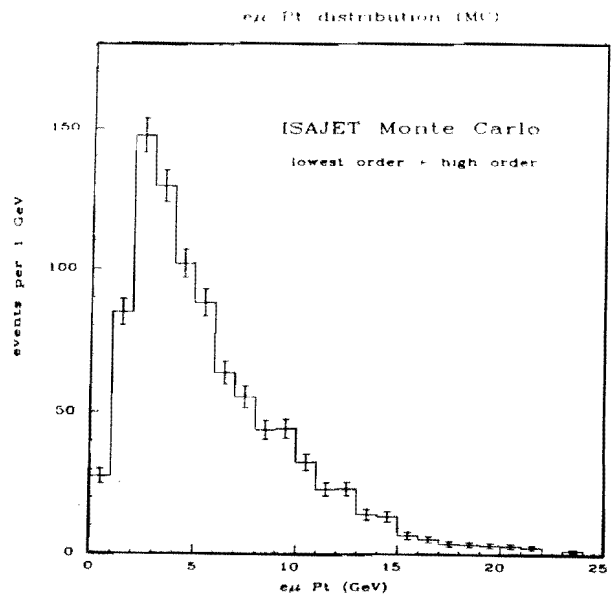

Figure 5.18: $e\mu$ vector sum P_T distribution from Monte Carlo.

Table 5.3: Systematic uncertainties from Monte Carlo predictions.

source	error for f_s	error for f_c
statistics	8%	14%
branching ratio	15%	20%
fragmentation	10%	-
b P_T and $e\mu$ correlation	10%	-
$Z \rightarrow \tau^+\tau^-$	$\leq 2\%$	-
third leptons	$\leq 2\%$	-
other processes	3%	-
$c\bar{c}$ fraction	-	100%
overall	22%	100%

Since the higher order contribution is relative small, the systematic error due to the modeling of the higher order processes will be small. As the Monte Carlo ratio f_s does not differ very much from lowest order to higher order process, the analysis is insensitive to the fraction f_g in the events.

5.3.2 Systematic Uncertainties from Monte Carlo

The possible uncertainties for f_s and f_c from the Monte Carlo is listed in table 5.3. The uncertainties due to b and c semileptonic decay branching ratios are calculated

from

$$f_s \equiv \frac{N_s}{N_f} \sim \frac{Br_b Br_c}{Br_b^2} = \frac{Br_c}{Br_b}$$

and

$$f_c \equiv \frac{N_c}{N_f} \sim \frac{Br_c^2}{Br_b^2}$$

where we take the current Particle Data Group [2] numbers for the average b and c semileptonic decay branching ratios ($Br_b = 11.5\%$). There is a 10% uncertainty associated with each of the averaged branching ratios. Given the large b quark mass, the spectator model should apply relatively well. So one does not expect the B semileptic branching ratios to vary very much for different B hadrons.

The uncertainty due to b quark fragmentation is estimated by varying the Peterson parameter ϵ in ISAJET between the measured 1σ,

$$\epsilon_b = 0.006 \pm 0.001 \pm 0.002$$

We see a 5% change at the generator level. To take into account any possible additional uncertainties due to detector simulation and limited Monte Carlo statistics, we inflated this number to 10%.

The uncertainties due to the b P_T and $e\mu$ correlation prediction in the Monte Carlo is reflected in the f_s value from direct $b\bar{b}$ production (lowest order) process and gluon splitting (higher order) process. When we vary the higher order fraction from 0 to 100%, the change in f_s is only 10% and we take this as part of the systematic uncertainty. Again, this is a very conservative estimate. We've checked (last subsection) that the ISAJET prediction for gluon splitting fraction agrees with the final $e\mu$ sample. So this error assignment also reflects the uncertainty in the ISAJET modeling of the overall P_T of leptons from B decays. Other uncertainties from MC are small and we therefore do not go into the details. It's clear that the errors on the measured branching ratios dominate the uncertainty of f_s.

Since no experimental measurement is available for the $c\bar{c}$ production cross-section at CDF energy, we have to rely on theoretical predictions. This prediction is uncertain because the c quark is not very well described by perturbative QCD. Therefore, we take the b to c production ratio in ISAJET and assign a 100% error to it. This error apparently dominates over other error sources and leads to a 100% error on f_c.

The final results for the ratios are:

$$f_s = 0.248 \pm 0.055$$

$$f_c = 0.066 \pm 0.066$$

In the next chapter, these ratios along with the determined R will be used to extract the $B^0\overline{B}^0$ mixing parameter χ.

Chapter 6

Determination of the Mixing Parameter

6.1 Effect of Monte Carlo ratios f_s, f_c

In the dilepton tagging $B^0\overline{B}^0$ mixing measurement, the signal is embedded in the charge ratio R. Due to sequential B decays, the charge sign of a lepton does not always tag the b quark flavor correctly. So, even in the case of no mixing $b\bar{b}$ decays, R is not zero. For a small ratio f_s, mixing is effective to increase R. This is because mixing turns more OS events into LS events. If $f_s = 1$, R will have no sensitivity to mixing, as

$$R = \frac{2\chi(1-\chi) + [(1-\chi)^2 + \chi^2]f_s}{[(1-\chi)^2 + \chi^2] + 2\chi(1-\chi)f_s + f_c} = \frac{1}{1+f_c}$$

In order to measure the mixing parameter χ using R, it is important to reduce the like-sign events from sequential decays and also those from $c\bar{c}$ decays. Since both f_s and f_c are sensitive to the decay $c \to lX$, sometimes it is possible to reduce or eliminate them. This requires studies of the differences between leptons from b and c decays. Two sources could contribute to the differences. One is the P_T spectra.

Leptons from b decays have a harder spectrum than those from c decays. A high P_T cut is thus effective in reducing the c and sequential b decays. However, since all P_T spectra are sharply falling, this will also reduce the signal. The effect of the P_T cut is already shown in table 3.2 in Chapter 3. In this analysis, the P_T threshold is 3 GeV for muons and 5 GeV for electrons. From a Monte Carlo data sample with the same threshold, we have $f_s \simeq 25\%$. While lowering the threshold certainly increases the signal rate, the background from both real (such as $c\bar{c}$ and sequential B decays) and fake sources will increase. Other Monte Carlo studies have shown that $f_s \simeq 1$ for both lepton P_T around 1 GeV [44]. This more or less sets a limit on how low one can go in P_T for tagging the b flavor with leptons. In mixing measurements, if statistics is not the dominate error source, a higher P_T threshold is favored to minimize systematic errors.

Another way to reduce c decays is by an isolation requirement. This is mainly due to the mass difference between the b and c quarks. If the parent quark is boosted with a certain P_T, it's very likely the decay daughters will fall in a cone. Sometimes a jet can be identified. Leptons in the jet usually have a certain amount of P_T^{rel} relative to the thrust direction. This quantity is a measurement of the parent quark mass, just like the transverse energy of the electrons from W decays. A difficulty in defining such a quantity is that the jet direction is not well measured. If one uses calorimeter jet clustering, the low energy tower is often below threshold (about 500 MeV). Very

high P_T is required for a good measurement. The b or c jets are usually soft. So one can only use tracks to find the jet cluster. Omitting neutral particles will lead to mis-measurement in this method.

In principle, one can also apply an explicit isolation cut to discriminate $c\bar{c}$ and sequential decays. We take the muons in the $e\mu$ events as an example. In figure 6.1 to 6.3 we show the muon border tower energy deposition as modeled by the Monte Carlo. The muon border towers consist of calorimeter towers surrounding the one that the muon passes. From the figures one can see that muons from B decays are more isolated than that from $c\bar{c}$ decays, but there is not very much discrimination. The difference between direct B decay muons and those from sequential decays is very small. This isolation variable is not effective to reduce f_s.

If one can reduce f_s and f_c to a negligible level, no Monte Carlo would be necessary to extract χ from R, as

$$R = \frac{2\chi(1-\chi)}{(1-\chi)^2 + \chi^2}$$

In this analysis, no special cut is made to further reduce f_s or f_c. Such cuts could introduce more systematic errors. For future CDF runs, this kind of consideration should be taken more seriously.

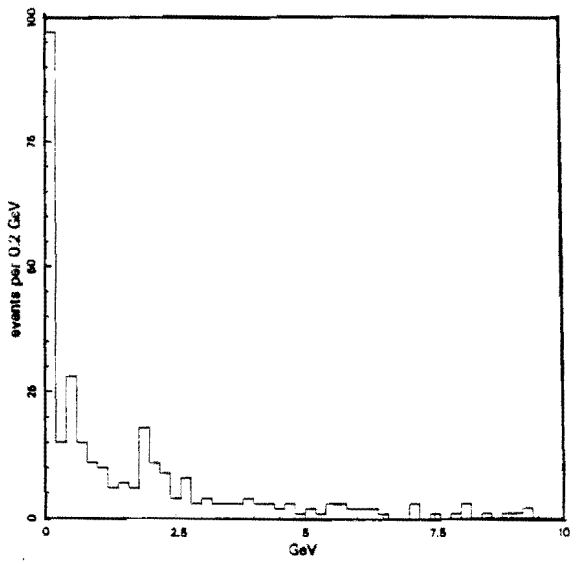

Figure 6.1: Muon border tower energy for LS MC $e\mu$ events from $b\bar{b}$ decays.

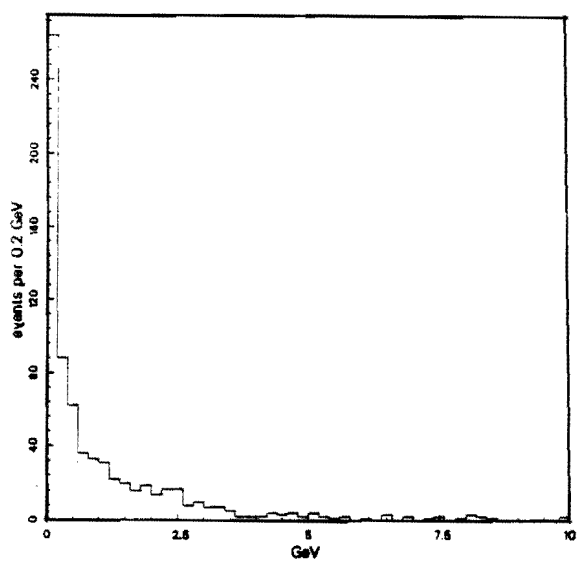

Figure 6.2: Muon border tower energy for OS MC $e\mu$ events from $b\bar{b}$ decays.

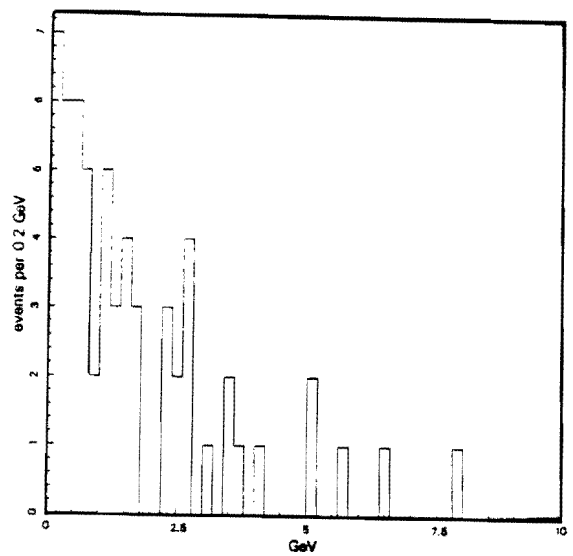

Figure 6.3: Muon border tower energy for MC $e\mu$ events from $c\bar{c}$ decays.

6.2 Effect of Background Fraction f_{BK}

Fake lepton background is another major factor to concern in determining the mixing parameter. Charge correlation in such background is small. So the contribution to LS events is the same as to OS events. In another word, background tends to increase the ratio R, same as mixing.

From the inclusive electron analysis [28], we see that the fake background at CDF is relatively small. By requiring an additional lepton, the signal to background should be improved given the reasonably good lepton identification ability of CDF. This is shown by the following example.

It is worthwhile to note that the charge asymmetry in the single muon background does not effect R given no charge asymmetry in the inclusive electrons. Due to the

difference in K^+ and K^- scattering cross-sections, one expects more μ^+ than μ^- in the kaon punch-through background. Let

$$\frac{N_{\mu^+}}{N_{\mu^-}} = \kappa$$

in the muon background, and

$$\frac{N_{e^+}}{N_{e^-}} = 1$$

then

$$R_{BK} = \frac{N_{e^+\mu^+} + N_{e^-\mu^-}}{N_{e^+\mu^-} + N_{e^-\mu^+}} = \frac{N_{e^+\mu^+}(1+\kappa)}{N_{e^-\mu^+}(1+\kappa)} = 1$$

So even if the single muon events have an arbitrary charge asymmetry, the background $e\mu$ events still are charge symmetric, which is important for the background subtraction.

The background fraction f_{BK} directly effect the determination of the charge ratio R. Therefore, it effects the mixing parameter. A plot of χ versus f_{BK} is shown in figure 6.4. The background fraction cannot be larger than about 65% determined by the observed charge asymmetry.

6.3 the Mixing Parameter

With the data selected in Chapter 3 and background determined in Chapter 4, the $e\mu$ charge ratio is given by

$$R = 261/469 = 0.556 \pm 0.048 \text{ (stat)} \; ^{+0.035}_{-0.042} \text{ (sys)}$$

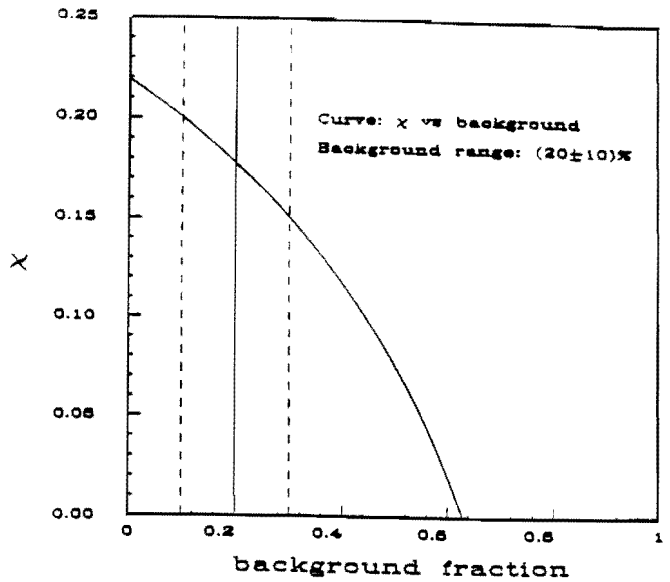

Figure 6.4: Mixing parameter χ as a function of the background fraction f_{BK}.

Using the f_s, f_c ratios determined in Chapter 5, the relation between R and χ is shown in figure 6.5. The no mixing charge ratio is

$$R_0 = \frac{f_s}{1 + f_c} = 0.233 \pm 0.051$$

and the averaged mixing parameter is determined to be

$$\chi = 0.179 \pm 0.027(\text{stat}) \pm 0.022(\text{sys}) \pm 0.032(\text{model})$$

where the statistical and measurement systematic uncertainies are calculated by varying the corresponding uncertainties in R. The systematic uncertainty due to Monte Carlo modeling is calculated by varying the two predicted ratios f_s and f_c within their sigma. It's clear that the overall systematic uncertainty dominates. About half of the Monte Carlo systematic error is due to f_c and the rest is due to f_s. The error on f_c can be reduced easily if the $c\bar{c}$ production cross-section is measured relative to

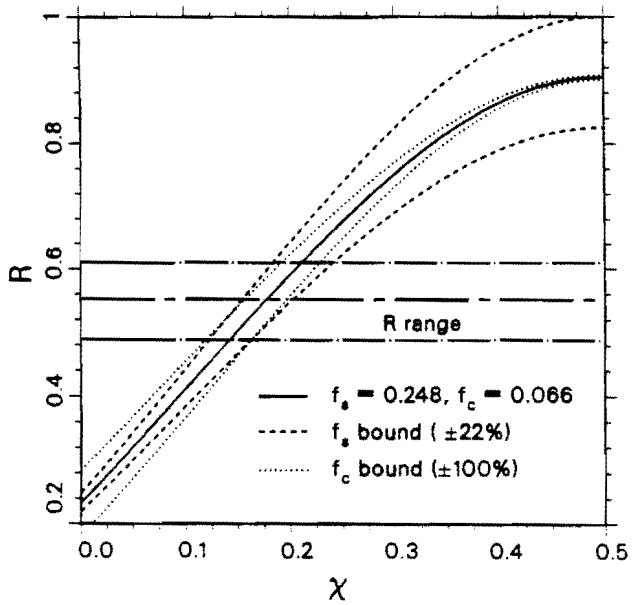

Figure 6.5: Charge ratio R versus mixing parameter χ.

the $b\bar{b}$ at CDF. The error here corresponds to 100% uncertainty in f_c. Monte Carlo predictions with the determined mixing probability are in good agreement with the data. As an example, in figure 6.6, we show the muon P_T distributions for $e\mu$ events from both data and MC sample. To further check the result, we developed a fitting method to determine χ, which is described in the next Chapter.

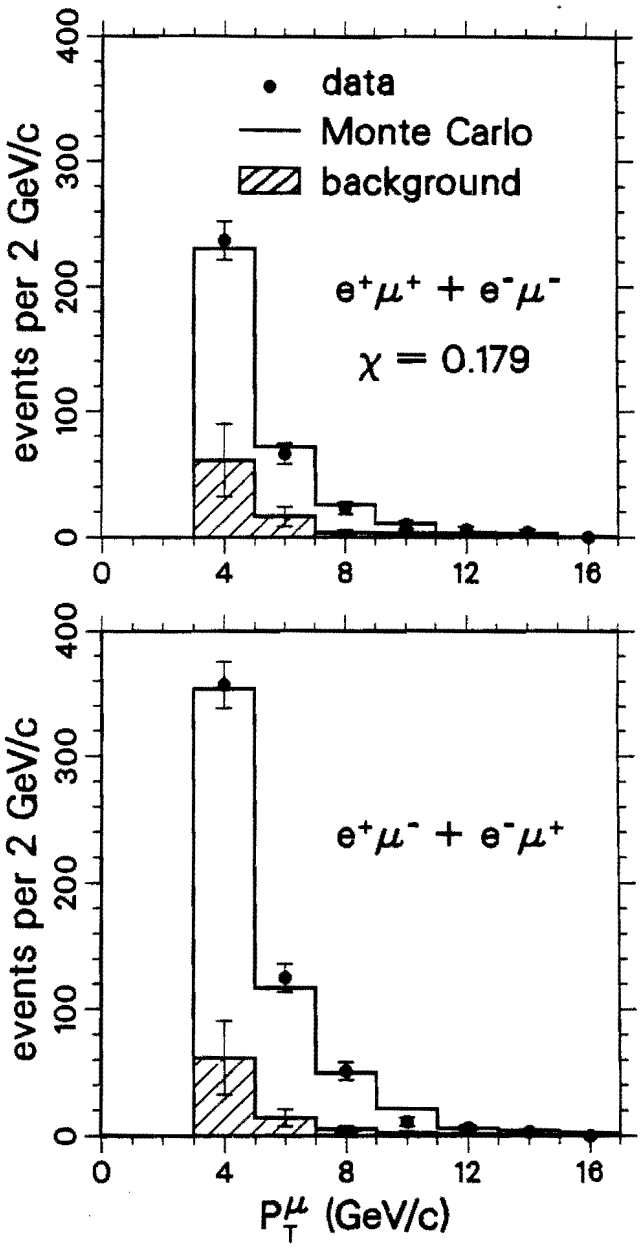

Figure 6.6: Muon P_T spectra for the data, Monte Carlo with the observed mixing and background in like-sign and opposite-sign $e\mu$ events. The uncertainties for the data are statistical only, while those for the background are the determined 47%. Both the data and the Monte Carlo include the background.

Chapter 7

Fitting Method — a Consistency Check

In previous chapters we took the charge ratio R (like-sign events to opposite-sign events) as the directly measured quantity. Then we used the Monte Carlo predictions of the P_T integrated ratios f_s (sequential $b\bar{b}$ decays to direct $b\bar{b}$ decays) and f_c ($c\bar{c}$ decays to direct $b\bar{b}$ decays) to calculate the mixing parameter χ. The Monte Carlo predicted ratio f_s is sensitive to the $b \to l^{\pm}X$ and $b \to cX \to l^{\pm}X$ branching ratios. Actually, the uncertainties in the branching ratios dominate the systematic error from the Monte Carlo. The charge ratio method is not very sensitive to the lepton P_T spectra predicted because one integrates over the P_T range and then takes the ratio. Possible errors can arise from the Monte Carlo predictions of the lepton-lepton correlation and the parent b P_T shape. These effects can change the P_T cut acceptance for like-sign (LS) and opposite-sign (OS) events and therefore alter the derived answer. In order to check these, we now describe another method of determining χ.

The fact that we have a large $e\mu$ data sample (of order 1000 events) provides more

information about the mixing signal than just the excess of like-sign events (large R). This information is contained in the P_T distributions of the LS and OS leptons. Here we use the muon P_T distribution in the final $e\mu$ sample. The electron E_T^e would be more sensitive to effects due to the trigger. The two dimensional E_T^e versus P_T^μ distribution with small bin contents would have a less distinctive shape.

7.1 muon P_T distribution in the final $e\mu$ sample

The muon P_T distributions in LS and OS $e\mu$ events after the invariant mass cut can be described by the following formula:

$$\mathcal{F}_{LS}(P_T^\mu) = N_D p D(P_T^\mu) + N_S(1-p)S(P_T^\mu) + \frac{N_B}{2}B(P_T^\mu) \tag{7.1}$$

$$\mathcal{F}_{OS}(P_T^\mu) = N_D(1-p)D(P_T^\mu) + N_S p S(P_T^\mu) + \frac{N_B}{2}B(P_T^\mu) + N_C C(P_T^\mu) \tag{7.2}$$

where N_D, N_S, N_B, and N_C are the numbers of direct $b\bar{b}$ decays, sequential $b\bar{b}$ decays, background events and $c\bar{c}$ decays, respectively, $p \equiv 2\chi(1-\chi)$ is the probability that one of the b ($\bar{b}$) will change its sign (due to mixing), $D(P_T^\mu)$, $S(P_T^\mu)$, $B(P_T^\mu)$ and $C(P_T^\mu)$ are the normalized distribution functions for different decay processes.

If one integrates over all P_T for the above distributions, (the functions D, S, B and C all normalized to 1.) the numbers N_D and N_S can be written in terms of the measured number of LS and OS events (N_{LS} and N_{OS}) before background subtraction. The results are

$$N_D = [(N_{OS} - \frac{N_B}{2} - N_C)(1-p) - (N_{LS} - \frac{N_B}{2})p]/(1-2p)$$

$$N_S = [(N_{OS} - \frac{N_B}{2} - N_C)p - (N_{LS} - \frac{N_B}{2})(1-p)]/(2p-1)$$

The raw P_T spectra for equation 7.1 and 7.2 are shown in figure 7.1 and 7.2 the $e\mu$ sample. (All distributions in this chapter except otherwise notified have been normalized to 1 for comparisons.) In order to do a fit directly, one would have to know the background distribution $B(P_T^\mu)$ in addition to the Monte Carlo predicted distribution functions (D, S and C). The background distribution is not known. However, the fact that the background contributes equally to LS and OS events enables us to do a background-shape independent fit. (The ratio $LS : OS$ is 1 independent of P_T for the background events. This is because there is no charge correlation in the fake background. It has been checked using electron-track combinations in the inclusive electron sample, see figure 7.4.) Subtracting equation 7.1 from equation 7.2, one obtains

$$\begin{aligned} F(P_T^\mu) &\equiv \mathcal{F}_{OS}(P_T^\mu) - \mathcal{F}_{LS}(P_T^\mu) \\ &= N_D(1-2p)D(P_T^\mu) - N_S(1-2p)S(P_T^\mu) + N_C C(P_T^\mu) \\ &= [(N_{OS} - N_C) - \alpha(\chi, N_B)]D(P_T^\mu) - [N_{LS} - \alpha(\chi, N_B)]S(P_T^\mu) + N_C C(P_T^\mu) \end{aligned} \quad (7.3)$$

where

$$\alpha(\chi, N_B) \equiv (N_{LS} + N_{OS} - N_B - N_C)2\chi(1-\chi) + \frac{N_B}{2}$$

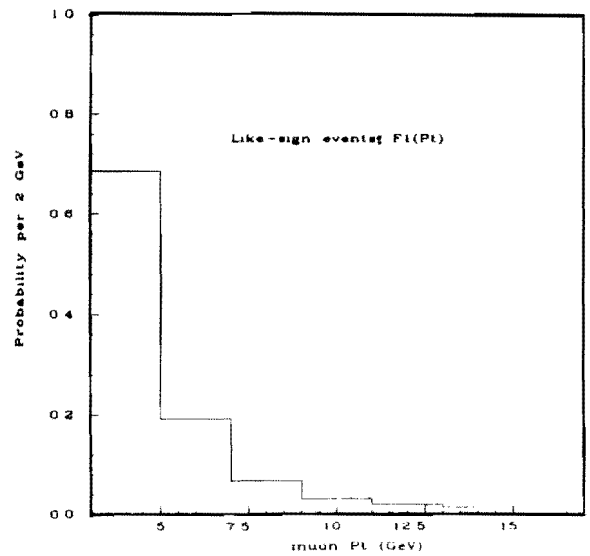

Figure 7.1: Muon P_T spectrum in LS $e\mu$ data.

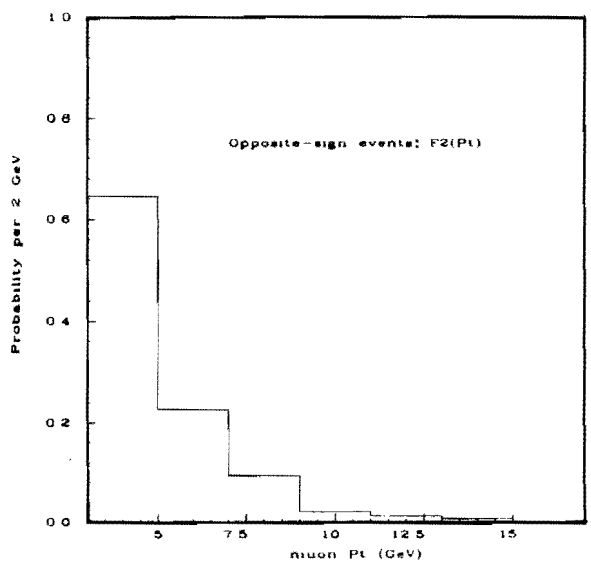

Figure 7.2: Muon P_T spectrum in OS $e\mu$ data.

This distribution does not contain background. The background fraction ($N_B = f_{BK}\,(N_{LS} + N_{OS})$) enters from the normalization. In figure 7.3, we show this background free muon P_T spectrum with the statistical error bars. The distribution itself provides a clear signal for $b\bar{b}$ decays in the $e\mu$ data sample. If the events were dominated by background, the distribution would be flat around zero as in figure 7.4. The background spectrum is obtained using e-track sample from 7 GeV inclusive electron trigger.

In figure 7.5-7.7, we give the predicted muon P_T distribution from a ISAJET $b\bar{b} \rightarrow e\mu$ Monte Carlo sample with 4.5 pb^{-1}. These are the D, S and C functions.

7.2 Fitting

In doing a fit to the background-free distribution (figure 7.3) using equation 7.3, we use the binned likelihood method [21]. The likelihood function is defined as

$$L = \prod_i \frac{1}{N_i!} F_i(P_T^\mu)^{N_i} e^{-F_i(P_T^\mu)} \times \frac{1}{\sqrt{2\pi}\sigma_{f_{BK}}} e^{-(f_{BK}-f_{BK0})^2/2(\sigma_{f_{BK}})^2} \tag{7.4}$$

where N_i is the number of events in each P_T bin in figure 7.3. The Gaussian function allows the background fraction f_{BK} to vary around the central value with the determined uncertainty. The $c\bar{c}$ fraction $N_C/(N_{LS} + N_{OS})$ cannot be determined in the fit because of the similarity of its muon P_T distribution to that of the sequential muons. We vary the $c\bar{c}$ fraction by 100% to study the uncertainty due to this. The fitting is done by maximizing the log-likelihood function, using the CERN library MINUIT

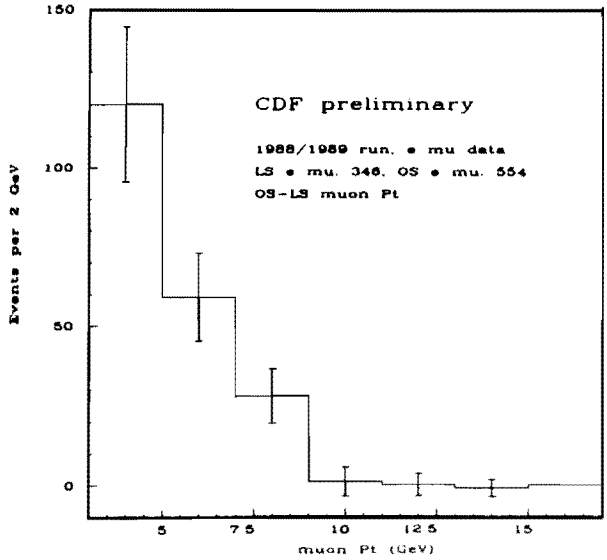

Figure 7.3: Background free muon (OS-LS) P_T distribution in $e\mu$ data.

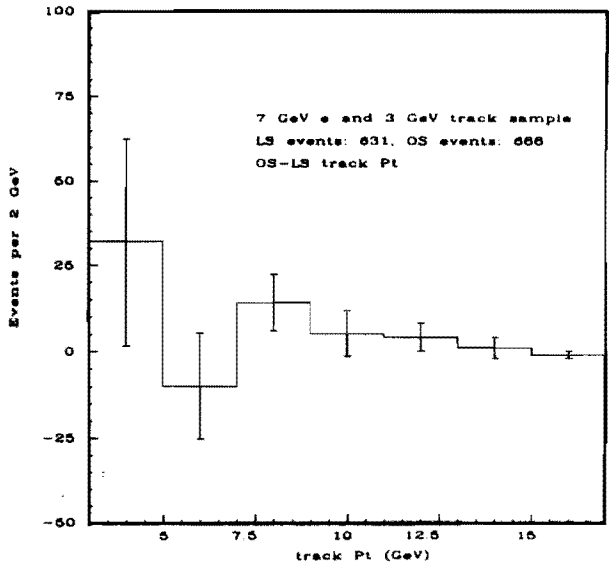

Figure 7.4: Background track (OS-LS) P_T distribution.

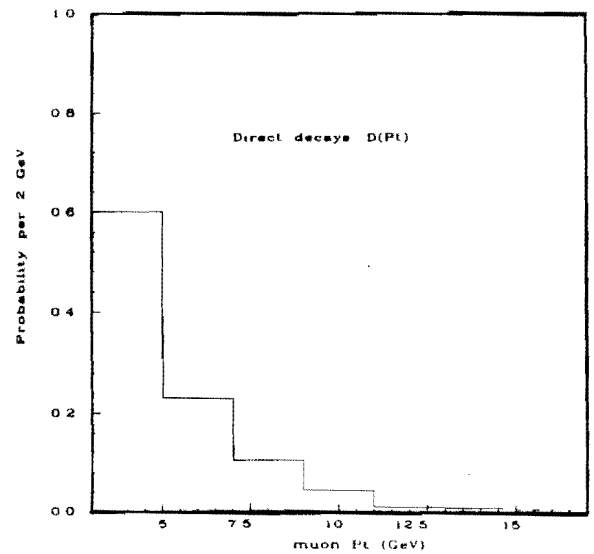

Figure 7.5: Muon P_T spectrum from direct $b\bar{b}\rightarrow e\mu$ decays.

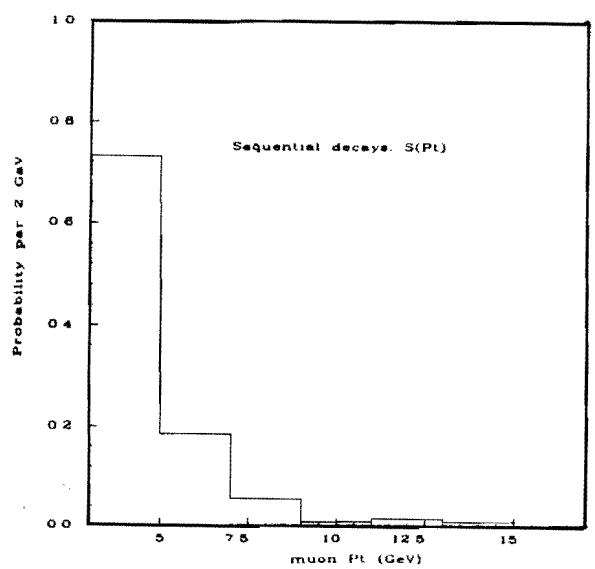

Figure 7.6: Muon P_T spectrum from sequential $b\bar{b}\rightarrow e\mu$ decays.

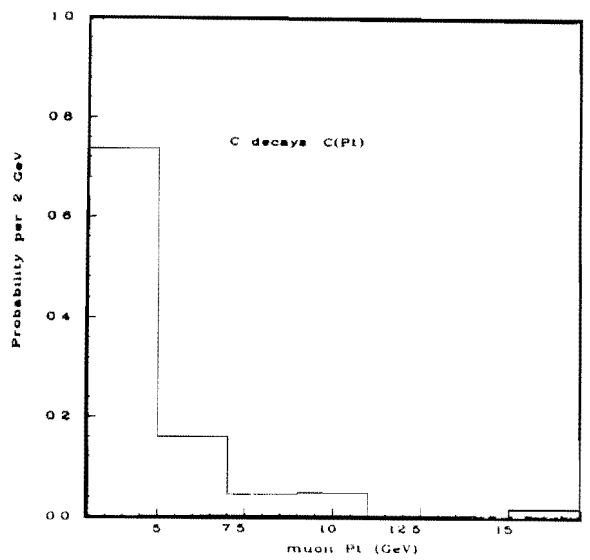

Figure 7.7: Muon P_T spectrum from $c\bar{c} \rightarrow e\mu$ decays.

program package [40].

7.3 Results

The fitting procedure yields the following result

$$\chi = 0.184 \pm 0.065(\text{stat+sys}) \ \pm 0.049(f_c).$$

The systematic uncertainty from background determination and the P_T distributions are in the fitting function while that from the $c\bar{c}$ fraction is determined by varying it within $\pm 100\%$. This χ value can be compared with that from the previous charge ratio method, where

$$\chi = 0.179 \pm 0.040(\text{stat+ sys}). \ \pm 0.025(f_c)$$

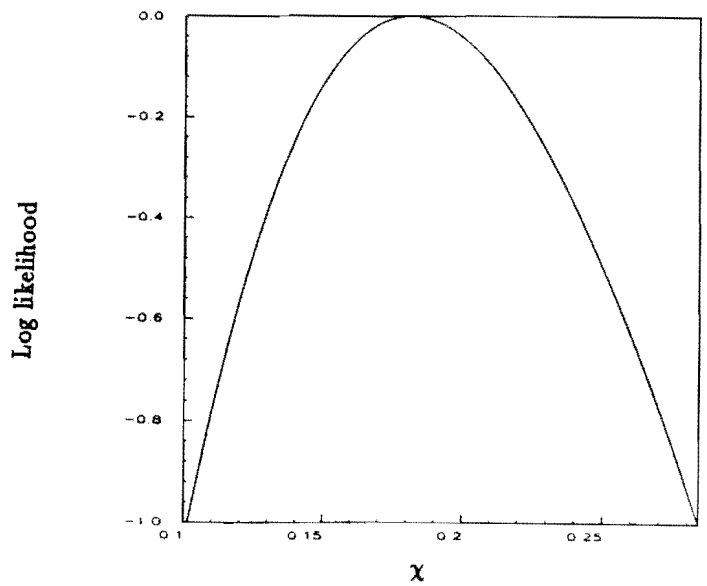

Figure 7.8: Log likelihood function from fitting.

The uncertainty from the fitting method is larger mainly due to the lack of statistics in the background-free P_T distribution.

The log-likelihood function is given in figure 7.8 with the central value of the $c\bar{c}$ fraction of 5.2%. In figure 7.9, we show the mixing parameter χ versus the background fraction f_{BK} for the two different methods. The good agreement gives us more confidence in the Monte Carlo in the charge ratio method for determining χ.

More statistics power can be gained by fitting to both LS and OS event P_T spectra simultaneously. However, such a fit is directly sensitive to f_s itself, so it does not provide an independent check. If the P_T shape in the Monte Carlo is modeled with a high confidence, this kind of fitting method can be used to extract χ without involving the ratio R. In a such method, one also needs to know the P_T spectrum

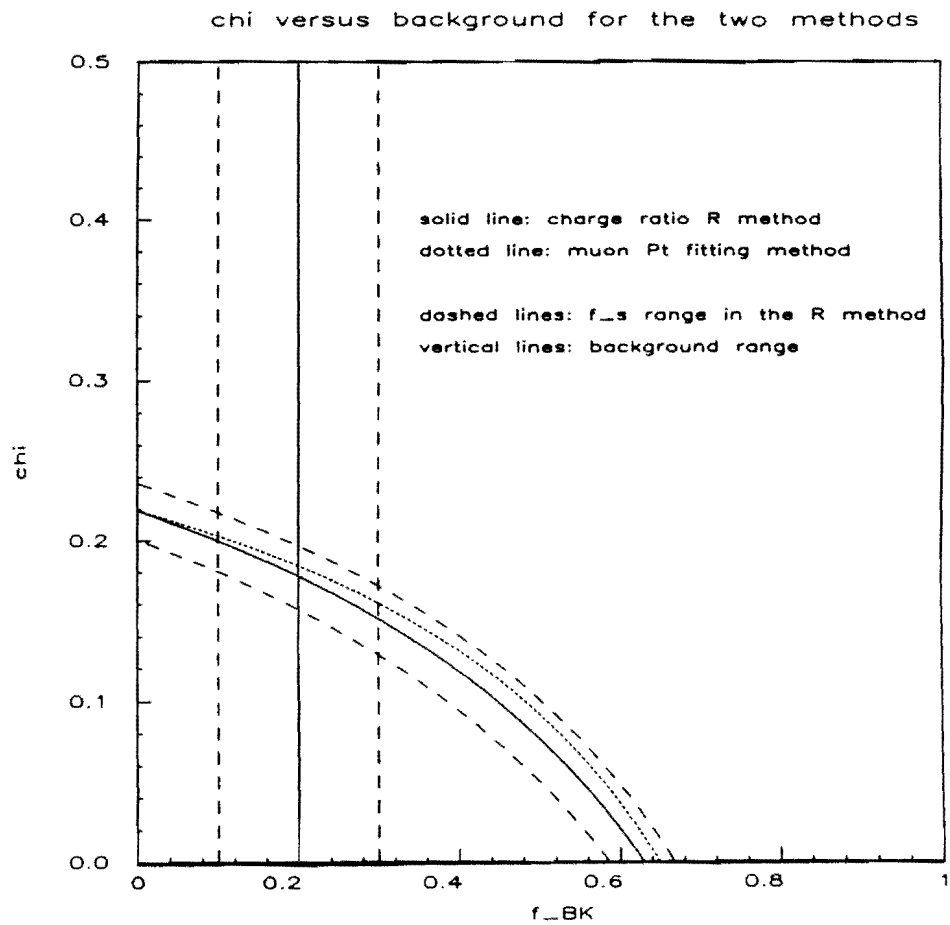

Figure 7.9: χ versus background fraction f_{BK} for R and fitting methods.

of the background events in addition to its fraction. In the next chapter, we discuss some of the other experiments which use this kind of method to measure the mixing parameter.

Chapter 8

Conclusions & Discussions

Analysis of the $e\mu$ events from the 1988-89 CDF run data demonstrates clearly the existence of $B^0\overline{B}^0$ mixing. The averaged mixing parameter is measured to be

$$\chi = 0.179 \pm 0.027(\text{stat}) \pm 0.022(\text{sys}) \pm 0.032(\text{model})$$

CDF currently has the world's largest $e\mu$ sample. This is because of the extremely large $b\bar{b}$ production rate in $p\bar{p}$ collisions at high energies. From this analysis and other B analyses at CDF, it is clear that hadron collider experiments can contribute to B physics study with a large statistics sample. Background from QCD does not dominate over the signal.

While improvements can be made in the data statistics and background determination in the near future, more theoretical and experimental studies on the lepton tagged high P_T $b\bar{b}$ events are desirable. This reflects itself in the large systematic error from the Monte Carlo. More studies of the B decay branching ratios, fragmentation, $b\bar{b}$ correlation and high order processes are necessary to improve this situation.

Theoretical inputs for $b\bar{b}$ production processes and the correlation between the decay leptons will be helpful.

8.1 Other Recent Results

At the time of finishing this analysis, several other experiments also released their preliminary $B^0\overline{B}^0$ mixing results. Two LEP experiments (ALEPH and L3) measured χ using $b\bar{b}$ pairs from Z decays. The CERN $p\bar{p}$ collider experiment UA1 also announced a new χ value from data collected during 1988 and 1989. These experiments use the predicted P_T^{rel} distributions from Monte Carlo. A fit is made to the data in distinguishing the contributions of dileptons from different processes. The mixing parameter χ is one of the fitting parameter.

A summary of current mixing measurements are shown in table 8.1. It's clear that significant progress has been made in this area since the first discovery of $B^0\overline{B}^0$ mixing in 1987. These results are all consistent with the standard model predictions. However, as discussed in the following sections, one can seen that a precise check on the standard model will require more accurate measurements.

8.2 The B_s mixing

The Standard Model predicts a much larger ($\sim$ 5 times) mixing for B_s than for B_d. The mixing probability for B_s is so large that significant oscillations occur in real time

Table 8.1: Summary of current mixing measurements.

experiment	mixing parameter	reference
ARGUS	$\chi_d = 0.170 \pm 0.054$	[6]
CLEO	$\chi_d = 0.154 \pm 0.056$	[7]
ALEPH	$\chi = 0.132 \pm 0.022$	[41]
L3	$\chi = 0.178^{+0.049}_{-0.040}$	[42]
UA1	$\chi = 0.145 \pm 0.035(stat) \pm 0.014(sys)$	[43]
CDF ($e\mu$)	$\chi = 0.179 \pm 0.027(stat) \pm 0.040(sys)$	This work.
CDF (ee)	$\chi = 0.172 \pm 0.060(stat) \pm 0.035(sys)$	[29]

(see Chapter 1). The time integrated signal is therefore reduced due to cancellation. To measure this kind of rapid oscillation, one would need to resolve the mixing signal (usually like-sign to opposite-sign dilepton event ratio R) in time. Such measurements clearly need a fine resolution micro-vertex detector. The most possible scenario for measuring the B_s mixing would be via a silicon vertex detector. A vertex detector with spatial resolution of 10 - 20 μm or so would enable one to measure the time dependence of B decay. By fitting to such a time dependent decay spectrum, one can extract the B_s mixing parameter directly. A large dilepton sample and good momentum resolution will be necessary to perform such a measurement.

While the direct determination of χ_s is out of reach of current experiments, some

knowledge can be gain from the average mixing parameter. Note that

$$\chi = P_d\chi_d + P_s\chi_s$$

where P_d and P_s represents the weight of contributions from B_d and B_s mesons respectively,

$$P_{d(s)} = Prob(b \to \overline{B}^0_{d(s)})\frac{BR(\overline{B}^0_{d(s)} \to l^- X)}{BR(b \to \overline{B} \to l^{\pm} X)}$$

The $B^0_d\overline{B}^0_d$ and $B^0_s\overline{B}^0_s$ mixing parameters were given in chapter 1 as

$$\chi_{d(s)} = \frac{N(B^0_{d(s)} \to \overline{B}^0_{d(s)})}{N(B^0_{d(s)} \to B^0_{d(s)}) + N(B^0_{d(s)} \to \overline{B}^0_{d(s)})}$$

Given P_d, P_s, one can solve for χ_s. The fractions P_d, P_s are not yet measured. A rough estimate can be made from the knowledge of the ratio $u : d : s$. If we assume the same semileptonic decay branching ratios for all B hadrons, the fraction of B hadrons produced is in proportion to $B_u : B_d : B_s : B_{\text{baryons}} = 0.375 : 0.375 : 0.15 : 10$ [41, 42, 43], a diagram of χ_s vs χ_d from this analysis is given in figure 8.1 along with the χ_d value from ARGUS and CLEO. The plot indicates large χ_s, consistent with the standard model predictions. The band from the χ measurement is large because the uncertainty has been amplified by a factor $\sim \frac{1}{P_d}$, which is 2.5 in this case. This also shows how difficult it is to determine χ_s.

An immediate improvement in constraining χ_s can be obtained by combining all of the mixing measurement results. A contour plot which combines all above measurements is given in figure 8.2. In the combination process, we take all published

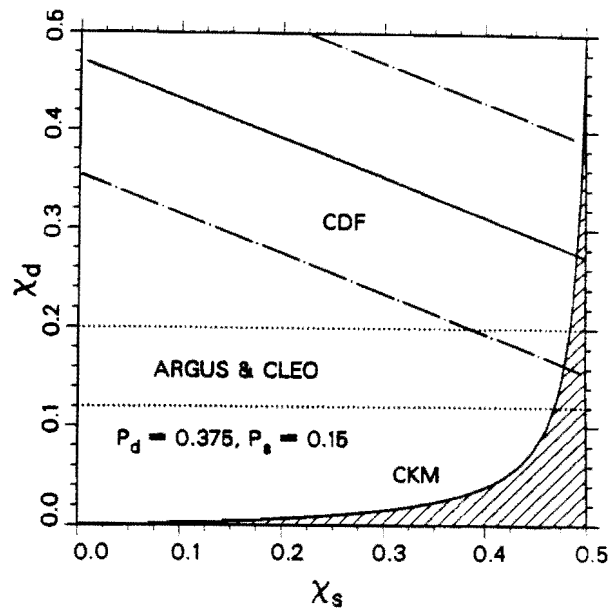

Figure 8.1: CDF $e\mu$ channel: χ_d versus χ_s.

results in table 8.1, treat the uncertainties quoted as gaussian, use the corresponding assumptions for P_d and P_s in the publication. No correlations in the systematic uncertainties is assumed. This is a small effect since most of the results are statistics limited. The contour shows a much better constraint on χ_d versus χ_s plane than any previous measured result. The consistency with minimum standard model prediction is clear.

8.3 Tagging Efficiency, $e\mu$ Rate and CP violation

In studies of the $b\bar{b}$ system such as CP violation, one often needs to tag the flavor of the B or $\overline{B}$. This is most easily done by tagging the flavor of the second B in the event via leptons. We first define a tagging efficiency of the second B as the

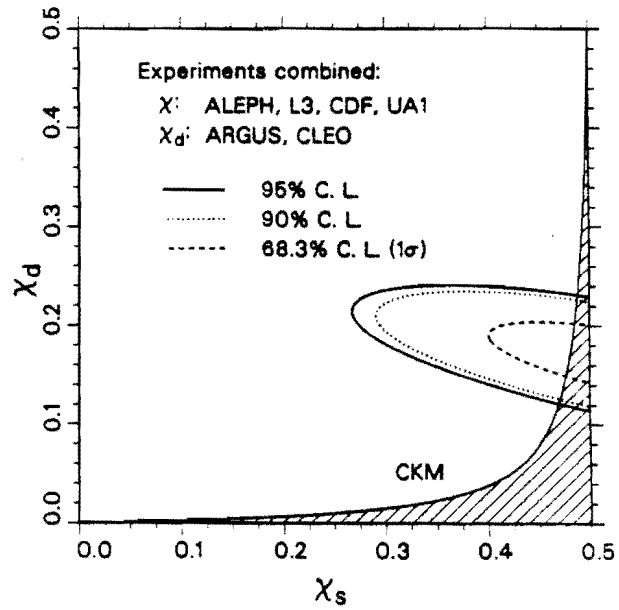

Figure 8.2: All combined: χ_d versus χ_s contour.

probability of finding a second lepton in a lepton tagged sample. For example, in a sample of N_e real electrons from heavy flavor decays, if we find $N_{e\mu}$ events with a real muon, excluding decay-in-flight and single B sequential decays, the tagging efficiency is defined by

$$\epsilon_\mu = \frac{N_{e\mu}}{N_e}$$

This efficiency includes $c\bar{c}$ decay and muons from the other B sequential decays, which will be considered later. We use the 7 GeV trigger inclusive electron sample and require 3 GeV for the muon P_T, the tagging efficiency is found to be

$$\epsilon_\mu = (0.4 \pm 0.1)\%$$

Note, this factor includes the semi-leptonic branching ratio and the detection/cut efficiencies.

This number is clearly very small for various high rate B physics studies. There are several ways to increase the tagging efficiency. The most apparent ways are: extending the detector coverage, lower the P_T thresholds and increase detection efficiencies and use both electron and muon. At CDF, the pseudo-rapidity coverage for electrons and muons is $|\eta| \leq 1.0$ and $|\eta| \leq 0.6$ respectively while CTC provides tracking for $|\eta| \leq 1.2$. So the extension of muon coverage to $|\eta \sim 1.2$ will give a factor of 2 increase. Lowering the P_T threshold gives roughly a factor of 0.5 increase per GeV. So, if one lowers the trigger threshold by 2 GeV, and use both e and μ, one can get about six-fold increase for ϵ_l, i.e. achieving a tagging efficiency of roughly 3%. The upper limit of this efficiency is given by the semi-leptonic branching ratio, which is about 20%. More improvement on the tagging efficiency is under discussion. For example, with particle identification, the kaons can be used as a tag as well [44]. The wrong tagging from $c\bar{c}$ and B sequential decays gives a dilution factor in most cases. For P_T as low as 1 GeV, such dilution factor can be as large as 50%. This has to be taken into account when tagging efficiency is considered for B_s mixing or CP violation measurements.

Another interesting figure for $b\bar{b}$ studies is the dilepton rate, most importantly, the like-sign dilepton rate. From this analysis, we observe 429 like-sign $e\mu$ events,

Table 8.2: Comparison of different B decay channels for CP violation observation.

channel	CP violation (SM)	N (1 fb^{-1})	σ (1 fb^{-1})
$l^{\pm}l^{\pm}$	$10^{-3} - 10^{-4}$	1 M	10^{-3}
$J/\Psi K_S$	$0.30 - 0.02$	900	0.03

of which 86% are from the $e\mu$ trigger with 2.7 pb^{-1}. Using the background fraction of 20%, this gives 109 $e\mu$'s per pb^{-1}. Following the same procedure for the tagging efficiency, this number can be increased by a factor of 12. There is a factor of two by using ee and $\mu\mu$ events. So, one gets about 1,200 like-sign dileptons per inverse picobarn. This includes the low trigger and reconstruction efficiencies during the 88-89 CDF run. Therefore, the actual rate could be much higher.

With all these numbers and the rough limit that CDF currently could have about 10 $B_d \rightarrow J/\Psi K_S$ events, we can compare the inclusive and exclusive B decay channels for future CP violation studies. The results are listed in table 8.2. Mixing affects both cases, so the standard model (SM) prediction would be diluted. The dilution factor is roughly (1-2χ), or about 70%. The rate is calculated for the Tevatron. It requires about 10 fb^{-1} to clarify the SM CP violation. However, with 1 fb^{-1}, the Tevatron can lead us into the interesting region of CP violation.

8.4 Future Prospectives for B physics

In the coming CDF run scheduled to start in early 1992, a silicon vertex detector (SVX) will be commissioned. With the ability to measure the B decay vertices, the background rate can be significantly reduced. Upgrade of the central muon system by adding more muon steel shielding and extending the rapidity coverage will provide better muon identification and more statistics. A much larger event sample is expected with the increase of luminosity to about 100 pb^{-1}. We anticipate the average mixing parameter to be measured more accurately and there is hope of making a direct measurement of χ_s using dilepton triggers. With higher luminosity and improved dilepton triggers, the B_s meson can be reconstructed, which can lead to a measurement of the B_d, B_u, B_s fraction. Other B physics will include: production cross-section in exclusive channels, single lepton and dilepton channels; study of the P_T dependence of the cross-section; measurement of the fractions of different production processes using dilepton events; B lifetime measurements; rare B decays, such as $B \rightarrow \mu^+\mu^-$; discovery of B_s and B baryons; etc.

At LEP or LEP-II, with more Z's being accumulated, more high P_T $b\bar{b}$ events will be collected for B physics and other studies. The e^+e^- colliders operated at lower energies will produce more data for B physics. The fragmentation and various branching ratios will be determined more accurately. Momentum spectra for many decay productions will be measured will high precision. Several fixed-target

[10] F. Abe *et al.,* CDF collab., Nucl. Instr. Meth. **A271**, 387 (1988).

[11] F. Abe *et al.,* CDF collab., Phys. Rev. Lett. **62**, 3020 (1989).

[12] F. Snider *et al.,* Nucl. Instr. Meth. **A268**, 75 (1987).

[13] F. Bedeschi *et al.,* Nucl. Instr. Meth. CTC **A268**, 50 (1988).

[14] L. Balka *et al.,* Nucl. Instr. Meth. CEM **A267**, 272 (1988).

[15] G. Ascoli *et al.,* Nucl. Instr. Meth. CMU **A268**, 33 (1988).

[16] E. Barsotti *et al.,* Nucl. Instr. Meth. DAQ **A269**, 82 (1988).

[17] F. Paige and S.D. Protopopescu, BNL Report No. BNL 38034, 1986 (unpublished). ISAJET version 6.22 was used for this analysis.

See CDF internal note 1379 for a description of the modifications.

[18] J. Freeman, Proceedings of the Workshop on Detector Simulation for the SSC, edited by L. E. Price, ANL-HEP-CP-88-51, Argonne National Laboratory (1987), p. 190. CDFSIM

[19] K. Chadwick, R. Hollebeek, P. K. Sinervo, CPC **45** (1987) 409-415.

[20] UA1 Collab., H.C. Albajar, *et al.,* CERN-EP/87-189, Oct. 1987.

M. Della Negra,

Heavy-flavor Production at the CERN Proton-antiproton Collider

CERN-EP/87-07, Jan. 1987.

[21] CDF Collab., F. Abe *et al*, **PRD** 43 (1991) 664.

[22] CDF Collab., F. Abe *et al*, **PRD** 43 (1991) 2070.

[23] E. Eichten, I. Hinchliffe, K. Lane and C. Quigg
Supercollider Physics,
Rev. Mod. Phys. Vol. 56, No. 4, 1984.

[24] F. Abe *et al.,* CDF collab., Phys. Rev. Lett. **64**, 147 (1990).

[25] D. Smith and H. Jensen, CDF note 707

[26] D. Smith and T. K. Westhusing CDF note 726

[27] CDF Collab., F. Abe *et al*, **PRD** 40 (1989) 3791

[28] J. Proudfoot, F. Ukegawa, A. B. Wicklund, CDF note 1253

[29] L. Kirsch *et al.,* CDF note 1314

[30] W. Y. Chen, *Decays of Upsilon Mesons to the J/ψ Meson*, CLEO Thesis (May 1990).

[31] CLEO Collab., M. Artuso, *et al.,* Phys. Rev. Lett. 62 (1989) 2233.

[32] R. Hughes *et al.,* CDF note 1382.

[33] Y. Cen *et al.,* CDF note 1452.

[34] P. Nason, S. Dawson and R. K. Ellis, Nucl. Phys. B 303 (1988) 607.

[35] C. Peterson, D. Schlatter, I. Schmidt and P. Z. Zerwas,
Phys. Rev. **D27**, 105 (1983).

[36] D. Kuebel *et al.,* ANL-HEP-PR-90-23, March, 1990.

[37] J. Chrin, Z. Phys. C36 (1987) 165.

[38] ALEPH Collab., D. Decamp, *et al.*, Phys. Lett. B244, 551 (1990).

[39] The Particle Data Group, G.P. Yost *et al*, Phys. Lett. **B204,** 74 (1988).

[40] F. E. James and M. Roos, Comput. Phys. Commun. **10,** 343 (1975).

[41] ALEPH Collab., D. Decamp, *et al.*, Phys. Lett. B258, 236 (1991).

[42] L3 Collab., B. Adeva, *et al.*, Phys. Lett. B252, 703 (1990).

[43] UA1 Collab., H.C. Albajar, *et al.*, Phys. Lett. B262, 171 (1991).

[44] Bottom Collider Detector (BCD) proposal to the SSC lab, 1990.

Appendix A

CDF Coordinate System

The CDF coordinate system is defined with the z axis pointing in the anti-proton beam direction, x axis pointing to the Tevatron ring center and y axis perpendicular to the accelerator ring. The $r\phi$ coordinate is defined in the usual way. The polar angle θ is measured with respect to the anti-proton direction.

Appendix B

CDF Jet Algorithm

At CDF, jets are detected as clusters of energy in the calorimeter. A fixed-cone clustering algorithm is used [21]. A continous set of adjacent calorimeter towers with $E_T \geq 1.0$ GeV is defined as a precluster. Clusters are formed from preclusters by considering all the towers in a cone of 0.7 in η-ϕ space centered on the precluster. All towers with $E_T \geq 0.1$ GeV within the cone are included. The E_T-weighted average of the cluster, defined as the centroid is calculated. The cluster is repositioned on the centroid. Around the centroid, towers within the new cone of 0.7 are included in reclustering. This precedure repeats until the towers in a cluster do not change.

If a cluster is completely contained in a larger cluster, the smaller one is dropped. Partially overlapping clusters may be merged together, depending the overlap fraction, defined as the E_T in the overlap region divided by the E_T in the smaller cluster. If the fraction is above 0.75, the two clusters are combined. Otherwise, the towers in the overlap region are divided between the two clusters according to their proximity

to the cluster centroid. After this division, the centroids are recalculated and the towers in the original overlap region are redivided based on their distance from the new centroids. This procedure iterates until a stable configuration is reached.

Appendix C

Calculation of Statistical Uncertainty for the Charge Ratio R

The quantity R in this analysis is defined as the ratio of number of like-sign dilepton events to that of the opposite-sign events after background subtraction. Assume that there are N_{LS} like-sign, N_{OS} opposite-sign events observed in an experiment with the background fraction determined to be f_{BK}. If the background events contribute equally to both like-sign and opposite-sign events, the charge ratio R is given by

$$R = \frac{N_{LS} - f_{BK}(N_{LS} + N_{OS})/2}{N_{OS} - f_{BK}(N_{LS} + N_{OS})/2}.$$

For large N_{LS} and N_{OS}, one can assume gaussian errors for them. So

$$\sigma(N_{LS}) = \sqrt{N_{LS}}$$

and

$$\sigma(N_{OS}) = \sqrt{N_{OS}}.$$

The uncertainty in f_{BK} is treated as part of the systematic error. In calculating the statistical uncertatinty of R, f_{BK} is treated as a constant parameter. From these, the

statistical uncertainty on R can be calculated in the usual way,

$$\sigma(R)^2 = \frac{\partial R}{\partial N_{LS}}^2 \sigma(N_{LS})^2 + \frac{\partial R}{\partial N_{OS}}^2 \sigma(N_{OS})^2.$$